Underlying Event Simulation in the Herwig++ Event Generator

Zur Erlangung des akademischen Grades eines

DOKTORS DER NATURWISSENSCHAFTEN

von der Fakultät für Physik der
Universität Karlsruhe (TH)

genehmigte

DISSERTATION

von

Dipl.-Phys. Manuel Bähr
aus Oberkirch

Tag der mündlichen Prüfung:	19.12.2008
Referent:	Prof. Dr. D. Zeppenfeld
Koreferent:	Prof. Dr. M. Steinhauser

Abstract

We study Quantum Chromodynamics (QCD) at hadron colliders. This is done in the context of general purpose Monte Carlo event generators. The aim of this thesis is to develop and implement a model for the so–called underlying event for the program Herwig++. We discuss multiple parton-parton scattering as source of the underlying event and show that our implementation is able to describe existing data from the Tevatron collider very well. Nevertheless we extend this model by a soft, non-perturbative component. This allows us to use the so–called minimum bias data, where only a minimum amount of requirements on the final-state are imposed, to challenge our model. This extension additionally allows us to couple the underlying event activity to measurements of total and elastic cross sections and therefore offers a powerful constraint to reduce the extrapolation uncertainties.

Zusammenfassung

Wir untersuchen die Quanten-Chromodynamik (QCD) an Hadron-Kollidern. Dies geschieht im Rahmen eines Monte Carlo Ereignis Generators, Herwig++. Das Ziel dieser Arbeit ist die Entwicklung und Implementierung eines Modelles für das sogenannte *underlying event*. Wir diskutieren mehrfache Parton-Parton Wechselwirkungen als Quelle und zeigen, dass unsere Implementierung in der Lage ist existierende Daten des Tevatron Beschleunigers sehr gut zu beschreiben. Gleichwohl erweitern wir dieses Modell um eine nicht-störungstheoretische Komponente. Diese erlaubt uns den Vergleich mit sogenannten *minimum bias* Daten, welche sich durch eine minimale Anzahl an Einschränkungen an die Endzustandsteilchen auszeichnen. Zusätzlich ermöglicht es diese Erweiterung, die Aktivität im underlying event an Messungen des totalen und elastischen Wirkungsquerschnittes zu koppeln, wodurch die Unsicherheiten der Vorhersage reduziert werden.

"The aim of science is not to open the door to infinite wisdom, but to set a limit to infinite error."

— Berthold Brecht, The Life of Galileo.

Contents

Chapter 1

Introduction

We are on the cusp of a new era in particle physics. The imminent start-up of the Large Hadron Collider (LHC) at the European Organization for Nuclear Research (CERN) is very likely to end decades of painful uncertainty in theoretical physics. We will learn if electroweak symmetry-breaking is realised using the Higgs mechanism and thus may find the last piece in the puzzle that we called the *Standard Model* (SM) of particle physics. It will tell us whether Supersymmetry is a property of our universe or remains a mathematical concept. It may even provide us more insight into the space-time structure of our universe, by testing the idea of extra dimensions.

However, the price to pay for answering these fundamental questions is the tremendous complexity of the experiments at LHC. On the one hand we face the purely technical challenges of operating this huge machine and measuring micrometer distances with detectors of 20-45 meters size. On the other hand we have to make full use of and understand the outcome of the high-energy proton-proton collisions at LHC. We, as theorists, can contribute to the latter one by providing accurate predictions for these interactions. Anyhow, the task remains colossal and can only be addressed in close collaboration between theory and experiment.
To illustrate that, let us consider a typical final-state that will be produced at LHC. By the time the particles hit the first detector layer, it will contain $\sim 500 - 1000$ particles of only a handful different particle types. This introduces a huge ambiguity as soon as one tries to infer the underlying parameters of the theory from the

observed final-states. "New" physics will in general not produce hadronic final-states that are completely different from the Standard Model ones. It will rather show up as an excess of certain events over a background of Standard Model origin. This makes it in many cases almost impossible to extract properties of the underlying theory directly from the statistical analysis of these events. One rather relies on a fully exclusive hadronic simulation of these final-states using Monte Carlo Event Generators. They implement the underlying theory to the best of our knowledge. Hence, it is crucial that both the simulation of new physics and the physics of conventional origin are accurately described.

Calculating the rates of specific processes utilises the *parton model* (which is described in the next Chapter). The main assumption there is, that the collision of a hadron pair can be described as collision of a parton pair during the passage of the hadrons through each other. However, plenty of data (from UA1-5 to CDF) suggests that this picture is too simple and that more than one parton pair may interact during a single hadronic collision, which gives rise to multiple partonic interactions (MPI). These additional interactions occur in most cases at much smaller energy scales than the main (hard) interaction. Since they do occur at scales that are still perturbative, they are often referred to as *semi-hard* interactions. MPI are also expected from the theoretical point of view, since the cross section for these semi-hard jets[1] may violate unitarity as long as multiple scatterings are ignored. Apart from the semi-hard correction, one has to consider the break-up of the incoming hadrons during the partonic scattering(s) and the further evolution of the hadron remnants. This happens at typical hadronic scales, *i.e.* in the non-perturbative or soft regime. These two effects are what theoretically is attributed to the so-called *underlying event*. From the experimental point of view however, the underlying event contains all activity in a hadronic collision that is not related to the signal particles from the hard process, e.g. leptons or missing transverse energy. The additional particles may result from the initial- or final-state radiation of coloured particles or from multiple interactions.

The aim of this work is the introduction and implementation of a model to describe the underlying event for the event generator Herwig++. The validation and tuning of this model against existing data is also an integral part of this task, since data

[1] Sometimes referred to as *mini-jets*

is the ultimate judge for our work.

We will start in Chap. 2, by introducing the basics of Quantum Chromodynamics (QCD), scattering theory and the concept of jets, which are needed to understand the underlying event. The next Chapter then reviews the main features of general-purpose event generators and describes the details for the case of Herwig++.

An introduction to MPI is given in Chap. 4, as well as the model and implementation details of MPI. A detailed tune to and comparison with CDF measurements on the underlying event is also presented there, as well as extrapolations to the LHC.

Chapter 5 contains the description and study of so-called *double parton scattering* events, which separate from the above mentioned multiple semi-hard scatterings in the energy scale that is involved there, which is always *hard*. We show the operability of the simulations of these event with the example of like sign di-lepton production. We compare Standard Model processes leading to that signature with double parton scattering events.

Chapter 6 completes the underlying event model in adding the non-perturbative or soft interactions to the model. We study general properties of this model as a function of the centre-of-mass energy and derive constraints on its parameter space that are imposed by existing or future measurements.

The findings of the previous Chapter lead us to the formulation of an improved model, which will be described in detail in Chap. 7. We describe the implementation of this improved model and compare the simulation to existing data. The inclusion of soft scatters will enable us to describe also minimum bias data which is not possible in a model without this soft component. Finally, we tune this model and make predictions for the LHC.

The last Chapter finally gives a summary and conclusion of the work that has been done.

Chapter 2

Basics

"If I could explain it to the average person, I wouldn't have been worth the Nobel Prize."
— Richard Feynman, 1985

The presence of the underlying event can only be understood in terms of hadrons as compound objects and the strong interaction among the constituents, the *partons*. Hence, the understanding of these phenomena requires a sound knowledge of the strong interaction. This chapter therefore serves as an introduction to scattering theory, theorems which hold independent of the precise theory formulation and non-perturbative as well as perturbative attempts to understand the strong force. Finally, the manifestations of partons in experiments, the *jets*, deserve a careful description and explanation.

2.1 Scattering theory

Throughout this work the system of natural units, where $\hbar = 1 = c$, is used. The two-body scattering process $1 + 2 \to 3 + 4$ may serve as an entry to the basic formalism that is at the foundation of scattering theory. The particles $1 \ldots 4$ have four-momenta $p_i = (E_i, \mathbf{p}_i)$ and the masses $m_i \equiv \sqrt{p_i^2}$. This system has the

Lorentz invariants (the *Mandelstam* variables),

$$s = (p_1 + p_2)^2 \,, \qquad t = (p_1 - p_3)^2 \,, \qquad u = (p_1 - p_4)^2 \,, \tag{2.1}$$

that satisfy the relation $s + t + u = \sum_i m_i^2$. Hence, a *scattering amplitude* that describes the transition of the initial-state $|i\rangle = |1{+}2\rangle$ to the final-state $|f\rangle = |3{+}4\rangle$ during a scattering process, will only be a function of two independent Lorentz invariants and may be written as $\mathcal{A}(s,t)$.

2.1.1 The S-matrix

For orthonormal states $|i\rangle$ and $|f\rangle$, not restricted to the two-body scattering case, that satisfy $\langle f|f\rangle = 1 = \langle i|i\rangle$ and $\langle f|f'\rangle = \delta_{ff'}$, the *S-matrix element* $\langle f|S|i\rangle$ is defined [1] such that

$$P_{fi} = |\, \langle f|S|i\rangle \,|^2 \tag{2.2}$$

is the probability of initial-state $|i\rangle$ resulting in the final-state $|f\rangle$. The completeness of the states $|f\rangle$ together with sum of probabilities being one, leads to $SS^\dagger = 1$, *i.e.* the S-matrix is unitary. It is usually expressed as the sum of an interacting (the so-called T-matrix) and a non-interacting part (the identity operator). They are related by

$$\langle f|S|i\rangle = \delta_{fi} + i(2\pi)^4 \delta^4(P_f - P_i)\, \langle f|T|i\rangle \,, \tag{2.3}$$

where $P_f(P_i)$ denotes the four-momentum sum of all final- (initial-) state particles. The total *cross section* for the reaction $12 \to n$ is defined as

$$\sigma_{12\to n} = \frac{1}{4k\sqrt{s}} (2\pi)^4 \delta^4(P_f - P_i)\, |\, \langle f_n|T|i\rangle \,|^2 \,, \tag{2.4}$$

where $k = |\mathbf{k}|$. $\mathbf{k}$ is the momentum of the incoming particles in the centre-of-mass frame (CMF). For the case of elastic two-body scattering and a continuum of states, the differential cross section with respect to t is then given by

$$\frac{\mathrm{d}\sigma_{12\to 34}}{\mathrm{d}t} = \frac{1}{64\pi s\; k^2} \left|\mathcal{A}(s,t)\right|^2 \,, \tag{2.5}$$

where $\langle f|T|i\rangle \equiv \mathcal{A}(s,t)$ has been identified.

The optical theorem

The unitarity of the S-matrix provides an important connection between total cross sections and the forward ($\theta \equiv \theta_{\mathrm{CMF}} = 0$) elastic amplitude, known as the *optical theorem*, which will be very useful in later chapters. Starting with

$$\delta_{ij} = \langle j|i\rangle = \langle j|SS^{\dagger}|i\rangle = \sum_f \langle j|S|f\rangle \langle f|S^{\dagger}|i\rangle \tag{2.6}$$

and using the definition of the T-matrix from Eq. (2.3), one obtains

$$\langle j|T|i\rangle - \langle i|T^{\dagger}|j\rangle = i(2\pi)^4 \sum_f \delta^4(P_f - P_i) \langle j|T^{\dagger}|f\rangle \langle f|T|i\rangle \ . \tag{2.7}$$

For the case $i = j$, which corresponds to elastic scattering with vanishing scattering angle θ *i.e. elastic, forward* scattering, this yields

$$2\mathfrak{Im}\{\langle i|T|i\rangle\} = \sum_f (2\pi)^4 \delta^4(P_f - P_i) \,|\langle f|T|i\rangle|^2 \ . \tag{2.8}$$

The right-hand-side is proportional to $\sigma_{12\to n}$ from Eq. (2.4) summed over all n. $\theta = 0$ corresponds to vanishing t and therefore the *optical theorem*,

$$\sigma_{12}^{\mathrm{tot}} = \frac{1}{2k\sqrt{s}} \,\mathfrak{Im}\{\mathcal{A}(s,t=0)\} \ , \tag{2.9}$$

is obtained. $\mathcal{A}(s,t)$ is the *elastic* amplitude. In the high-energy limit, where the masses of all particles are negligible, k is given by $\sqrt{s}/2$ and thus

$$\sigma_{\mathrm{tot}} = \frac{1}{s}\mathfrak{Im}\{\mathcal{A}(s,t=0)\} \ , \tag{2.10}$$

where σ_{tot} is the cross section for the scattering of two particles resulting in *any* final-state.

Elastic Scattering

Elastic scattering is connected to the total cross section as discussed in the previous section. The structure away from the limit $t \to 0$ exhibits also interesting features. The differential cross section with respect to t from Eq. (2.5) has been empirically parameterised in the form

$$\frac{\mathrm{d}\sigma_{\mathrm{el}}}{\mathrm{d}t} = \left.\frac{\mathrm{d}\sigma_{\mathrm{el}}}{\mathrm{d}t}\right|_{t=0} \cdot e^{b_{\mathrm{el}}t} \,, \tag{2.11}$$

with b_{el} the *elastic slope* parameter. Using this functional form in Eq. (2.5) and inserting Eq. (2.10) leads to

$$\sigma_{\mathrm{el}} = \frac{\sigma_{\mathrm{tot}}^2}{16\pi b_{\mathrm{el}}}(1+\rho^2) \,, \tag{2.12}$$

with $\rho = \mathfrak{Re}\{\mathcal{A}\}/\mathfrak{Im}\{\mathcal{A}\}$. Measurements show that $\rho \lesssim 0.2$ and therefore the real part of the elastic amplitude is often neglected.

2.1.2 Geometrical correspondence

At high energies, scattering processes can be described by means of geometrical optics since the typical wavelength is smaller than their transverse size [2]. This picture is based on the *impact-parameter* space, usually represented by vectors $\mathbf{b}$, the two-dimensional physical space perpendicular to the beam direction[1]. The spin of the scattering particles is neglected in the following, which is a good approximation in the case of small scattering angles. Working in the CMF, t is given by

$$t = -q^2 = -4k^2 \sin^2\left(\frac{\theta}{2}\right) \,, \tag{2.13}$$

[1] defined by $\mathbf{k}$ in our case.

where q^2 is the magnitude of the momentum transfer. The scattering amplitude can now be expanded in Legendre polynomials

$$\mathcal{A}(s,t) = 16\pi \sum_{\ell=0}^{\infty}(2\ell+1)a_\ell(s)P_\ell(\cos\theta)\,, \tag{2.14}$$

since angular momentum is conserved during the scattering process. By comparing Eqs. (2.5) and (2.10) a requirement for a_ℓ can be deduced. It states that $\mathfrak{Im}\{a_\ell\} = (\mathfrak{Im}\{a_\ell\})^2 + (\mathfrak{Re}\{a_\ell\})^2$, which defines the so-called *Argand circle*. For inelastic processes the amplitude lies inside this circle. Such an amplitude can always be represented as

$$a_\ell = \frac{e^{2i\delta_\ell} - 1}{2i}\,, \tag{2.15}$$

where δ_ℓ acquires an imaginary component if there is inelasticity. The optical theorem additionally implies, that the ℓth partial wave, σ^ℓ_{tot}, is bound as $\sigma^\ell_{\text{tot}}(s) \leq (2\ell+1)\frac{4\pi}{k^2}$. This bound is decreasing in energy and is in contrast to the measured rise of total hadronic cross sections for a fixed number of partial waves. That means that an increasing number of partial waves must contribute to the high-energy amplitude. It is therefore sensible to convert the discrete sum in Eq. (2.14) into an integral,

$$\mathcal{A}(s,t) = 16\pi \int_0^\infty \mathrm{d}\ell(2\ell+1)a(s,\ell)P_\ell(\cos\theta)\,, \tag{2.16}$$

where $a(s,\ell)$ is the analytic continuation of $a_\ell(s)$. The additional relations,

$$\begin{aligned} P_\ell(\cos\theta) &\overset{\ell\to\infty}{\to} J_0\left[(2\ell+1)\sin\left(\frac{\theta}{2}\right)\right]\,, \\ J_0(z) &= \frac{1}{2\pi}\int_0^{2\pi}\mathrm{d}\phi\, e^{iz\cos\phi}\,, \\ \mathbf{q}\cdot\mathbf{b} &= \mathbf{q}_\perp\cdot\mathbf{b} = q_\perp b\,\cos\phi\,, \end{aligned}$$

allow the conversion of the integral in Eq.(2.16) into

$$\mathcal{A}(s,t) = 4s\int \mathrm{d}^2\mathbf{b}\;\; a(s,\mathbf{b})\, e^{-i\mathbf{q}\cdot\mathbf{b}}\,, \tag{2.17}$$

where $a(\mathbf{b}, s) = a_\ell(s)|_{l=kb}$ can be interpreted as source-density of scattered waves producing interference patterns. This expression for the elastic amplitude can now be inserted into Eqs.(2.10) and (2.5), and yields the relations

$$\sigma_{\text{tot}}(s) = 4 \int \mathrm{d}^2\mathbf{b} \;\; \mathfrak{Im}\left\{a(\mathbf{b}, s)\right\} , \qquad \sigma_{\text{el}}(s) = 4 \int \mathrm{d}^2\mathbf{b} \;\; \left|a(\mathbf{b}, s)\right|^2 . \tag{2.18}$$

The elastic slope b_{el} is given by [2]

$$b_{\text{el}} = \frac{\int \mathrm{d}^2\mathbf{b} \;\; b^2 a(\mathbf{b}, s)}{2 \int \mathrm{d}^2\mathbf{b} \;\; a(\mathbf{b}, s)} . \tag{2.19}$$

2.2 Regge theory

Before a field theoretical approach (QCD) for the understanding of the strong interactions was within reach, the so-called *Regge theory* [1, 3] very successfully described the scattering of strongly interacting particles. It is based on very general properties of the S-matrix that were partly discussed in Sect. 2.1.1, *i.e.* lorentz invariance, unitarity and analyticity in the Mandelstam variables (regarded as complex variables). Furthermore it exploits the formalism that Regge [4] developed for non-relativistic potential scattering. This formalism involved converting the orbital angular momentum ℓ into a complex variable. He showed that the singularities of the t-channel partial wave amplitude $a_\ell(t)$ are poles in the complex ℓ plane, the so-called *Regge poles* or *Reggeons*, which are t-dependent. Crossing symmetry of the S-matrix as consequence of analyticity allows for the application of Eq. (2.14) to resonance production in the t-channel. With $\cos\theta = 1 + \frac{2s}{t}$ in the high-energy limit, the elastic amplitude yields

$$\mathcal{A}(s, t) = 16\pi \sum_{\ell=0}^{\infty} (2\ell + 1) a_\ell(t) P_\ell \left(1 + \frac{2s}{t}\right) . \tag{2.20}$$

This sum can be converted to an contour-integral in the complex angular momentum plane (the Sommerfeld-Watson transform). In the *Regge region*, that is $s \gg |t|$, the amplitude vanishes for $|\ell| \to \infty$ leaving only the sum over the residues of the Regge poles at $\ell_k = \alpha_k(t)$. In this limit, $P_\ell(1 + 2s/t)$ can be approximated by $(s/(2t))^\ell$ and therefore only the leading Regge pole with the largest value has

to be considered, leading to

$$\mathcal{A}(s,t) \quad \overset{s\to\infty}{\to} \quad \beta(t)\,\frac{\eta + \; e^{-i\pi\alpha(t)}}{2}\; s^{\alpha(t)}\,, \tag{2.21}$$

where $\alpha(t)$ is the position of the leading Regge pole and η its signature, defined as $\eta_{\text{baryons}} = (-1)^{J-1/2}$ and $\eta_{\text{mesons}} = (-1)^{J}$.

2.2.1 Regge trajectories

Amplitudes for t-channel processes with positive t are expected to have poles corresponding to the exchange of physical particles of spin J_k and mass m_k. For the Regge poles must therefore hold that $\alpha_k(m_k^2) = J_k$. It has been observed experimentally in Ref. [5] that these resonances lie on a straight line, once the spins are plotted against the square mass, *i.e.*

$$\alpha(t) = \alpha(0) + \alpha' t\,. \tag{2.22}$$

Hence, the amplitude of such a Reggeon exchange is estimated by summing up all resonance exchange amplitudes. The Regge poles therefore have definite quantum numbers like isospin, parity or strangeness. The mesons ρ and ω belong to such a trajectory as depicted in Fig. 2.1. The extracted parameters from the data are

$$\alpha_\rho(t) = 0.55 + 0.86\ \text{GeV}^{-2}\ t\,. \tag{2.23}$$

From the asymptotic s-dependence of the amplitude in Eq. (2.21), the s-dependence of differential elastic cross sections can be deduced with Eq. (2.5),

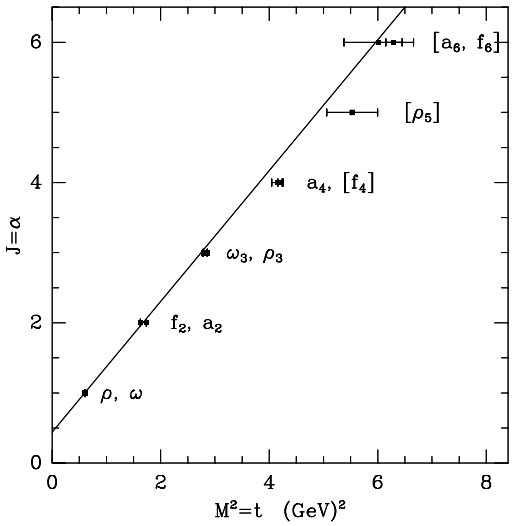

Figure 2.1: The Chew-Frautschi plot for the ρ-trajectory. Taken from Ref. [6].

to be

$$\frac{\mathrm{d}\sigma}{\mathrm{d}t} \propto s^{2(\alpha(0)-1+\alpha' t)} \,. \tag{2.24}$$

The s-dependence of the elastic slope b_{el} can be extracted from that,

$$b_{\mathrm{el}}(s) = 2\alpha' \ \ln\left(\frac{s}{s_0}\right) \,, \tag{2.25}$$

using $b_{\mathrm{el}} = \frac{\mathrm{d}}{\mathrm{d}t} \ln \frac{\mathrm{d}\sigma}{\mathrm{d}t}$. All constant factors have been absorbed into s_0, which has to be determined experimentally.

2.2.2 Total cross sections and the Pomeron

In the same way as for the elastic cross section, one can extract the asymptotic s-dependence of the total cross section from a given Regge trajectory. In using the optical theorem from Eq. (2.10), one obtains

$$\sigma_{\mathrm{tot}} \propto s^{\alpha(0)-1} \,. \tag{2.26}$$

For the ρ-trajectory from Eq. (2.23) this means that the total cross section falls as s increases. Pomeranchuk proved from general assumptions, that in any scattering process in which there is charge exchange, the cross section vanishes asymptotically. This is known as the *Pomeranchuk theorem*. It has been noticed, that a scattering cross section that does not fall with increasing s must be dominated by the exchange of vacuum quantum numbers.

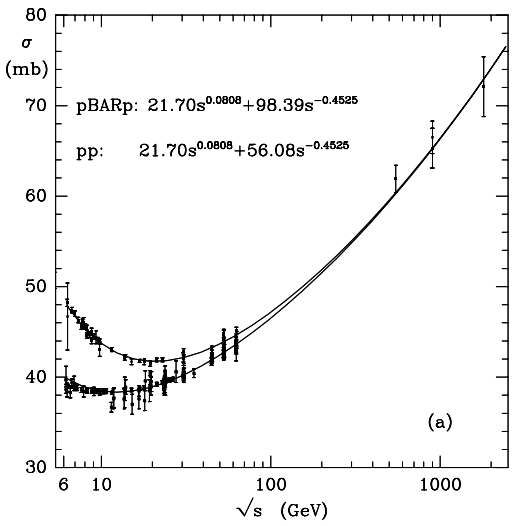

Figure 2.2: Data for the total pp and $p\bar{p}$ cross section over a wide range of energies. Included is the Regge fit from Ref. [6].

Experimentally, a slow rise of the total cross section with increasing s is observed. If this rise is attributed to the exchange of a single Regge pole, it must satisfy

$\alpha(0) > 1$ and carrying vacuum quantum numbers. This trajectory is usually called the *Pomeron* after its inventor Pomeranchuk.

Donnachie & Landshoff [6] have performed a fit of all available total cross section data with a Regge type parameterisation given by

$$\sigma_{\text{tot}} = X s^{\epsilon} + Y s^{-\eta}\,, \tag{2.27}$$

where the first term corresponds to a Pomeron Regge pole, whereas the second term is due to the exchange of the ρ-trajectory from Eq. (2.23). The Pomeron contribution must be identical in pp and $p\bar{p}$ scattering, as it carries vacuum quantum numbers. For the ρ-trajectory this obviously does not hold. ϵ is extracted to be 0.08 and $\eta = 0.45$. The complete parameterisation of the Pomeron trajectory can be extracted from the differential elastic scattering cross section as it is sensitive to α' (see Eq. (2.25)). The Pomeron trajectory has the following functional form[2]

$$\alpha_{\mathbb{P}}(t) = 1.08 + 0.25\ \text{GeV}^{-2}\ t\,. \tag{2.28}$$

The description of total cross sections with these two Regge exchanges is universal though. It successfully describes also $\pi p, Kp$ and np scattering cross sections with the same exponents, ϵ and η, but different couplings. It is note-worthy, that this high-energy behaviour ultimately leads to the violation of the Froissart-Martin bound $\sigma_{\text{tot}} < A \ln^2 s$, derived using unitarity and the partial wave expansion. This violation however happens not before energies reach the Planck scale! That is the reason why ϵ is expected to be energy dependent, although only very slightly, to preserve unitarity. Multiple Pomeron exchanges are known to be able to tame this asymptotic rise.

2.3 QCD

Quantum Chromodynamics (QCD) is the component of the Standard Model that describes the strong interactions. It is a theory formulated in terms of quarks and gluons at the Lagrangian level, but observed in terms of baryons and mesons in

[2] The same authors provide in Ref. [7] an updated form of the trajectory.

nature. Therefore observations in hadron spectroscopy triggered the formulation of the quark model. Confirmation of that model has been deduced from deep inelastic scattering experiments. Subsequent measurements have so far verified QCD in various quantitative test. More information on QCD and Jets can be found in Refs. [8–10].

2.3.1 QCD-Lagrangian

QCD is defined as a field theory by its Lagrangian density [11],

$$\mathcal{L}_{\text{QCD}} = \sum_{f=1}^{n_f} \bar{\psi}_i^f \left[i\not{D}_{ij} - m_f \delta_{ij} \right] \psi_j^f - \frac{1}{4} F_{\mu\nu,a} F_a^{\mu\nu} + \mathcal{L}_{\text{gauge}} + \mathcal{L}_{\text{ghost}} \,, \tag{2.29}$$

where the abbreviations,

$$\not{D}_{ij} = \gamma^\mu D_{\mu,ij} = \gamma^\mu [\partial_\mu \delta_{ij} + ig A_{\mu,a} (T_a)_{ij}] \tag{2.30}$$

for the covariant derivative D_μ, and

$$F_{\mu\nu,a} = \partial_\mu A_{\nu,a} - \partial_\nu A_{\mu,a} - g C_{abc} A_{\mu,b} A_{\nu,c} \tag{2.31}$$

for the field strength tensor have been used. Greek letters indicate Lorentz indices and latin letters colour indices. Letters from the beginning of the alphabet, abc, are in the range 1 to $N_C^2 - 1$, whereas the other latin indices are from 1 to N_C. The Lagrangian is a function of the spinor fields $\psi_f(x)$ (quarks) and the vector field $A(x)$ (gluon). The first two terms are invariant under local $SU(N_C)$ gauge transformations, with $N_C = 3$ in QCD. f is the summation over independent quark fields, *i.e.* $n_f = 6$ in the standard model. g is the coupling constant of QCD and C_{abc} are the structure constants of $SU(N_C)$ which define its Lie algebra. Usually one defines the coupling in analogy with the fine structure constant of QED to be $\alpha_s = \frac{g^2}{4\pi}$. Perturbation theory is not applicable without fixing a particular choice of gauge. This is done in the term $\mathcal{L}_{\text{gauge}}$ which is needed to define the gluon propagator. $\mathcal{L}_{\text{ghost}}$ introduces a complex scalar field, the ghost fields, which are needed to cancel unphysical degrees of freedom that would otherwise propagate in covariant gauges.

2.3.2 Asymptotic freedom and confinement

The most puzzling features of the strong interaction can be summarised by two terms: *Confinement* and *asymptotic freedom* [13, 14]. The first one explains, why quarks and gluons are not observed at macroscopic distances. The latter one is the reason why perturbation theory is applicable at high energies. QCD is able to accommodate both features of strong interactions by making the forces between quarks a function of the distance. The coupling constant is said to run, being large at low energy and becoming smaller at high energy.

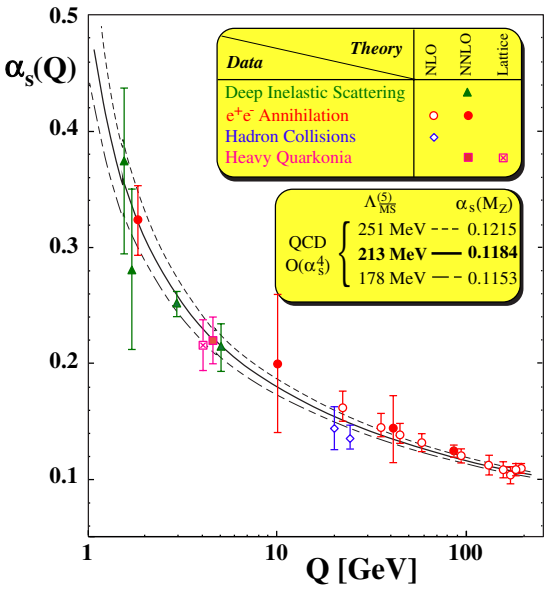

Figure 2.3: Experimental tests of the running coupling in QCD. Taken from Ref. [12].

The concept of a running coupling has to be introduced once higher order terms in the perturbation series are computed. There, ultraviolet divergences are encountered, which are absorbed into the couplings and fields at a *renormalisation scale* μ. Physical observables, however, must not depend on this arbitrary scale, as the Lagrangian of QCD makes no mention of it. To illustrate that, consider a dimensionless physical observable $\mathcal{R}$ depending on α_s and a single energy scale Q^2. If this scale is large enough, all masses can be set to zero. $\mathcal{R}$ can only be a function of the dimensionless quantities Q^2/μ^2 and $\alpha_s(\mu^2)$. The μ-independence of $\mathcal{R}$ can be expressed as

$$\mu^2 \frac{\mathrm{d}}{\mathrm{d}\mu^2} \mathcal{R}\left(\frac{Q^2}{\mu^2}, \alpha_s(\mu^2)\right) = \left[\mu^2 \frac{\partial}{\partial \mu^2} + \mu^2 \frac{\partial \alpha_s}{\partial \mu^2} \frac{\partial}{\partial \alpha_s}\right] \mathcal{R} \stackrel{!}{=} 0\,. \tag{2.32}$$

Hence, any explicit dependence of $\mathcal{R}$ on μ must be cancelled by the μ-dependence of α_s. If one eliminates the presence of the second scale by setting $\mu^2 = Q^2$, all of the scale dependence in $\mathcal{R}(1, \alpha_s)$ enters through the coupling constant $\alpha_s(Q^2)$.

This scale dependence is predicted by the *renormalisation group equation* (RGE),

$$Q^2 \frac{\partial \alpha_s}{\partial Q^2} = \beta(\alpha_s)\,, \tag{2.33}$$

where β can be computed as a power series in α_s,

$$\beta\left(\alpha_s(Q^2)\right) = -\alpha_s^2(Q^2)\left(b_1 + b_2\alpha_s(Q^2) + \ldots\right)\,, \tag{2.34}$$

with $b_1 = \frac{33-2n_f}{12\pi}$ and $b_2 = \frac{153-19n_f}{24\pi^2}$. n_f is the number of active flavours at Q^2. Hence, for $n_f \leq 16$ the beta function has a negative sign, leading to a vanishing coupling constant at asymptotically large energies, *i.e. asymptotic freedom*. This is contrary to the beta function in QED, where the coupling increases with increasing energy. This behaviour in QCD can be made more explicit if Eq. (2.33) is solved in the 1-loop approximation, *i.e.* truncating the expansion for the beta function after α_s^2,

$$\alpha_s(Q^2) = \frac{\alpha_s(\mu^2)}{1 + \alpha_s(\mu^2)\; b_1 \ln \frac{Q^2}{\mu^2}}\,. \tag{2.35}$$

Eq. (2.35) also shows the divergence of α_s for small Q^2. The absolute value of the coupling constant however is not predicted and has to be obtained from experiment. It can therefore be regarded as *the* fundamental parameter. One typically chooses $\alpha_s(M_Z^2)$ as reference point to ensure that the perturbative description is valid.

Using $\alpha_s(M_Z^2) = 0.12$, α_s exceeds unity for $Q^2 < \mathcal{O}\,(0.1 - 1\text{ GeV})$, which signals the breakdown of perturbation theory. Alternatively to Eq. (2.35), α_s can be parameterised in terms of the dimensionful parameter Λ_{QCD},

$$\alpha_s(Q^2) = \frac{1}{b_1 \ln \frac{Q^2}{\Lambda^2_{\text{QCD}}}}\,, \tag{2.36}$$

which essentially defines the scale where the coupling constant diverges. Λ_{QCD} is not uniquely defined though, it depends on the renormalisation scheme as well as on the number of active flavours and the order to which the beta function is computed. At 4 loops, calculated in the $\overline{\text{MS}}$ scheme, its value is $\Lambda^{\overline{\text{MS}}}_{\text{QCD}} = 220$ MeV.

2.3.3 Infrared Safety

With the solution to the running coupling from Eq. (2.35), we can see how asymptotic freedom can help in a practical case. The perturbative expansion of the observable $\mathcal{R}$ from the previous section is

$$\mathcal{R}\left(\frac{Q^2}{\mu^2}, \frac{m_i^2}{\mu^2}, \alpha_s(\mu^2)\right) = \sum_{n=0}^{\infty} a_n \left(\frac{Q^2}{\mu^2}, \frac{m_i^2}{\mu^2}\right) \alpha_s^n(\mu^2)\,, \tag{2.37}$$

where the m_i denote the internal (quark) masses. One encounters that the coefficients, a_n, are large and even in many cases infrared (IR) divergent, due to the vanishing gluon mass. This divergence is independent of the value for $\alpha_s(\mu^2)$. Nevertheless a large class of quantities can be identified [15], which are *infrared safe*. These quantities do not depend on the long-distance behaviour of the underlying theory, their coefficients are IR finite and possess a finite limit for vanishing m_i, such that

$$\mathcal{R}\left(\frac{Q^2}{\mu^2}, \frac{m_i^2}{\mu^2}, \alpha_s(\mu^2)\right) = \mathcal{R}\left(\frac{Q^2}{\mu^2}, 0, \alpha_s(\mu^2)\right)\left\{1 + \mathcal{O}\left(\frac{m_i}{Q^2}\right)\right\}. \tag{2.38}$$

For such a quantity we can set $\mu^2 = Q^2$ and therefore put *all* scale dependence into α_s. If Q^2 is large, the coupling decreases and the perturbation series becomes better and better.

The simplest case where this can be studied in more detail is e^+e^- annihilation into hadrons, $e^+e^- \to q\bar{q}$. The $\mathcal{O}(\alpha_s)$ real corrections to that process, $e^+e^- \to q\bar{q}g$, will reveal the structure of these divergences. The total cross section is given by

$$\sigma^{q\bar{q}g} = \frac{4\pi\alpha^2}{s} \sum_q e_q^2 \int_0^1 \mathrm{d}x_1 \mathrm{d}x_2 C_F \frac{\alpha_s}{2\pi} \frac{x_1^2 + x_2^2}{(1-x_1)(1-x_2)}\,, \tag{2.39}$$

where $x_{1,2}$ are the energy fractions of the quark and anti-quark, respectively, *i.e.* $x_{1,2} = 2E_{q,\bar{q}}\sqrt{s}$. The group constant C_F is $\frac{4}{3}$ for QCD. The integrals in Eq. (2.39) are divergent along the boundaries $x_{1,2} = 1$. Since $1 - x_{1,2} = x_{2,1}E_g(1 - \cos\theta_{\{2,1\}g})/\sqrt{s}$, with E_g being the gluon energy and $\theta_{i,g}$ the angle between the quarks and the gluon. Hence, the singular behaviour stems from kinematic regions, where either the gluon is *soft* or *collinear* with the quark or anti-quark. The key point now is that these singularities, once regularised in e.g. dimensional

regularisation, cancel *exactly* against singularities that appear in the $\mathcal{O}(\alpha_s)$ virtual corrections. This leaves a finite, infrared and collinear (IRC) safe[3] total cross section.

This cancellation of soft and collinear singularities is not accidental though, it is subject of the Kinoshita, Lee and Nauenberg (KLN) theorem [16, 17]. It states that suitably defined inclusive quantities will be free of singularities in the massless limit. The relevant physical observation that justifies infrared safety is that the creation of a quark pair is a short-distance phenomenon, and is not expected to interfere quantum mechanically with the long-distance processes that produce hadrons from quarks. Consequently, the cross section can be thought of as a product of probabilities, one for quark pair creation (Born diagram plus calculable corrections), the other for the evolution of quarks to hadrons. In the fully inclusive cross section, we sum over all final-states. Then, because of the absence of interference between short and long-distance effects, the probabilities for hadrons to be produced from quarks sum to unity. This is also the justification for the separated phases during event generation, which will be discussed in Chapter 3.

2.3.4 Parton model and deep inelastic scattering

Hadrons are compound objects, made up of strongly interacting particles. However, once a scattering process occurs that has a relatively large scale in the process, > 1 GeV^2, the asymptotic freedom property of QCD permits that to be understood in terms of a scattering process of the more fundamental constituents - quarks and gluons (partons), which interact relatively weakly. The fundamental quantities that are needed for a calculation of such scattering processes are the *parton distri-*

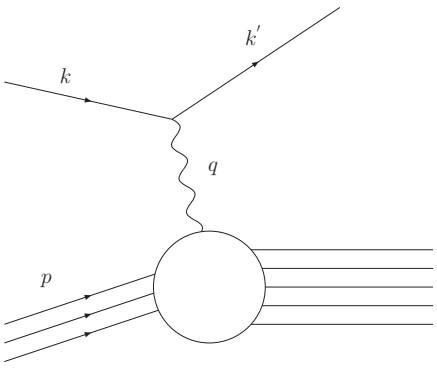

Figure 2.4: Deep inelastic lepton hadron scattering process $\ell h \to \ell X$.

[3] Up to now, only to $\mathcal{O}(\alpha_s)$

butions (PDFs). The concept of point
like constituents has been developed after the observation of Bjorken scaling in deep inelastic lepton-hadron scattering (DIS). Breaking of this scaling property was of the same importance, because it cannot be explained by the *naive parton model* but is a prediction of QCD.

The canonical example for the discussion of parton densities and the parton model is DIS. The example of electron proton scattering is used to briefly introduce the main points. Figure 2.4 shows the scattering process, where the lepton scatters off the proton leaving some hadronic state X. The incoming and outgoing lepton four-momenta are labelled by k^μ and k'^μ respectively. The proton by p^μ and the momentum transfer by $q^\mu = k^\mu - k'^\mu$. With these definitions the standard DIS variables are

$$\begin{aligned} Q^2 &= -q^2\,, & \nu &= p\cdot q\,, \\ x &= \frac{Q^2}{2\nu}\,, & y &= \frac{q\cdot p}{k\cdot p}\,. \end{aligned} \tag{2.40}$$

The lepton scattering cross section can be parameterised in terms of the two *structure functions* $F_{1,2}(x, Q^2)$. Neglecting the mass of the proton, which is justified when working in the *infinite momentum frame*, this expression yields

$$\frac{\mathrm{d}^2\sigma}{\mathrm{d}x\;\mathrm{d}Q^2} = \frac{4\pi\alpha_s^2}{Q^2}\left[\left(1+(1-y)^2\right)F_1 + \frac{1-y}{x}\left(F_2 - 2xF_1\right)\right]. \tag{2.41}$$

In the *Bjorken limit*, where $Q^2, \nu \to \infty$ with x fixed, these structure functions are observed to obey an approximate scaling law [18]. That means they depend only on the dimensionless variable x. This implies that the virtual photon scatters off point like constituents, since otherwise a scale associated with the length scale of the constituents would appear. From that observation the parton model has evolved, where the photon scatters off a point like constituent which is moving parallel with the proton and carries a fraction ξ of its momentum. Using this model, the cross section from Eq. (2.41) can be calculated using the matrix element for the process $e^- q \to e^- q$,

$$\frac{\mathrm{d}^2\hat{\sigma}}{\mathrm{d}x\;\mathrm{d}Q^2} = \frac{4\pi\alpha_s^2}{Q^2}\left[1+(1-y)^2\right]\;\frac{e_q^2}{2}\;\delta(x-\xi)\,. \tag{2.42}$$

The "hat" indicates that this is a partonic cross section. The partonic structure functions can be obtained by comparing Eqs. (2.41) and (2.42),

$$\hat{F}_2 = 2x\hat{F}_1 = xe_q^2\ \delta(x-\xi)\,. \tag{2.43}$$

Measurements however show that they are rather a distribution in x and not a delta function, which then finally lead to the formulation of the *naive parton model*:

- partons carry a range of momentum fraction, where $f_q(\xi)\mathrm{d}\xi$ represents the probability that a quark q carries a momentum fraction between ξ and $\xi+\mathrm{d}\xi$ and $\xi \in [0,1]$. $f_q(x)$ are the *parton distributions*.
- the virtual photon scatters incoherently off the proton constituents

The structure functions can now be written as

$$F_2(x) = 2xF_1(x) = \sum_{q,\bar{q}} \int_0^1 \mathrm{d}\xi\ f_q(\xi) xe_q^2\ \delta(x-\xi) = \sum_{q,\bar{q}} e_q^2\ f_q(x)\,. \tag{2.44}$$

The relation between F_2 and F_1 is known as the *Callan-Gross relation* and is a manifestation of the spin-$\frac{1}{2}$ property of the quarks. The two terms of Eq.(2.41) correspond to the absorption of transversely (F_1) and longitudinally ($F_2 - 2xF_1$)[4] polarised virtual photons. The absence of the second term follows from the fact that spin-$\frac{1}{2}$ particles cannot absorb longitudinally polarised vector bosons.

It is note-worthy that the DIS process doesn't specify the nature of the hadronic state X. This *inclusive* definition means that for example diffractive processes are included. Therefore whenever a parton distribution is used to calculate a cross section, the contribution from diffractive scattering is implicitly included.

2.3.5 Perturbative QCD and the parton model

Perturbative QCD beyond leading order *breaks* Bjorken scaling by logarithms of Q^2. This is due to the fact that the parton can acquire large transverse momentum by emission of a gluon. The probability for a emission with transverse momentum

[4] only in the Bjorken limit

k_T is proportional to $\alpha_s \frac{\mathrm{d}k_T^2}{k_T^2}$ at large k_T. Going up to the kinematical limit, $k_T^2 \sim Q^2$, this gives rise to terms $\sim \alpha_s \log Q^2$, which break scaling. Taking the $\mathcal{O}(\alpha_s)$ corrections from quarks ($\gamma^* q \to qg$) to the parton model into account, leads to

$$\hat{F}_2 = e_q^2 x \left[\delta(1-x) + \frac{\alpha_s}{2\pi}\left(P_{qq}(x) \ln \frac{Q^2}{\kappa^2} + C_q(x)\right)\right] . \tag{2.45}$$

Here the quark is assumed to have the full proton momentum, p. $P_{qq}(x)$ is the *splitting function* for the qqg Vertex, κ is used to regularise the collinear divergence at $k_T^2 = 0$. $C_q(x)$ is a finite and calculable function. The limit $k_T^2 \to 0$ corresponds to the long-range part of the interaction which is not calculable in perturbative QCD. It can't be subject to the KLN theorem, introduced in Sect. 2.3.3, because a quark and a collinear quark-gluon pair carrying the same momentum are *distinguishable* for a virtual photon. To obtain the proton structure function, the quark structure function, $\hat{F}_2$ has to be convoluted with a *bare* parton distribution, $f_{q,0}$ like in Eq. (2.44). Exactly as for the renormalisation of the coupling constant the singularities can now be absorbed into this bare distribution at a *factorisation scale* μ, which plays a similar role to the renormalisation scale. The *renormalised* parton distribution is then

$$f_q(x,\mu^2) = f_{q,0}(x) + \frac{\alpha_s}{2\pi} \int_x^1 \frac{\mathrm{d}\xi}{\xi} f_{q,0}(\xi) \left[P_{qq}\left(\frac{x}{\xi}\right) \ln \frac{\mu^2}{\kappa^2} + C_q\left(\frac{x}{\xi}\right)\right] + \ldots , \tag{2.46}$$

so that the structure function takes the form

$$F_2(x,Q^2) = x \sum_{q,\bar{q}} e_q^2 \int_x^1 \frac{\mathrm{d}\xi}{\xi} f_q(\xi,\mu^2) \left[\delta(1-\frac{x}{\xi}) + \frac{\alpha_s}{2\pi} P_{qq}\left(\frac{x}{\xi}\right) \ln \frac{Q^2}{\mu^2} + \ldots\right] . \tag{2.47}$$

This factorisation of short and long-distance contributions in DIS observables is a general feature that holds to all orders in perturbation theory [19]. It allows for the separation of all infrared sensitivity into the parton distributions. It is universal, *i.e.* independent of the particular hard scattering process.

One should note that in Eqs. (2.46) and (2.47) the finite contributions in $C_q(x)$ have been absorbed into the quark distribution f_q. This freedom of treating *finite* contributions is matter to the preferred *factorisation scheme*. The one above is the DIS scheme.

The full $\mathcal{O}(\alpha_s)$ result, including the gluon ($\gamma^* g \to q\bar{q}$) contribution, for F_2 in the $\overline{\text{MS}}$ scheme is given by

$$\begin{aligned} F_2(x,Q^2) = x \sum_{q,\bar{q}} e_q^2 \int_x^1 \frac{\mathrm{d}\xi}{\xi} \, f_q(\xi,Q^2) \left[\delta(1-\frac{x}{\xi}) + \frac{\alpha_s}{2\pi} \, C_q^{\overline{\text{MS}}}\left(\frac{x}{\xi}\right)\right] \\ + x \sum_{q,\bar{q}} e_q^2 \int_x^1 \frac{\mathrm{d}\xi}{\xi} \, f_g(\xi,Q^2) \left[\frac{\alpha_s}{2\pi} \, C_g^{\overline{\text{MS}}}\left(\frac{x}{\xi}\right)\right] . \end{aligned} \tag{2.48}$$

The functions C_q and C_g are the so-called *coefficient functions*. They are infrared safe and calculable in perturbation theory. They depend on the factorisation and renormalisation schemes and on the observable that is computed but are independent of the hadron that is considered in the scattering process.

A remarkable consequence of factorisation is that measuring parton distributions for one scale μ allows their prediction for any other scale μ', as long as both are large enough to ensure that $\alpha_s(\mu^2)$ and $\alpha_s(\mu'^2)$ are small[5]. The evolution of parton distribution is described by a set of integro-differential equations,

$$\frac{\mathrm{d}f_i(x,\mu^2)}{\mathrm{d}\ln\mu^2} = \sum_j \int_x^1 \frac{\mathrm{d}\xi}{\xi} \, P_{ij}\left(\frac{x}{\xi}, \alpha_s(\mu^2)\right) \, f_i(x,\mu^2) \,, \tag{2.49}$$

known as the Dokshitzer-Gribov-Lipatov-Altarelli-Parisi (DGLAP) equations [20–22]. P_{ij} are the splitting functions used before, which are calculable order by order in perturbation theory. A derivation can be obtained from Eq. (2.47). The right-hand side of that equation seems to have a μ dependence, which it cannot have. The scale dependence of the PDFs has to cancel all other scale dependencies exactly in the very same way than the scale dependence of α_s is obtained and finally described by the RGEs.

2.3.6 Hadronic cross sections in the parton model

A similar factorisation than present in DIS has not been rigorously proven for hadron-hadron scattering, but is generally employed for the calculation of cross sections. It can be carried out using the parton distributions, $f(x,Q^2)$, measured

[5] It is note-worthy, that the DGLAP description works down to very small scales ($Q \sim 0.4$ GeV), where α_s certainly exceeded unity.

in DIS. The general form of such cross sections, for the hadronic process $AB \to X_1 \dots X_n$ is given by

$$\sigma_{AB}(p_1, p_2) = \sum_{a,b} \int_0^1 \mathrm{d}x_1 \mathrm{d}x_2 \; \hat{\sigma}_{ab}(x_1 p_1, x_2 p_2) f_{a/A}(x_1, \mu^2) f_{b/B}(x_2, \mu^2) \,, \tag{2.50}$$

where $\hat{\sigma}_{ab}$ is the partonic cross section for incoming partons a and b and x_1 and x_2 their longitudinal momentum fractions with respect to the incoming hadrons. The partonic cross section can be calculated using

$$\mathrm{d}\hat{\sigma}_{ab} = \frac{\overline{\sum} \left|\mathcal{M}\right|^2 (p_a p_b \to p_1 \dots p_n)}{F} \, \mathrm{d}\Phi_n \,. \tag{2.51}$$

$\overline{\sum} \left|\mathcal{M}\right|^2$ is the squared Feynman amplitude of the considered process summed over all final-state quantum numbers and averaged over initial-state quantum numbers for the process. The incoming particle flux is taken into account by the factor F, which is given by $F = 4\sqrt{(p_a \cdot p_b)^2 - p_a^2 p_b^2}$. The number of possible final-states is counted by $\mathrm{d}\Phi_n$, the Lorentz invariant phase space element (LIPS) for n outgoing partons,

$$\mathrm{d}\Phi_n(p_a p_b \to p_1 \dots p_n) = (2\pi)^4 \delta^4 \left(p_a + p_b - \sum_{k=1}^{n} p_k \right) \prod_{k=1}^{n} \frac{\mathrm{d}^3 \mathbf{p}_k}{(2\pi)^3 2E_k} \,. \tag{2.52}$$

2.4 Jets

This section is dedicated to the objects that are used to study - and emerge from - QCD, the *jets*. After a brief introduction, the theoretical basis of jets will be discussed before challenges and solutions to jet finding are described.

2.4.1 Introduction

In the mid 1950s, sprays of particles emerging from the collisions of energetic cosmic rays in an emulsion target have been observed. The particles had relatively large and nearly parallel longitudinal momenta and were called *jets*. In the naive parton model it was assumed that a fast moving hadron can be regarded as a

bunch of more-or-less collinear partons. In a very similar way one can assume that a fast moving parton may lead to a spray of more-or-less collinear hadrons. This hypothesis is called *collinear fragmentation*. In $e^+e^- \to q\bar{q}$ reactions this would lead to the production of two back-to-back jets. Experimentally, most events contain indeed 2 jets, where a typical event is shown in Fig. 2.5. But there is also a small contribution from 3 and 4 jets etc. These appear once higher orders, thus more partons in the final-state, are considered. They lead to the problems of IRC safety, discussed in Sect. 2.3.3, and have to be treated carefully.

The decay products of an energetic parton are of course not infinitely well collimated which makes it necessary to establish *jet algorithms*, which map the outgoing hadrons to a (smaller) number of jets. Hence, they provide a way of projecting away the multiparticle dynamics of an event so as to leave a simpler quasi-partonic picture of the underlying hard scattering event. It was shown that such algorithms can be applied without loosing IRC safety [15]. They have to fulfil general conditions that any IRC safe observable has to fulfil. To be useful, they should also be relatively insensitive to the formation of hadrons, the *hadronisation* process. The reason for that is that jet algorithms are used to compare distributions at parton and hadron level, thus being applied to partons *and* hadrons or ultimately to their representation in experiment, detector cells.

2.4.2 Infrared safe observables

The total cross section for the e^+e^- annihilation into hadrons is guaranteed to be an IRC safe quantity by the KLN theorem. The amount of information it contains however is limited, it tells nothing about the distribution of hadrons in the final-state. Infrared safe cross sections or observables can be understood as generalisation of the KLN theorem to less inclusive quantities.

All possible divergences arise from the collinear or soft momentum configurations that were explicitly discussed in Sect. 2.3.3 for the $e^+e^- \to q\bar{q}g$ case. The general requirements for IRC safe observables can therefore be deduced.

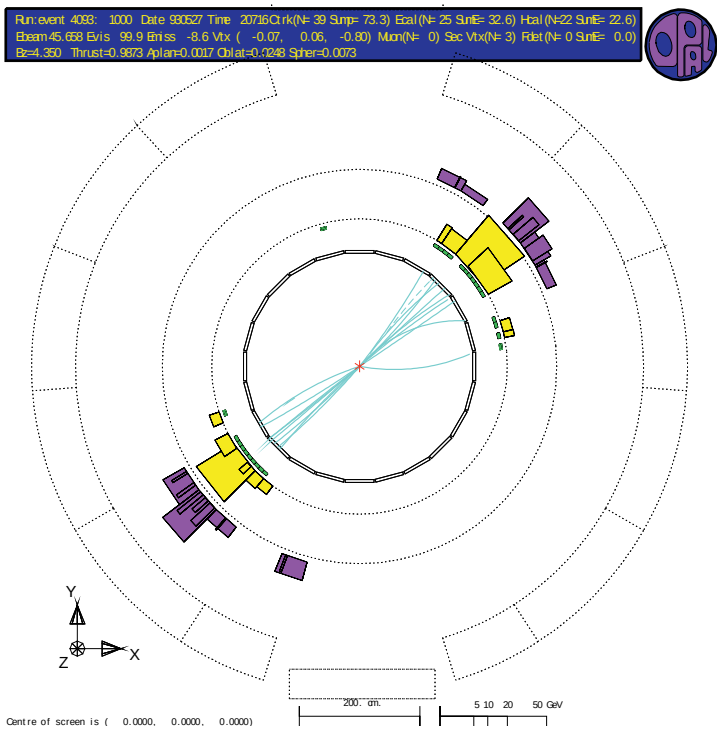

Figure 2.5: Two jet event in e^+e^- annihilation from the Opal Collaboration.

e^+e^- collisions

Consider an observable, $\mathcal{R}$, defined as,

$$\mathcal{R} = \sum_{n=2}^{\infty} \frac{1}{n!} \int \mathrm{d}\Phi_n \frac{\mathrm{d}\sigma}{\mathrm{d}\Phi_n} \, \mathcal{S}_n(p_1^\mu, \ldots, p_n^\mu) \,, \tag{2.53}$$

where $\mathrm{d}\Phi_n$ is the lorentz invariant phase space element already discussed in previous sections. On the assumption that all partons are not distinguished, the symmetrisation factor $\frac{1}{n!}$ is included. The functions $\mathcal{S}_n$ define the measurement to be made. Note, that for $\mathcal{S}_n = 1$ the total cross section is recovered.

Once the $\mathcal{S}_n$ fulfil certain requirements, the cancellation of infrared singularities is guaranteed to all orders. On the assumption that the $\mathcal{S}_n$ are invariant under

interchange of their arguments, this property may be expressed as

$$\mathcal{S}_{n+1}(p_1^\mu, \ldots, (1-\lambda)p_n^\mu, \lambda p_{n+1}^\mu) = \mathcal{S}_n(p_1^\mu, \ldots, p_n^\mu)\,, \tag{2.54}$$

for $0 \leq \lambda \leq 1$. The definition in Eq.(2.54) implies, that any measurement should not distinguish between a final-state, where two particles are collinear and one in which these particles are replaced by one particle carrying the sum of the momenta of these particles. Similarly, the measurement should not distinguish between a final-state in which one particle has zero momentum and the final-state in which this particle is omitted entirely. Typical examples for these observables at e^+e^- colliders are the *event shape* variables, like thrust or spherocity. They literally define the *shape* of an event in contrast to the jet finding procedure that is done by jet algorithms. In the case of uniformly distributed hadrons for example, a jet algorithm would always define jets, whereas the event shapes would disentangle that shape from e.g. a pencil-like.

Hadronic collisions

For hadronic collisions, $AB \to X$, the general form of a IRC finite quantity, $\mathcal{R}$, may be written as,

$$\begin{aligned}\mathcal{R} = &\sum_{n=2}^{\infty} \int \mathrm{d}x_1 \mathrm{d}x_2 \sum_{a,b} f_{a/A}(x_1, \mu^2)\; f_{b/B}(x_2, \mu^2) \\ &\times \int \mathrm{d}\Phi_n \frac{\mathrm{d}\hat{\sigma}}{\mathrm{d}\Phi_n}\; \mathcal{S}_n(p_1^\mu, \ldots, p_n^\mu)\,,\end{aligned} \tag{2.55}$$

where $\mathcal{S}_n$ has the property of Eq. (2.54). x_1, x_2 denote the longitudinal momentum fractions of the incoming partons a and b. The "hat" on $\mathrm{d}\hat{\sigma}$ indicates that IRC sensitivity arising from the the initial-state is factored into the parton distributions, as discussed in Sect. 2.3.5. In addition to Eq. (2.54), partons that are collinear with one of the beam momenta p_A^μ or p_B^μ, should not affect the measurement, *i.e.*

$$\mathcal{S}_{n+1}(p_1^\mu, \ldots, p_n^\mu, \lambda p_A^\mu) = \mathcal{S}_{n+1}(p_1^\mu, \ldots, p_n^\mu, \lambda p_B^\mu) = \mathcal{S}_n(p_1^\mu, \ldots, p_n^\mu)\,. \tag{2.56}$$

Jet cross sections

The usage of jets also allows for a more exclusive measurement without loosing IRC safety. This is somehow obvious as jets are the manifestation of partons in nature, where it is expected that no divergences appear.

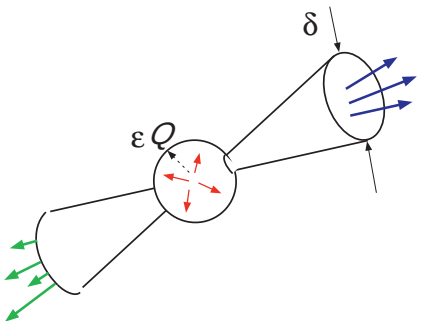

Figure 2.6: Visualisation of the jet definition of Ref. [15].

One of the first attempts to define jet cross sections in e^+e^-annihilation [15], classified an event as two-jet-like if all but a fraction ϵ of the total available energy is contained in a pair of *cones* of half-angle δ. The two-jet cross section can then be obtained by integrating the matrix elements over the regions of phase space that are determined by ϵ and δ. At leading order the two-jet and total cross section are identical. At $\mathcal{O}(\alpha_s)$ one has to integrate Eq. (2.39) over the appropriate range of x_1, x_2, which leads to the 2- and 3-jet rates

$$\begin{aligned} f_2 = \frac{\sigma_2}{\sigma_{\text{tot}}} &= 1 - 8C_F \frac{\alpha_s}{2\pi} \left\{ \ln\frac{1}{\delta} \left[\ln(\frac{1}{2\epsilon} - 1) - \frac{3}{4} + 3\epsilon \right] \right. \\ &\qquad \left. + \frac{\pi^2}{12} - \frac{7}{16} - \epsilon + \frac{3}{2}\epsilon^2 + \mathcal{O}\left(\delta^2 \ln\epsilon\right) \right\} \\ f_3 &= 1 - f_2 \,, \end{aligned} \tag{2.57}$$

where only the terms which are important for small δ are shown. The residual soft and collinear singularities are revealed for $\epsilon, \delta \to 0$. In a measurement ϵ and δ would correspond to the finite energy resolution and granularity of a particle detector and therefore never vanish.

2.4.3 Jet algorithms

The jet definition introduced in the previous section is the forerunner of a entire class of jet algorithms, known as *cone type* algorithms [15, 23, 24]. They are nowadays widespread at hadron colliders. Recent implementations are based on identifying energy flow into cones in rapidity y and azimuth ϕ. To obtain final

jets, various steps of iteration, merging and splitting of cones are used. The second large class of algorithms is the *sequential cluster* or *sequential recombination* type [25–30]. They introduce a distance measure between particles and repeatedly recombine the closest pair until all are sufficiently well separated.

Cone algorithms

Cone jet algorithms try to find an angular cone around some direction of dominant energy flow, by taking particles as *seeds*, *i.e.* trial cone directions. Then by evaluating the four-momentum sum of all particles falling into the cone, the algorithm defines a new trial direction for it. This procedure is iterated until the direction no longer changes, *i.e.* a *stable cone* is found. Hence, stable cones have the property, that the cone axis p^μ_{axis} coincides with the axis defined by the four-momentum sum of all contained particles p^μ_{sum}. One therefore has to define a measure of angular distance, d, so that the requirement of a stable cone can be expressed as

$$d(p^\mu_{\text{sum}}, p^\mu_{\text{axis}}) = 0\,, \quad \text{with } p^\mu_{\text{sum}} = \sum_i p^\mu_i \cdot \Theta\left(R - d(p^\mu_i, p^\mu_{\text{axis}})\right)\,, \tag{2.58}$$

with R being the angular resolution or *cone radius*. A typical choice for the distance measure is $d^2(p,q) = (y_p - y_q)^2 + (\phi_p - \phi_q)^2$.

To ensure collinear safety the selection of seed particles is not allowed to be restricted, all particles must be considered. However, if any particle can act as a seed, it has to be ensured that the addition of an infinitely soft particle cannot lead to a new stable cone. Otherwise the algorithm is IR unsafe. It turned out that traditional cone type algorithms indeed suffered from this problem in certain configurations with two particles being at the edge of a stable cone and no particle in between. Adding artificial *midpoint* seeds between pairs of stable cones and searching for new stable cones seemed to be a solution. The identification of certain triangular configurations, where the midpoint solution fails as well, showed that these algorithms are only IRC safe to a certain order in α_s.

The naive iterative cone algorithms for example are unreliable from $\mathcal{O}\left(\alpha_s^3\right)$ (or $\mathcal{O}\left(\alpha_s^2\alpha_{\text{EM}}\right)$), which means that at $\mathcal{O}\left(\alpha_s^4\right)$ first stable cones are missed. For vector boson production + 2 jets for example, this means that the last meaningful order

is the LO calculation!

It was only recently [24], that an infrared safe cone algorithm was proposed, which is both reasonably fast $\mathcal{O}(N^2 \ln N)$ *and* IRC safe to all orders.

Sequential recombination algorithms

In contrast to the cone type algorithms, all sequential recombination algorithms (SRAs) are IRC safe and have rather simple definitions. Their drawback however was the apparent slowness in high-multiplicity hadron collider environments. The clustering of N particles required $\mathcal{O}(N^3)$ operations. This speed issue has been solved in Ref. [31] by reducing the clustering problem to a (solved) problem in computational geometry. Running times could be reduced to $\mathcal{O}(N \ln N)$.

The most widely used algorithm is the k_t jet-finder [29, 30]. In its longitudinally invariant formulation, suitable for hadron colliders, it is defined as follows.

1. Calculate the k_t-distance $d_{ij} = \min(k_{T,i}^2, k_{T,j}^2) \cdot R_{ij}^2$ for each pair of particles i, j, where $R_{ij}^2 = (\eta_i - \eta_j)^2 + (\phi_i - \phi_j)^2$ and $k_{T,i}$ is the transverse momentum of particle i. Also calculate the beam distance $d_{iB} = k_{T,i}^2$.

2. Find the minimum, $d_{\min}$, of all d_{ij} and d_{iB}.

   - If $d_{\min}$ is a d_{ij}, merge particles i and j into a single particle. The resulting four-momentum is the sum of both.
   - If $d_{\min}$ is a d_{iB}, declare the particle i to be a final jet and remove it from the list.

3. Go back to step 1 until all particles are clustered.

A variant that is often used, introduces a jet resolution threshold d_{cut}. The clustering procedure is stopped there, once all distance measures are above that threshold. The number of clustered jets will therefore depend on the value of d_{cut}. Hence, it can be seen as a resolution parameter where $d_{\text{cut}} \equiv d_{\max}$ would lead to only one reconstructed jet, whereas $d_{\text{cut}} \to 0$ corresponds to the mode where all particles are clustered. Typical observables to examine the jet structure are for example the

number of jets as a funtion of the resolution parameter, or the resolution parameter, Y_n, at which n-jet events become $n + 1$-jet events.

Chapter 3

Event Generators

"First Commandment of Event Generation:
Thou shalt never believe event generation is easy."
— Leif Lönnblad, April 21, 2008

3.1 Introduction

The model for the underlying event has been implemented in the context of a general-purpose event generator. For a coherent picture, the basics of these programs are reviewed in this chapter. This is done for Herwig++ [32–36], the event generator of actual use. There are several other successful programs [37–42] available, which are not discussed in detail here.

Herwig++ is a general-purpose event generator for the simulation of high-energy lepton-lepton and hadron-hadron collisions with special emphasis on the accurate simulation of QCD radiation. It builds upon the heritage of the HERWIG program [37, 43–47], while providing a much more flexible structure for further development. It is based on ThePEG [48], which is a framework for event generators. ThePEG provides all parts of the event generator infrastructure that do not depend on the physics models used as a collection of modular building blocks. The specific physics models of Herwig++ are implemented on top of these.

It is useful to start by recalling the main features of a generic hard, high-momentum transfer, process in the way it is simulated by Herwig++. The processes involved can be divided into a number of stages corresponding to increasing time and distance scales, as already mentioned in Sect. 2.3.3:

1. *Elementary hard subprocess.* In the hard process the incoming particles interact to produce the primary outgoing fundamental particles. This interaction can involve either the incoming fundamental particles in lepton collisions or partons extracted from a hadron in hadron-initiated processes. In general this is computed at leading order in perturbation theory, although work is ongoing to include higher-order corrections [49–52]. The energy scale of the hard process, Q^2, together with the colour flow between the particles, sets the initial conditions for the production of QCD radiation in the initial- and final-state parton showers.

2. *Initial- and final-state parton showers.* The coloured particles in the event are perturbatively evolved from the hard scale of the collision to the infrared cut-off. This occurs for both the particles produced in the collision, the *final-state shower*, and the initial partons involved in the collision for processes with incoming hadrons, the *initial-state shower*. The coherence of the emission of soft gluons in the parton showers from the particles in the hard collision is controlled by the colour flow of the hard collision. Inside the parton shower, it is simulated by the angular ordering of successive emissions.

3. *Decay of heavy objects.* Massive fundamental particles such as the top quark, electroweak gauge bosons, Higgs bosons, and particles in many models of physics beyond the Standard Model, decay on time-scales that are either shorter than, or comparable to that of the QCD parton shower. Depending on the nature of the particles and whether or not strongly interacting particles are produced in the decay, these particles may also initiate parton showers both before and after their decay. One of the major features of the Herwig++ shower algorithm is the treatment of radiation from such heavy objects in both their production and decay. Spin correlations between the production and decay of such particles are also correctly treated.

4. *Multiple scattering.* For large centre-of-mass energies the parton densities

are probed in a kinematic regime where the probability of having multiple partonic scatterings in the same hadronic collision becomes significant. For these energies, multiple scattering is the dominant component of the underlying event that accompanies the main hard scattering. These additional scatterings take place in the perturbative regime, above the infrared cut-off, and therefore give rise to additional parton showers. This is the part of the simulation that has been developed and that is described in this thesis.

5. *Hadronisation.* After the parton showers have evolved all partons involved in hard scatterings, additional scatters and partonic decays down to low scales, the final-state typically consists of coloured partons that are close in momentum space to partons with which they share a colour index, their colour 'partner'. Note, that this assignment is unique in the large N_c limit. Herwig++ uses the cluster hadronisation model[44] to project these colour–anticolour pairs onto singlet states called clusters, which decay to hadrons and hadron resonances.

6. *Hadron decays.* The hadron decays in Herwig++ are simulated using a matrix element description of the distributions of the decay products, together with spin correlations between the different decays, wherever possible. The treatment of spin correlations is fully integrated with that used in perturbative production and decay processes so that correlations between the production and decay of particles like the τ lepton, which can be produced perturbatively but decays hadronically, can be treated consistently.

3.2 Monte Carlo methods

Before the details of the different phases of event generation are discussed, the very basics of it, the *Monte Carlo* method, shall be introduced and briefly discussed. The method and its name go back to Ref. [53].

3.2.1 Integration

As will be seen in the next section, one vital ingredient to event generation is the calculation of the cross section for the underlying hard process. This involves the calculation of high-dimensional integrals, where both the integrand, $f(\mathbf{x})$, and the integration volume, V, are not necessarily well behaved,

$$I = \int_V f(\mathbf{x}) \, \mathrm{d}^n x \,. \tag{3.1}$$

The most convenient way solve this integral is stochastic sampling of the integrand using uniformly distributed pseudo random numbers, $\mathbf{x}_i$,

$$I \approx \; I_{\mathrm{MC}} := V \cdot \langle f \rangle = V \cdot \frac{1}{N} \sum_{i=1}^{N} f(\mathbf{x}_i) \,, \tag{3.2}$$

where the integral is simply the product of the average value of the integrand times the integration volume. The uncertainty that is inherent to I_{MC} can be computed using the *variance* defined as $\mathrm{Var}\,[f] := \langle f^2 \rangle - \langle f \rangle^2$,

$$\mathrm{Var}\,[I_{\mathrm{MC}}] = \mathrm{Var}\left[\frac{V}{N} \sum_{i=1}^{N} f(\mathbf{x}_i)\right] = \frac{V^2}{N^2} \mathrm{Var}\left[\sum_{i=1}^{N} f(\mathbf{x}_i)\right] = \frac{V^2}{N} \mathrm{Var}\,[f] \;, \tag{3.3}$$

where in the last step the fact that the $\mathbf{x}_i$ are independent has been exploited. This simple result has several implications. First, the uncertainty is independent of the dimension of the integration volume. It will always scale like $\propto \frac{1}{\sqrt{N}}$. This is the main advantage compared to other numerical integration algorithms, which are typically highly dependent on the dimensionality of the problem. Second, the uncertainty is proportional to the variance of the integrand. From that observation you can immediately deduce two ways of improving the accuracy:

1. The so called *Stratified Sampling* relies on the partitioning of the integration volume into smaller volumes, where the variance of the function is smaller.

2. The *Importance Sampling* simply modifies the integrand *and* the distribution of sampling points in the same way, such that this modification cancels but leaves a integrand with less fluctuations and therefore smaller variance.

3.2.2 Event Generation

So far the integral can be computed, but the points $\mathbf{x}_i$, which are analogous to *events*, *i.e.* kinematic configurations, are uniformly distributed. Each of them however has a corresponding weight $w_i = \frac{V}{N} f(\mathbf{x}_i)$. The sum of these weights is the integral value. If these events are accepted with the probability

$$P_i = \frac{w_i}{\max(w_i)}\,, \tag{3.4}$$

they will be distributed in the same way than the initial integrand was. This is also known as the *Acceptance and Rejection method*. But also refers to an *unweighting* of events, because after that procedure, all events have equal weight.

3.3 Elementary Hard Process

The elementary hard process is the scattering process of fundamental particles with the highest scale in the event. The generation of this scattering process, *i.e.* the determination of the momenta of the external particles, their flavour, colour flow etc. is done using the Monte Carlo technique introduced in the previous Section. The corresponding integral that is used in that process is the standard expression for hadronic cross sections from Sect. 2.3.6,

$$\begin{aligned}\sigma = &\sum_{a,b} \int \mathrm{d}x_1 \mathrm{d}x_2 \; \mathrm{d}\Phi_n \; f_{a/p1}(x_1, Q^2) \; f_{b/p2}(x_2, Q^2) \\ &\times \frac{1}{2\hat{s}} \; \theta(\text{cuts}) \; \overline{\sum} \left|\mathcal{M}\right|^2 (p_a p_b \to p_1 \dots p_n) \quad .\end{aligned} \tag{3.5}$$

The longitudinal momentum fractions of the struck partons w.r.t. the incoming hadrons are $x_{1,2}$, $\mathrm{d}\Phi_n$ denotes the lorentz invariant phase space element, $f_{a/h}(x, Q^2)$ the PDFs for parton a in a hadron h and $\mathcal{M}$ is the amplitude of the process. This expression contains a theta function to account for kinematic cuts that are imposed on the outgoing particles.

ThePEG provides the infrastructure for doing this in a generic way. The PDFs are specific to Herwig++ or handled by the generic tool LHAPDF [54]. The matrix

elements are the remaining part to be implemented. In order to facilitate the process of adding new matrix elements, where needed, and to enable the generation of spin correlation effects [55–58], all matrix element calculations are based on the helicity libraries of ThePEG.

There are a few of them included for e^+e^- collisions, namely quark-antiquark and dilepton pair production, via interfering photon and Z^0 bosons, Z^0h^0 production and higgs production in vector boson fusion. In hadron-hadron collisions a few more are available:

- single W/Z production with up to one additional jet
- QCD dijet production
- heavy quark pair production
- prompt photon pair production as well as direct photon production in association with a jet
- s-channel higgs boson production, associated production with heavy vector bosons and associated production with a hard jet

As well as providing a native library of Standard Model processes and an interface to parton-level generators, which is discussed in the next section, Herwig++ also includes matrix elements for hard $2 \to 2$ collisions and $1 \to 2$ decays, arising in various models of new physics like the Minimal Supersymmetric Standard Model, the Randall-Sundrum Model and Minimal Universal Extra Dimensions. Details can be found in Ref. [59].

3.3.1 Les Houches interface

Nowadays there are a number of programs that automate these calculations, for a wide range of processes and high multiplicity final states. To enable the usage of such programs a standardised interface has been developed. These programs can generate parton-level events using either the original Les Houches Accord [60] or the subsequent extension [61], which specified a file format for the transfer of

the information between the matrix element generator and a general-purpose event generator.

Nevertheless, there are still some cases for which it is useful to handle all stages of the event generation process by one program. This is particularly true for processes in which spin correlations between the production and decay stages are significant *e.g.* those involving top quarks, τ leptons or other heavy unstable particles. Such correlation effects are hard to treat correctly if different programs handle different steps of the simulation process.

3.4 Parton Showers

The elementary hard process previously discussed, is typically calculated at the leading order (LO) in QCD. Next-to-leading order (NLO) calculations are available for many processes and even one further order in α_s, NNLO calculations are available in some special cases. Due to the roughly factorial growth in complexity one cannot expect much higher orders to be computed soon. There are kinematic regions, however, where higher-order terms are enhanced and cannot be neglected. The *collinear* and *soft* singularities discussed in Sects. 2.3.3 and 2.4.2 arose once higher orders were included. Parton shower algorithms give an approximate description of these effects to *all* orders, by working in the *collinear* limit and to leading logarithmic accuracy.

3.4.1 Single branching

The collinear enhancements are associated with a parton branching. Such a single branching of parton a into partons $b + c$ is depicted in Fig. 3.1. The blob represents the rest of the diagram. That means that a is an outgoing parton with $p_a^2 \equiv t > 0$, which is called *timelike* branching. The branching of an incoming parton is called

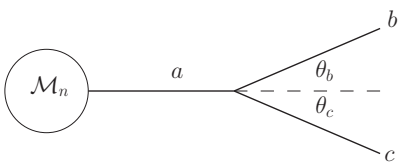

Figure 3.1: Timelike branching.

spacelike branching, due to the negative virtuality ($t < 0$) of the parton there. The opening angle is $\theta = \theta_b + \theta_c$. With the energy fractions

$$z = \frac{E_b}{E_a} = 1 - \frac{E_c}{E_a}\,, \tag{3.6}$$

t is given, in the collinear limit, by[1]

$$t = 2E_bE_c(1-\cos\theta) \;=\; z(1-z)E_a^2\theta^2\,. \tag{3.7}$$

θ can be expressed in terms of θ_a or θ_b as $\theta = \frac{\theta_b}{1-z} = \frac{\theta_c}{z}$. The different possible branchings are $g \to gg, g \to q\bar{q}$ and $q \to qg$. Using the small angle approximation one finds that the matrix element squared for these $n+1$ particle processes can be expressed in terms of the n particle matrix element as

$$|\mathcal{M}_{n+1}|^2 \sim \frac{4g^2}{t}\hat{P}_{ba}(z)\;\;|\mathcal{M}_n|^2\;. \tag{3.8}$$

The additional factors $\hat{P}_{ba}$ are the so-called unregularised, massless splitting functions related to the Altarelli-Parisi kernel from Eq. (2.49). For the three possible splittings, they are given by

$$\begin{aligned}
\hat{P}_{gg} &= 3\;\left[\frac{1-z}{z} + \frac{z}{1-z} + z(1-z)\right]\\
\hat{P}_{qg} &= \frac{1}{2}\;\left[z^2 + (1-z)^2\right]\\
\hat{P}_{qq} &= \frac{4}{3}\;\frac{1+z^2}{1-z}\,.
\end{aligned}$$

The differential cross section can be expressed using the splitting functions, as long as the dependence on the azimuthal angle ϕ of the branched parton is integrated out,

$$\mathrm{d}\sigma_{n+1} = \mathrm{d}\sigma_n\;\frac{\mathrm{d}t}{t}\mathrm{d}z\;\frac{\alpha_s}{2\pi}\hat{P}_{ba}(z)\,. \tag{3.9}$$

One finds that exactly the same formula also describes *spacelike* branchings. This universality of hierachical emissions is known as factorisation of collinear singularities.

[1] assuming that $p_b^2, p_c^2 \ll p_a^2$

3.4.2 Multiple branching

The aim of a parton shower algorithm is now to simulate according to Eq. (3.9) the ensemble effects of multiple parton branchings. Introducing the cut-off scale $Q_0^2 \equiv t_0$, imposes a resolution parameter, such that branchings that are softer or more collinear[2] than that, are not distinguishable from no branching at all, *i.e. unresolvable*. By invoking unitarity (requiring the sum of branching plus no-branching probabilities is one), the cancellation between the divergent parts of the splitting functions and the corresponding loop diagrams is implicitly handled. The main tool for the simulation of multiple branching is the *Sudakov form factor* [62], Δ(t),

$$\Delta_i(t) \equiv \exp\left[-\sum_j \int_{t_0}^{t} \frac{\mathrm{d}t'}{t'} \int \mathrm{d}z \frac{\alpha_s}{2\pi} \hat{P}_{ij}(z)\right] . \tag{3.10}$$

It is constructed such, that it gives the probability, for parton i, to evolve from t to t_0 without any *resolvable* emission. It is therefore given by one minus the n-emission probabilities, taken from Eq. (3.9), summed over all n.

The crucial ingredient for the Monte Carlo simulation is now the scale t' where the next branching occurs. The probability that parton i evolved from t to t' without resolvable emission is $\Delta_i(t)/\Delta_i(t')$. t' will have the correct probability distribution, if the equation

$$\frac{\Delta_i(t)}{\Delta_i(t')} = \mathcal{R} \tag{3.11}$$

is solved for t', with $\mathcal{R}$ being a uniformly distributed random number, $\mathcal{R} \in [0, 1]$. The algorithm is then recursively applied to each of the products of this branching.

The evolution of spacelike partons must take into account, that these partons are extracted from the incoming hadrons. This can be consistently done, by modifying Eq. (3.11) in the following way

$$\frac{f_i(x,t)\Delta_i(t')}{f_i(x,t')\Delta_i(t)} = \mathcal{R}\,, \tag{3.12}$$

[2] The boundaries of the z integration will also depend on t to regularise the divergences in $\hat{P}_{ba}(z)$ at $z = 1$ by $z < 1 - \epsilon(t)$

where parton i evolves backwards from (t', x) to (t, x).

The remaining variables to generate are the momentum fraction z and azimuthal angle ϕ. When averaging over ϕ, a simple uniform distribution $\phi \in [0, 2\pi]$ can be chosen. In the timelike case z will be distributed according to $\frac{\alpha_s}{2\pi} P_i(z)$, whereas in the spacelike case $((t', x') \to (t, x))$ according to $\frac{\alpha_s}{2\pi} \frac{P_i(z)}{z} f_i(x'/z, t)$.

3.4.3 Coherent branching

Such an algorithm of multiple branchings treats all leading collinear logarithms, arising from the $\frac{\mathrm{d}t}{t}$ term, correctly. However, there are also important soft logarithms, from $\frac{\mathrm{d}z}{z}$ terms, for gluon emissions. After averaging over azimuthal angle, their interference is completely destructive. It has been shown [43, 63–71] that whenever soft gluon emissions are considered, branchings that are not angular ordered do not give any leading logarithmic contributions.

A major success of the original HERWIG program was its treatment of soft gluon interference effects, in particular the phenomenon of *colour coherence*, via the angular ordering of emissions in the parton shower. Herwig++ simulates parton showers using the *coherent branching algorithm* of [72], which generalises that used in the original HERWIG program [43–45]. The new algorithm retains angular ordering as a central feature and improves on its predecessor in a number of ways, the most notable of these being:

- a covariant formulation of the showering algorithm, which is invariant under boosts along the jet axis;
- the treatment of heavy quark fragmentation through the use of mass-dependent splitting functions [73] and kinematics, providing a complete description of the so-called *dead-cone* region.

3.5 Hadronisation

The higher-order calculations mentioned above are all parton-level calculations that are not usable for e.g. detector simulation. They contain quarks and gluons at large energy scales. Parton showers evolve this high-scale, Q^2, outgoing partons to lower scales by successive parton emissions as long as perturbation theory is applicable, *i.e.* until some infrared cut-off value, Q_0^2 is reached. A mechanism is then needed to convert the partons to hadrons at the typical hadronic scale Λ^2_{QCD}. In Herwig++ this is done using the cluster model [44]. The basis of this model is the colour preconfinement property of the angular-ordered parton shower, described in Ref. [74]. There it was shown, that the parton shower evolution leads to a configuration of quarks and gluons from which one can form colourless clusters with a finite and Q^2-independent mass of order Q_0. As this happens still in the perturbative regime this phenomenon was called *pre*confinement. Confinement is the underlying dynamics of the conversion from clusters to observed hadrons. Associated with that is the transition from mass scales of $\mathcal{O}(Q_0)$ to typical hadron masses $\mathcal{O}(m_\pi, m_\rho)$.

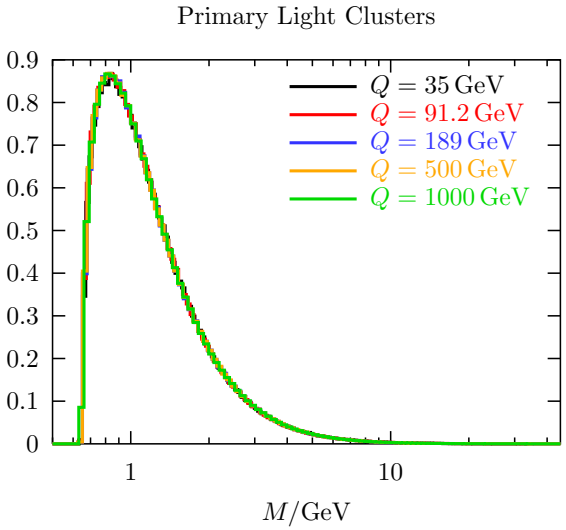

Figure 3.2: Primary cluster mass distribution in e^+e^- annihilation at various centre-of-mass energies Q for clusters containing only light quarks. Taken from Ref. [32].

The cluster model, which implements that transition, has the properties that it is local in the colour of the partons and independent of both the hard process and centre-of-mass energy of the collision [44, 45].

3.5.1 Gluon splitting and cluster formation

As a first step of the cluster hadronisation model, the gluons left at the end of the parton shower are non-perturbatively split into quark-antiquark pairs. Since, at

the end of the Herwig++ shower the gluons are given their constituent mass it is essential that this mass is heavier than twice the constituent mass of the lightest quark. The gluon is allowed to decay into any of the accessible quark flavours with a probability given by the available phase space for the decay. The decay itself is isotropic. Now, the event only contains colour connected (di)quarks and anti-(di)quarks. The colour singlets formed by these colour connected parton pairs are formed into clusters with the momentum given by the sum of the momenta of the constituent partons.

3.5.2 Cluster fission

Figure 3.2 provides the justification for regarding the clusters as highly excited hadron resonances, because the cluster mass spectrum is both universal (independent of the hard scale) and peaked at low masses. These clusters could then simply decay into the observed hadrons. There is however a small fraction of clusters that are too heavy for this to be a reasonable approach. These heavy clusters are therefore first split into lighter clusters before they decay.

A cluster is regarded *heavy* if its mass, M, is such that

$$M^{Cl_{\text{pow}}} \geq Cl_{\text{max}}^{Cl_{\text{pow}}} + (m_1 + m_2)^{Cl_{\text{pow}}}\,, \tag{3.13}$$

where Cl_{max} and Cl_{pow} are parameters of the model, and $m_{1,2}$ are the masses of the constituent partons of the cluster. In order to improve the description of the production of bottom and charm hadrons, both Cl_{max} and Cl_{pow} can be set with distinct values for clusters containing light, charm and bottom quarks respectively.

For clusters that need to be split, a $q\bar{q}$ pair is selected and taken from the vacuum. Only up, down and strange quarks are chosen with separate probabilities, given as adjustable parameters. Once a pair is selected the cluster is decayed into two new clusters with one of the original partons in each cluster. Unless one of the partons is a remnant of the incoming beam particle the mass distribution of the new clusters is given by

$$M_i = m_i + (M - m_i - m_q) \cdot x(P)\,, \tag{3.14}$$

where m_q is the mass of the parton taken from the vacuum and $M_{i=1,2}$ are the masses of the clusters formed by the splitting. x is a random number distributed between $x_{\min} > 0$ and 1 according to $f(P) = 1/P$. The distribution of the masses of the clusters is controlled by the parameter P, which again can have different values for clusters containing light, charm or bottom quarks. In addition to the selection of the mass according to Eq. (3.14) the masses of the daughter clusters are required to be less than that of the parent cluster and greater than the sum of the masses of their constituent partons.

For clusters that contain a remnant of the beam particle in hadronic collisions a soft distribution is used for the masses of the clusters produced in the splitting. The mass of the soft clusters is given by

$$M_i = m_i + m_q + x, \tag{3.15}$$

where x is distributed between 0 and $M - m_1 - m_2 - 2m_q$ according to

$$\frac{\mathrm{d}P}{\mathrm{d}x^2} = e^{-bx} \ . \tag{3.16}$$

The faster decreasing exponential is used in contrast to Eq. (3.14), because that avoids a proliferation of transverse energy due to the many sequential decays of the typically high-mass remnant clusters.

3.5.3 Cluster decays

The final step is the decay of the cluster into a pair of hadrons. For a cluster of a given flavour $(q_1, \bar{q}_2)$ a quark-antiquark or diquark-antidiquark pair $(q, \bar{q})$ is extracted from the vacuum and a pair of hadrons with flavours $(q_1, \bar{q})$ and $(q, \bar{q}_2)$ is formed. The hadrons are selected from all the possible hadrons with the appropriate flavour based on the available phase space, spin and flavour of the hadrons.

The weight for the production of hadrons $a_{(q_1,\bar{q})}$ and $b_{(q,\bar{q}_2)}$ is

$$W(a_{(q_1,\bar{q})}, b_{(q,\bar{q}_2)}) = P_q w_a s_a w_b s_b p^*_{a,b}, \tag{3.17}$$

where P_q is the weight for the production of the given quark-antiquark or diquark-

antidiquark pair, $w_{a,b}$ are the weights for the production of individual hadrons and $s_{a,b}$ are suppression factors for the hadrons, which allow the production rates of individual meson multiplets, and singlet and decuplet baryons to be adjusted. The momentum of the hadrons in the rest frame of the decaying cluster,

$$p^*_{a,b} = \frac{1}{2M}\left[\left(M^2 - (m_a + m_b)^2\right)\left(M^2 - (m_a - m_b)^2\right)\right]^{\frac{1}{2}}, \tag{3.18}$$

measures the phase space available for two-body decay. If the masses of the decay products are greater than the mass of the cluster then the momentum is set to zero. The weight for the individual hadron is

$$w_h = w_{\text{mix}}(2J_h + 1), \tag{3.19}$$

where w_{mix} is the weight for the mixing of the neutral light mesons[3] and J_h is the spin of the hadron.

The amount of baryon production can be controlled directly by the following mechanism: If a cluster mass is sufficiently large that it can decay into the lightest baryon-antibaryon pair the parameter P_{qq} is used to decide whether to select a mesonic or baryonic decay of the cluster. The probabilities of selecting a mesonic decay or baryonic decay are $\frac{1}{1+P_{qq}}$ and $\frac{P_{qq}}{1+P_{qq}}$.

The final cluster decay is isotropic in the cluster rest frame. However, hadrons that contain a parton produced in the perturbative stage of the event retain the direction of the parton in the cluster rest frame, apart from a possible Gaussian smearing of the direction.

In practice there is always a small fraction of clusters that are too light to decay into two hadrons. These clusters are therefore decayed to the lightest hadron, with the appropriate flavours, together with a small reshuffling of energy and momentum with the neighbouring clusters to allow the hadron to be given the correct physical mass. The cluster with the smallest space-time distance that can absorb the recoil is used for that reshuffling.

[3] $w_{\text{mix}} = 1$ for all other particles.

3.6 Particle Decays

The hadronisation model has converted the colourless clusters into hadrons. However, most of them have such short lifetimes that they decay before they hit the first layer of a potential detector in a typical collider experiment. Therefore the decay of these hadrons has to be simulated as well. Herwig++ uses a sophisticated model of hadronic decays, as described in Refs. [75, 76]. The simulation is designed to have the following properties:

- a unified treatment of the decays of both the fundamental particles and the unstable hadrons, this is of particular importance for particles like the τ lepton, which, while a fundamental particle, is more like the unstable hadrons in the way it decays;
- up-to-date particle properties, *i.e.* masses, widths, lifetimes, decay modes and branching ratios together with a new database to store these properties to make updating the properties easier and the choices made in deriving them clearer;
- full treatment of spin correlation effects using the algorithm of Refs. [55–58] for the decay of all unstable particles, it is important that the same algorithm is used consistently in all stages of the program so that correlations between the different stages can be correctly included;
- a sophisticated treatment of off-shell effects for both the unstable hadrons and fundamental particles;
- a large range of matrix elements for hadron and τ decays including both general matrix elements based on the spin structures of the decays and specific matrix elements for important decay modes;
- the accurate simulation of QED radiation in the particle decays using the Yennie-Frautschi-Suura (YFS) formalism.

The information in the Particle Data Group's (PDG) compilation [77] of experimental data is sufficient in many cases to determine the properties of the hadrons

used in Herwig++. However, there are some particles for which the data are incomplete or too inaccurate to be used. Equally, there are a number of particles that are necessary for the simulation but have not been observed, particularly excited bottom and charm hadrons. A number of choices therefore have to be made in constructing the particle data tables used in the event generator based on the data in Ref. [77].

In the past the data were stored as either a text file or the contents of a FORTRAN COMMON block. However, due to the relatively large amount of data that needs to be stored a database approach based on the MySQL database system has been adopted. The event generation still uses text files to read in the particle properties but these files are now automatically generated from the database. This provides a range of benefits: the data can now be edited using a web interface; additional information describing how the particle properties were determined is stored in the database both improving the long-term maintenance and allowing the user to understand the uncertainties and assumptions involved.

3.6.1 Details

τ decays

The simulation of τ lepton decays in Herwig++ is described in detail in Ref. [75], together with a detailed comparison between the results of Herwig++ and TAUOLA [78, 79]. The matrix element for the decay of the τ lepton can be written as

$$\mathcal{M} = \frac{G_F}{\sqrt{2}} L_\mu J^\mu, \qquad L_\mu = \bar{u}(p_{\nu_\tau}) \gamma_\mu (1 - \gamma_5) u(p_\tau) , \tag{3.20}$$

where p_τ is the momentum of the τ and p_{ν_τ} is the momentum of the neutrino produced in the decay. The information on the decay products of the virtual W boson is contained in the hadronic current, J^μ. This factorisation allows for the implementation of the leptonic current L_μ for the decaying τ independent of the hadronic current and then combine them to calculate the τ decay matrix element. Hadronic currents that occur are for the τ decays to one pseudoscalar- or vector-meson, the leptonic decay to lepton and anti-neutrino, decays to two mesons via ρ or K^* resonances, to $K\pi$ via vector and scalar resonances, 3 meson decays, $\pi^\pm\pi^0\gamma$

and the four and five pion decays.

Weak hadron decays

There are five classes of weak mesonic decays currently included in the simulation:

1. **Exclusive semi-leptonic decays of bottom and charm mesons**
   The decays are of the general type $X \to Y\ell\nu_\ell$. Their matrix element can again be factorised into a leptonic and a hadronic current. The latter one can be written in a general Lorentz structure with a number of unknown form factors. Several form factor models are available.

2. **Exclusive decays**
   Several models for $D \to K\pi\pi$ are included here, which are based on various experimental fits. Apart from that, other weak hadronic decays are simulated using the form factors that were already implemented for semi-leptonic meson decays together with the weak currents from τ decays.

3. **Inclusive decays**
   In addition to the exclusive weak decays of the mesons to specific final-states we include a number of models of the decay of mesons containing a heavy, *i.e.* bottom or charm, quark based on the partonic decay of the heavy quark. The Herwig++ cluster hadronisation model is then applied to the resulting partonic final state to produce hadrons. This approach is primarily used for the bottom mesons where there are insufficient exclusive modes to saturate the branching ratios.

4. **Leptonic decay of pseudoscalar mesons**
   There are a small number of decays of pseudoscalar mesons to a charged lepton and a neutrino, *e.g.* $\pi \to \ell\nu$ and $D_s \to \ell\nu$.

5. **Inclusive $b \to s\gamma$ mediated decays**
   There is a range of decays, both inclusive and exclusive, mediated by the $b \to s\gamma$ transition. These decays are simulated by using a partonic decay of the B meson to a photon and a hadronic system, composed of a quark and antiquark, which recoils against the photon. The mass spectrum of the hadronic system is calculated using a theoretical model [80].

Strong and electromagnetic hadron decays

The vast majority of the strong and electromagnetic decays in Herwig++ are simulated using a few simple models based on the spin structure of the decay. These simple models are supplemented with a small number of specialised models, usually from experimental fits, for specific decay modes.

For a number of bottomonium and charmonium resonances partonic decays of the mesons to $q\bar{q}$, gg, ggg and $gg\gamma$ are used to model the unobserved inclusive modes needed to saturate the branching ratios. The cluster hadronisation model is then used to hadronise these partonic final-states. A veto prevents double counting with other exclusive modes.

Chapter 4

Multiple Partonic Interactions

"Prediction is very difficult, especially if it's about the future."
— Niels Bohr, 1885 - 1962

After an introduction and discussion of experimental findings related to the underlying event, we will introduce the model that we use to simulate it in terms of multiple interactions. After tuning its free parameters to existing data, we address the question of intrinsic PDF uncertainties and make predictions for the LHC. Needless to say, these studies rely on a Monte Carlo implementation of the presented ideas into Herwig++, which is a central building block of this work. We will, however, focus on the physics and describe the implementation only briefly in Appendix A.

4.1 Introduction

With the advent of the LHC in the near future it will become increasingly important to gain a detailed understanding of all sources of hadronic activity in a high energy scattering event. An important source of additional soft and semi-hard jets will be the presence of the underlying event. From the experimental point of view, the underlying event contains all activity in a hadronic collision that is not related to the signal particles from the hard process, e.g. leptons or missing trans-

verse energy. The additional particles may result from the initial-state radiation of additional gluons or from additional hard (or soft) scatters that occur during the same hadron–hadron collision. Jet measurements are particularly sensitive to the underlying event because, although a jet's energy is dominated by the primary hard parton that initiated it, jet algorithms inevitably gather together all other energy deposits in its vicinity, giving an important correction to its energy and internal structure.

In standard Monte Carlo event generators, like Herwig(++) [32–36, 47] , PYTHIA [38, 39] or SHERPA [40], additional gluons from initial- and final-state radiation are generated with the help of parton shower algorithms, possibly supplemented by multi-jet matrix elements[81, 82]. Therefore, we tend to attribute these to the hard process rather than to the underlying event. On top of that, the underlying event is simulated as some additional hadronic activity. The simplest way to do so is the so–called UA5 model [83], which has been the default underlying event model in HERWIG for a long time. Here, additional (soft) hadronic activity is generated as a number of additional clusters are generated flat in rapidity with an exponential transverse momentum distribution. See [35] for more details. These clusters eventually give the required additional activity of soft hadrons.

Another variant, which has been far more successful in the description of recent collider data, was formulated as a sequence of more-or-less independent parton interactions. The simplest case of two partonic interactions is shown in Fig. 4.1 In contrast to the UA5 model this model is capable of describing the jet-like structure of the underlying event. In its initial formulation [84] there were no parton showers invoked. Later variants of this model also contain full parton showers [85, 86]. The additional scatters in these models are always modelled as simple QCD $2 \to 2$ scattering as long as the scattering contains a hard jet of at least a few GeV. Soft, more forward scattering may also be

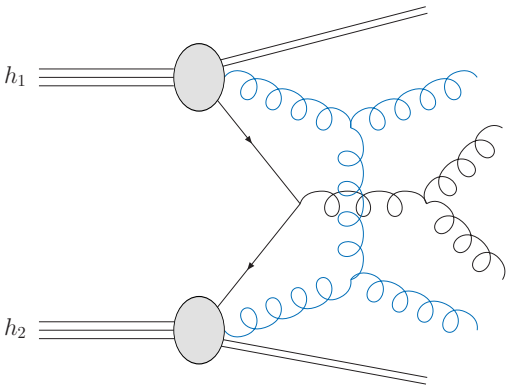

Figure 4.1: Sketch of two partonic scatterings.

modelled but requires a unified description of perturbative and non-perturbative scattering, as in the dual parton model [87–89], which had been implemented into the event generator PHOJET [41]. Another model is the simple extrapolation of the transverse momentum distribution of hard jets in QCD processes down to zero p_t [90]. Such a modelling of soft interactions will also allow us to describe minimum bias events. These are dominated by soft, forward scatterings and diffractive production of particles during the hadron–hadron scattering event.

Understanding minimum bias interactions and the underlying event are very important for many aspects of LHC physics. Particularly in high luminosity runs, every triggered hard event in one bunch crossing will be accompanied by additional interactions among other protons from the same bunch. These are predominantly minimum bias interactions and will give some additional activity in the detectors. There are already detailed plans for the measurement of the underlying event in ATLAS [91] and CMS [92, 93]. The presence of the underlying event is important whenever measurements at the LHC will be based on the measurements of the properties of jets, like e.g. their energy. The determination of the so-called jet energy scale is known to be improved when a reasonable modelling of the underlying event is included in the analysis. A good example for this is the measurement of the top mass [94]. Implications for the central jet veto in vector boson fusion processes have been addressed in detail in [95].

In this Chapter we will focus on the description of the semi-hard component of the underlying event, which stems from additional semi-hard scatters within the same proton. Not only does this model give us a simple unitarisation of the hard cross section, it also allows to give a good description of the additional substructure of the underlying events. It turns out that most activity in the underlying event can be understood in terms of hard mini-jets. We therefore adopt this model, based on the model JIMMY [85, 86], for our new event generator Herwig++ [35]. We will describe the basic implementation of the model and its parameters and study some important implications for jet final-states. In Chap. 6 we will consider an extension of this model towards softer interactions, which will also allow us to describe minimum bias interactions.

Improvements of the underlying event description have also been implemented in other event generators. A completely new formulation of the interleaving of un-

derlying hard scatterings with the parton shower has been introduced with the latest versions of PYTHIA [38, 39, 96, 97]. A model very similar to the multiple interaction model in PYTHIA has been implemented in SHERPA [98]. A new approach, based on k_T–factorisation [99–101] has been introduced and studied in [102]. An important issue, which has been addressed in [96] is the relation between the charged particle multiplicity and the average transverse momentum in the underlying event. The relation between these observables in the transverse region of jet events may point us towards the right colour correlations of the different hard scatters [103]. We want to point out that the organisation of colour lines adopted in our model differs significantly from that in PYTHIA.

In Sect. 4.3 we briefly review the theoretical motivation for multiple interactions and describe all details that are relevant for our Monte Carlo implementation. In Sect. 4.4 we discuss the parameters of our model and perform a fit to current Tevatron data. Taking this as a starting point, we make predictions for the most important final-state observables at the LHC. Furthermore, we discuss implications of the intrinsic uncertainties of parton distribution functions for the underlying event observables.

4.2 Experimental results

Experimentally, there has been strong evidence for the presence of multiple partonic interactions already at the CERN ISR through the measurement of a momentum imbalance in multi-jet events [104]. The idea for this measurement is that multiple pairs of jets, two in this case, will appear to be balanced in transverse momentum if they have been created in different back–to–back events rather than a single multi-jet event. Similar observations of double parton scattering [105] have been made at the Tevatron [106, 107]. Nowadays, the clearest observation has been made in γ+3 jet events at CDF [108]. In addition to this clear evidence for the presence of multiple interactions in hadronic collisions, the only sensible description of the final-state of such events can be made with detailed Monte Carlo modelling, based on this ansatz. The most detailed measurements of the properties of the underlying event as well as their implications for Monte Carlo models are described in [109, 110].

4.2.1 CDF analyses

We will use the data of Ref. [109] to validate and tune our model and therefore give a detailed description of the measurement in this section.

CDF has studied the properties of the charged particle component of jets, which they refer to as *charged particle jet*. They used a simple algorithm to reconstruct the jets and examine event properties as a function of the transverse momentum of the so-called *leading jet*. This is the jet with the largest transverse momentum in the event. The jet p_t is defined to be the scalar sum of the transverse momentum of all constituents, *i.e.* charged particles, that build up the jet.

The analysis solely used information from the central tracking chamber (CTC) in the region $p_t > 0.5$ GeV and $|\eta| < 1$ where the track finding efficiency is high and uniform. The data is then compared to the simulation by applying this constant efficiency (92%) to the simulated data, without any further detector simulation.

The direction of the *leading jet* was used to partition each event into three parts, the **towards, away** and **transverse** regions. These regions are equal in size in $\eta - \phi$ space and classify where particles are located in this space with respect to the hardest jet in the event. Figure 4.2 shows the three regions schematically for an example event. The towards region contains the leading charged particle jet, whereas the away region contains, on average, the balancing jet. The transverse region, being perpendicular to the plane of the hard $2 \to 2$ scattering, exhibits the largest relative contribution from the underlying event. If we assume a symmetric underlying event in azimuth, this region is therefore very sensitive to the underlying event. For each of these regions the average number of charged particles and the average scalar p_t sum is plotted against the p_t of the leading jet.

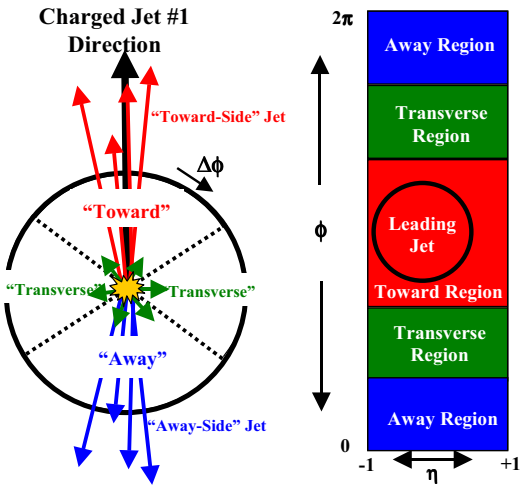

Figure 4.2: Event topology. Taken from Ref. [109].

Two data sets were used in the analysis, where in addition to the p_t and η cuts on the tracks a single vertex requirement was imposed to eliminate the background from several proton anti-proton collisions in one bunch crossing (Pile-up).

1. The first dataset was obtained by applying the *Min-bias trigger*, which required at least one particle hit in the forward beam-beam counter (BBC) as well as in the backward BBC ($3.4 < |\eta| < 5.2$). The data collected here goes up to 20 GeV leading jet transverse momentum.

2. The *Jet20* trigger was used for the second dataset to extend the analysis to larger values of leading jet transverse momentum. It required an energy deposit of at least 20 GeV in a cluster of calorimeter cells. Hence, this trigger acts on both charged and neutral particles. Nevertheless its data samples are used from 20 GeV transverse momentum of the leading charged particle jet onwards. This matching should have a residual bias, which forced us to add an additional systematic error for this transition region. Details on this additional error are given in Appendix B.

Jet definition

The jet algorithm that was used is non-standard and works as follows:

1. Order all particles according to their transverse momentum ($\rightarrow$ ordered list).

2. Go to the first particle in the list and assign a new jet to it. Remove this particle from the list. If the list is empty: `exit`

3. Go to the first particle in the list

4. Compute the distance measure R with respect to the centroid of the jet.

5. $R \leq 0.7$:

   (a) Add this particle to the jet.

   (b) Remove it from the list. If the list is empty: `exit`

(c) Recalculate the centroid of the jet, with

$$\eta_{\text{jet}} = \sum_i \frac{p_{t,i}\,\eta_i}{p_{t,\text{jet}}}, \quad \phi_{\text{jet}} = \Delta_\phi \left(\phi_1 + \sum_i \frac{p_{t,i}}{p_{t,\text{jet}}} \Delta_\phi(\phi_i - \phi_1) \right), \qquad (4.1)$$

where ϕ_1 is the azimuthal angle of any particle in the jet and Δ_ϕ a mapping to the range $[-\pi, \pi]$.

(d) `Go to 3.`

$R > 0.7$:

(a) If the end of the list is already reached, `Go to 2.` otherwise go to the next particle in the list.

(b) `Go to 4.`

Once a particle is assigned to a jet it stays with that jet. This ensures that all particles are assigned to a jet, but it means that some particles in the jet may lie outside of R. There is no merging or splitting and a particle is in one and only one jet. This jet algorithm is not IRC safe and therefore not applicable at the parton level. Full event generation provides a regularisation of the infrared and collinear divergences via the hadronic masses but a residual sensitivity to soft physics may still exist.

4.3 The model

The starting point for thinking about multiple interactions is the observation that the cross section for QCD jet production may exceed the total pp or $p\bar{p}$ cross section already at an intermediate energy range and eventually seems to violate unitarity. For example, for QCD jet production with a minimum p_t of 2 GeV this already happens at $\sqrt{s} \sim 1$ TeV. This can be seen in Fig. 4.3, where we plot the QCD jet cross section as well as the total pp cross section parameterisation from the non-perturbative Pomeron fits from Refs.[6, 7].

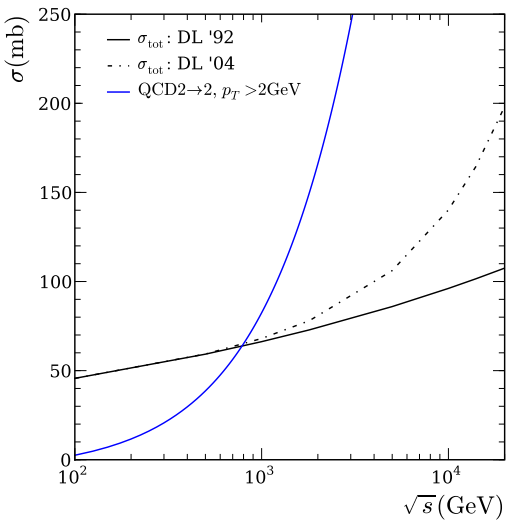

Figure 4.3: Total cross sections (black) in two parameterisation [6, 7] based on the non-perturbative Pomeron fits by Donnachie and Landshoff. In blue the QCD jet production cross section above 2 GeV.

This p_t cutoff should however be large enough to ensure that we can calculate the cross section in pQCD, using Eq. (2.50),

$$\sigma^{\rm inc}(s; p_t^{\rm min}) = \sum_{i,j} \int_{p_t^{\rm min 2}} {\rm d}p_t^2 \; f_{i/h_1}(x_1, \mu^2) \otimes \frac{{\rm d}\hat{\sigma}_{i,j}}{{\rm d}p_t^2} \otimes f_{j/h_2}(x_2, \mu^2) \,, \tag{4.2}$$

where $\otimes$ denote the convolution integrals in longitudinal momentum fractions x_1 and x_2. ${\rm d}\hat{\sigma}$ is the differential partonic cross section for QCD 2→2 scattering. The rapid increase of this cross section remains for any fixed cut-off and the reason for it turns out to be the strong rise of the proton structure function at small x, since the x values probed decrease with increasing centre-of-mass energy.

The key to resolve this seeming unitarity violation is the *inclusive* definition of the standard parton distribution functions. They give the *inclusive* distribution of a parton in a hadron, with all other partonic interactions summed and integrated out. If, on average, there are $\langle n_{\rm dijet} \rangle$ jet pairs produced with transverse momentum

larger than $p_t^{\min}$ per collision, one has

$$\sigma^{\text{inc}}(s; p_t^{\min}) = \langle n_{\text{dijet}} \rangle \cdot \sigma_{\text{inel}}(s; p_t^{\min}) \,, \tag{4.3}$$

where σ_{inel} is the cross section for having one or more jet pairs above $p_t^{\min}$. σ_{inel} has to stay below the total cross sections to preserve unitarity. This proliferation of low-x partons does, however, signal the onset of a regime in which the simple interpretation of the pQCD calculation as describing the only partonic scattering must be unitarised by additional scatters.

In principle, predicting the rate of multiple partonic scattering processes requires multi-parton distribution functions, about which we have almost no experimental information. However, the fact that the standard parton distribution functions describe the inclusive distribution gives a powerful constraint, which we can use to construct a simple model.

4.3.1 Parton level theory

The procedure of calculating the inelastic cross section from the inclusive one employs the eikonal approximation, introduced in Chap. 2. At fixed impact parameter, $b \equiv |\mathbf{b}|$, the probability for k partonic interactions,

$$\mathcal{P}_k = \frac{\langle n(b,s) \rangle^k}{k!} \, e^{-\langle n(b,s) \rangle} \,, \tag{4.4}$$

can be derived [111] in a field-theoretical approach using the Abramovski-Gribov-Kancheli (AGK) cutting rules [112]. The average number of partonic collisions, $\langle n(b,s) \rangle$, can be obtained as convolution of a parton luminosity, $\mathcal{L}_{\text{partons}}$, and the partonic cross section as

$$\langle n(b,s) \rangle = \mathcal{L}_{\text{partons}}(x_1, x_2, b) \otimes \sum_{i,j} \int \mathrm{d}p_t^2 \, \frac{\mathrm{d}\hat{\sigma}_{i,j}}{\mathrm{d}p_t^2} \,. \tag{4.5}$$

Since $\mathcal{L}_{\text{partons}}$ most likely depends on the longitudinal momentum fractions as well as the transverse coordinates, it is expressed in terms of the number densities $G(x, \mathbf{b}, \mu^2)$. They represent the average number of partons with a given momentum

fraction x and transverse coordinate $\mathbf{b}$. Equation (4.5) reads now

$$\begin{aligned}\langle n(b,s)\rangle &= \int \mathrm{d}^2\mathbf{b}_1\mathrm{d}^2\mathbf{b}_2\mathrm{d}p_t^2 \sum_{i,j}\frac{\mathrm{d}\hat{\sigma}_{ij}}{\mathrm{d}p_t^2} \\ &\quad \otimes G_{i/h_1}(x_1,|\mathbf{b}_1|,\mu^2)\otimes G_{j/h_2}(x_2,|\mathbf{b}_2|,\mu^2)\delta^2(\mathbf{b}_2-\mathbf{b}_1-\mathbf{b}) \qquad (4.6)\\ &= \int \mathrm{d}^2\mathbf{b}'\mathrm{d}p_t^2 \sum_{i,j}\frac{\mathrm{d}\hat{\sigma}_{ij}}{\mathrm{d}p_t^2} \\ &\quad \otimes G_{i/h_1}(x_1,|\mathbf{b}-\mathbf{b}'|,\mu^2)\otimes G_{j/h_2}(x_2,|\mathbf{b}'|,\mu^2)\,, \qquad (4.7)\end{aligned}$$

By assuming a factorisation of the x and $\mathbf{b}$ dependence in G, namely

$$G(x,\mathbf{b},\mu^2) = f(x,\mu^2)\cdot S(\mathbf{b})\,, \qquad (4.8)$$

where $f(x,\mu^2)$ is the conventional parton distribution and $S(\mathbf{b})$ are the spatial parton distributions, Eq. (4.7) can be written as

$$\begin{aligned}\langle n(b,s)\rangle &= \sigma^{\mathrm{inc}}(s;p_t^{\mathrm{min}})\cdot\int \mathrm{d}^2\mathbf{b}'\; S_{h_1}(|\mathbf{b}-\mathbf{b}'|)\; S_{h_2}(|\mathbf{b}'|) \\ &= A(b)\cdot\sigma^{\mathrm{inc}}(s;p_t^{\mathrm{min}})\,, \qquad (4.9)\end{aligned}$$

where we identify the standard perturbative jet cross section from Eq. (4.2) . In Eq. (4.9), $A(b)$ describes the overlap of the partons in the colliding hadrons. We model the impact parameter dependence of partons in a hadron, $S(\mathbf{b})$, by the electromagnetic form factor,

$$S_{\bar{p}}(\mathbf{b}) = S_p(\mathbf{b}) = \int \frac{\mathrm{d}^2\mathbf{k}}{(2\pi)^2}\;\frac{e^{i\mathbf{k}\cdot\mathbf{b}}}{(1+\mathbf{k}^2/\mu^2)^2}\,, \qquad (4.10)$$

where μ is the inverse hadron radius. This leads to

$$A(b) = \frac{\mu^2}{96\pi}(\mu b)^3 K_3(\mu b)\,, \qquad (4.11)$$

where $K_3(x)$ is the modified Bessel function of the third kind. The overlap function, shown in Fig. 6.2, is normalised such that

$$\int \mathrm{d}^2\mathbf{b}\; A(b) = 1\,. \qquad (4.12)$$

We do not fix μ at the value determined from elastic ep scattering, but rather treat it as a free parameter, because the spatial parton distribution is assumed to be similar to the distribution of charge, but not necessarily identical.

The cross section for having exactly n scatters with individual cross section σ^{inc}, using this Poissonian distribution is

$$\sigma_n(\sigma^{\text{inc}}) = \int \mathrm{d}^2\mathbf{b} \;\; \mathcal{P}_n(A(b)\cdot\sigma^{\text{inc}}) = \int \mathrm{d}^2\mathbf{b} \;\; \frac{(A(b)\cdot\sigma^{\text{inc}})^n}{n!}\, e^{-A(b)\cdot\sigma^{\text{inc}}} \;. \tag{4.13}$$

The probability of having n scatters in an event, given that there is at least one, is then

$$\mathrm{P}_{n\geq 1}(\sigma^{\text{inc}}) = \frac{\int \mathrm{d}^2\mathbf{b} \;\; \mathcal{P}_n(A(b)\cdot\sigma^{\text{inc}})}{\int \mathrm{d}^2\mathbf{b} \;\; \sum_{k=1}^{\infty} \mathcal{P}_k(A(b)\cdot\sigma^{\text{inc}})} = \frac{\sigma_n(\sigma^{\text{inc}})}{\sigma_{\text{inel}}(\sigma^{\text{inc}})}\,. \tag{4.14}$$

Equation (4.14) is used as the basis of the multi-parton scattering generator for events in which the hard process is identical to the one used in the underlying event, *i.e.* QCD $2 \to 2$ scattering. σ_{inel} in the denominator of Eq.(4.14) is the inelastic cross section, which takes multiple scatterings properly into account and thus ultimately solves the initial problem of unitarity violation. It is given by,

$$\sigma_{\text{inel}}(\sigma^{\text{inc}};\mu) = \int \mathrm{d}^2\mathbf{b} \;\; \sum_{n=1}^{\infty} \mathcal{P}_n = \int \mathrm{d}^2\mathbf{b} \;\; \left[1 - \; e^{-\langle n(b,s)\rangle}\right] \tag{4.15}$$

For distinct scattering types a modification is used, as described in the next section.

Different scattering types

Following the assumption of independent additional scatterings the cross section for two distinct scattering types a and b with the respective multiplicities k and m can be written as

$$\begin{aligned}\sigma_{k,m}(\sigma_a,\sigma_b) &= \int \mathrm{d}^2\mathbf{b} \;\; \mathcal{P}_k(A(b)\sigma_a)\;\mathcal{P}_m(A(b)\sigma_b) \\ &= \int \mathrm{d}^2\mathbf{b} \;\; \frac{(A(b)\sigma_a)^k}{k!}\, e^{-A(b)\sigma_a} \;\; \frac{(A(b)\sigma_b)^m}{m!}\, e^{-A(b)\sigma_b} \;.\end{aligned} \tag{4.16}$$

For small signal cross sections σ_b, the exponential can be approximated by unity. Using Eq. (4.16) the probability of having k events of type a in the presence of exactly one of type b is

$$\begin{aligned} \mathrm{P}_k &= \frac{\sigma_{k,1}}{\sum_{\ell=0}^{\infty}\sigma_{\ell,1}} \approx \frac{\int \mathrm{d}^2\mathbf{b}\;\; \mathcal{P}_k(A(b)\sigma_a)\cdot A(b)\sigma_b}{\int \mathrm{d}^2\mathbf{b}\;\; A(b)\sigma_b} \\ &= \int \mathrm{d}^2\mathbf{b}\;\; \mathcal{P}_k(A(b)\sigma_a)\cdot A(b)\,. \end{aligned}$$

This can then be rewritten to avoid the extra factor $A(b)$ in the form,

$$P_{n=k+1} \approx \frac{n}{\sigma_a}\int \mathrm{d}^2\mathbf{b}\;\; \mathcal{P}_n(A(b)\sigma_a)\,. \tag{4.17}$$

Here n is the total number of scatters, *i.e.* there is one of type b and $n-1$ of type a. It is worth noting that the fact that we have 'triggered on' a process with a small cross section leads to a bias in the b distribution and hence a higher multiplicity of additional scatters than in the pure QCD $2 \to 2$ scattering case.

Equation (4.17) can be used to describe underlying event activity under rare signal processes as well as jet production in the underlying event simulated under high p_t jet production as signal process. In the latter case the assumption of distinct scattering processes may not be fulfilled. One can show that in that case the mth scatter of type a that is also of type b should be rejected with probability $1/(m+1)$.

4.3.2 Monte Carlo implementation

The model introduced so far is entirely formulated at the parton level. However, an event generator aims for a full description of the event at the level of hadrons. This implies that the implementation of multi-parton scattering must be properly connected to the parton shower and hadronisation models, a few details of which we discuss in the following. We describe technical details of the implementation into Herwig++ in Appendix A.1, details of the way in which the multiple scattering is represented in the Herwig++ event record, and of how to access the model parameters, in Appendices A.2, A.3 and A.4 respectively.

Event generation starts with the sampling of the hard process according to its

matrix element and the parton densities. After that the parton shower evolves the final-state partons from the scale of the hard interaction down to a cut-off scale that is of the order of the confinement scale, but large enough to ensure that we remain within the perturbative regime. The incoming partons are evolved backwards to higher values of x and decreasing μ^2. The initial- and final-state parton showers in Herwig++ are performed using the coherent branching algorithm of Ref. [72], which is based on the original coherent shower algorithm of Refs. [43–45]. After the initial-state shower has terminated, the incoming partons are extracted out of the beam particles, a step that we describe in more detail below.

Now the number of secondary interactions is sampled from the probability distributions of Eq. (4.14) or Eq. (4.17) respectively. The chosen number of additional scatters is sampled according to the standard QCD $2 \to 2$ matrix elements and the same parton densities that were used for the hard process. That is, the additional hard processes are generated exactly according to the inclusive perturbative cross section, with no modification for the fact that they are additional scatterings. This list of processes is then successively processed by the parton shower. The partons involved in the additional hard scatters are also parton showered. As far as final-state showering is concerned, this is identical to a standard hard process. For the initial-state shower, we use the standard evolution algorithm, but with modified parton distribution functions, motivated by our model for extracting partons out of the hadron, which we return to shortly.

The backward evolution of an additional scattering may lead to partons with more energy than the remaining energy in the hadron remnants. This scattering has to be vetoed and is therefore regenerated until the desired multiplicity has been reached. If a requested scattering can never be generated without leading to violation of energy-momentum conservation, the program eventually gives up, reducing the multiplicity of scatters.

After the parton shower, the cluster model [44] is used in Herwig++ to model the hadronisation. The cluster model however necessarily expects (anti)quarks or (anti)diquarks at the beginning of the hadronisation. In the final-state this prerequisite is easily fulfilled by the gluon splitting mechanism: all final-state gluons decay non-perturbatively to light quark–antiquark pairs. In the case of an initial-state parton from an incoming hadron, this necessitates a parton extraction model,

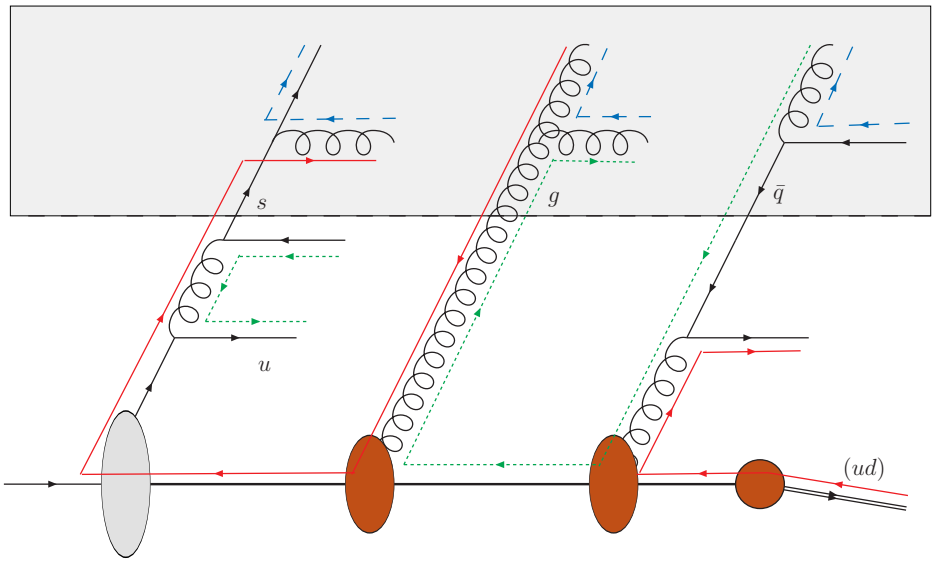

Figure 4.4: Schema of how the forced splittings and colour connections are implemented. Splittings in the shaded area stem from the hard scatters and the initial-state parton shower. The final splittings at the bottom are non-perturbative.

which we describe in the next section.

Finally all unstable particles must be decayed. Herwig++ uses a sophisticated model of hadronic decays as described in Refs. [75, 76].

Parton extraction

In the standard Herwig++ treatment of a single hard scattering, the prerequisite that the outgoing partons must be (anti)quarks or (anti)diquarks is implemented by forcing the backward evolution to terminate on a valence parton. This then gives a diquark as the proton remnant for example. This diquark is colour-connected through the colour connections of the valence quark either to a final-state parton emitted during the corresponding initial-state parton shower or through the hard process to a parton in one of the other jets in the event. In collisions other than pp, in events with little radiation, it can even be connected right through the event to the other hadron remnant.

It is often the case that by the time the perturbative evolution has terminated,

the backward evolution has reached a valence parton, since their PDFs dominate at high x and low scale. When this is not the case and the backward evolution has terminated on a gluon or sea quark, one or two additional backward steps respectively are 'forced', using the standard backward evolution algorithm, but with all flavours except the one necessary for the forced step, vetoed.

In the implementation of multiple interactions, we keep the treatment of the first interaction untouched, *i.e.* it is exactly as just described. This means that the valence structure of the hadron has already been saturated, with one valence parton extracted and the remainder forming the hadron remnant. This does not therefore provide a structure that can be iterated for subsequent scatters. Instead, we modify the backward evolution so that it terminates on a gluon. We do this both dynamically during the evolution and by a forced backward evolution step if necessary. During the backward evolution we use modified parton distribution functions that are identical to the standard ones but with the valence contributions subtracted out[1]. We stress that this subtraction of valence contributions is the only modification we make. In particular, the distribution of gluons is identical to that in the original hadron, leading to the possibility that the backward evolution of multiple scatters can over-saturate the available energy, which we deal with as already discussed above.

Once the backward evolution has terminated on a gluon, its colour connections can therefore be inserted into those of the previous remnant. As a concrete example, for the second scattering in an event with an incoming proton, the colour line of the gluon is connected to the diquark proton remnant and the anticolour line of the gluon is connected through the valence quark, to the outgoing parton that the diquark was previously connected to. This then gives a structure that can be iterated an arbitrary number of times. Since we do not order the additional hard scatters, for example in transverse momentum, this is equivalent to the colour connection model described as 'random' in [96]. The implementation of other colour connection models as described there would be possible, and may be interesting work for the future as well a models of colour re-connection [113].

[1] They do not therefore obey a momentum sum rule, but the algorithm is not sensitive to this fact, since it only involves ratios of PDFs. If one wanted to, one could rescale all the modified PDFs by a common factor to regain the momentum sum rule. The results would be unchanged.

We illustrate this parton extraction model in more detail in Fig. 4.3.2. In the upper part of the figure, which is shaded, we can see the extracted partons after a possible perturbative parton shower. In the lower half of the figure, additional forced splittings are carried out in order to guarantee a certain flavour structure of the remnant. The first extracted parton will always be a valence quark while all additional hard scatters will always end up on a gluon. The colour structure is as just described, with the gluon produced by each hard scatter inserted into the colour–anticolour connection left by the previous one.

The way in which the structure of the hadron remnant is represented in the event record is not quite the same as the way in which it is generated, as described above. The same event is shown in Fig. A.1 as it would appear in the event record, as described in Appendix A.2.

4.4 Results

We will now discuss several hadronic observables both for the Tevatron and the LHC. In particular a comparison to CDF data [109] is performed. For that reason, the non-standard jet algorithm used for the data analysis has been implemented. Detector effects are solely taken into account by simulating the 92% track efficiency by ignoring 8% of charged particles, chosen randomly[2]. For the LHC the prediction is compared to several other generators [98].

4.4.1 Tuning and Tevatron results

We have performed a tune of the model by calculating the total χ^2 against the data from Ref. [109]. See Sect. 4.2.1 for a detailed description. We used

$$\chi^2 = \sum_{\text{bins}} \frac{(X_{\text{Exp}} - X_{\text{MC}})^2}{\sigma_{\text{Exp}}^2 + \sigma_{\text{MC}}^2} \tag{4.18}$$

as definition of our χ^2 function, where X are the observed values and σ the corresponding errors. We compare our predictions to data for the average number

[2] This is exactly the same procedure that the original analysis employed.

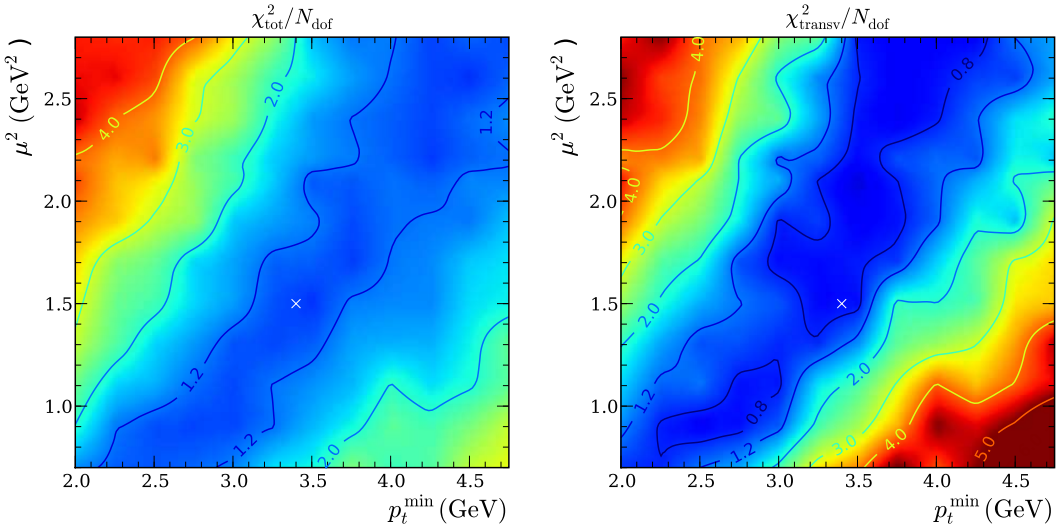

Figure 4.5: Contour plots for the χ^2 per degree of freedom of all discussed observables (left) and only the ones from the transverse region (right). The cross indicates the location of our preferred tune.

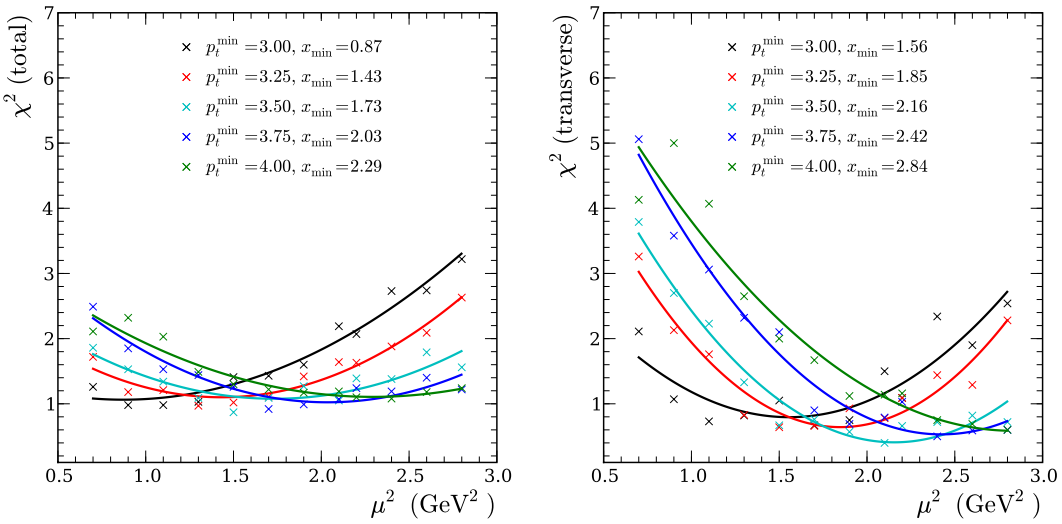

Figure 4.6: Line scans at fixed values of $p_t^{\rm min}$ of all discussed observables (left) and only the ones from the transverse region (right). The curves show a quadratic fit for each dataset. $x_{\rm min}$ is the position of the minimum calculated using the fit parameters.

of charged particles and for the scalar p_t sum in each of the three regions. As we are aiming primarily at a good description of the underlying event in high p_t events, we used jet production with a minimal transverse momentum of 15 GeV as the signal process. Because of that we only use data for the region of leading jet transverse momentum above 20 GeV corresponding to the jet data sample in the original analysis. We added an additional systematic error in quadrature for the lowest p_t bins as described in Appendix B.

The parameter space for this tune is two dimensional and consists of the p_t cut-off $p_t^{\min}$ and the inverse hadron radius squared, μ^2, entering $A(b)$ in Eq. (4.10). In Fig. 4.5 we show the contour plots for all six observables and for the observables from the transverse region respectively. We have used the MRST 2001 LO[114] PDFs built in to Herwig++ for this plot, and discuss the PDF-dependence in the next section. For these, and all subsequent plots, we use Herwig++, with all parameters at their default values except the two we are tuning and, in the next section, the PDF choice.

The description of the Tevatron data is truly satisfactory for the entire range of considered values of $p_t^{\min}$. For each point on the x-axis we can find a point on the y-axis to give a reasonable fit. Nevertheless an optimum can be found between 3 and 4 GeV. The strong and constant correlation between $p_t^{\min}$ and μ^2 is due to the fact that a smaller hadron radius will always balance against a larger p_t cut-off as far as the underlying event activity is concerned.

As a default tune we use $p_t^{\min} = 3.4$ GeV and $\mu^2 = 1.5$ GeV^2. Figure 4.7 shows the result of this parameter choice for the transverse region. The towards region is shown in Fig. 4.8 as well as the away region in Fig. 4.9. For these plots we used 10 million events in contrast to 1 million for each point in Fig. 4.5, which is the reason for the slight differences in the corresponding χ^2 values.

It is clear from these figures that event generation without any model for the underlying event is not capable of describing the data. In particular, in the transverse region, which receives the least contribution of the two jets from the matrix element, the results are a factor of two below the data.

Although our default multi-parton interaction (MPI) model gives a good overall description of the data, we see a slight trend to produce too much multiplicity in

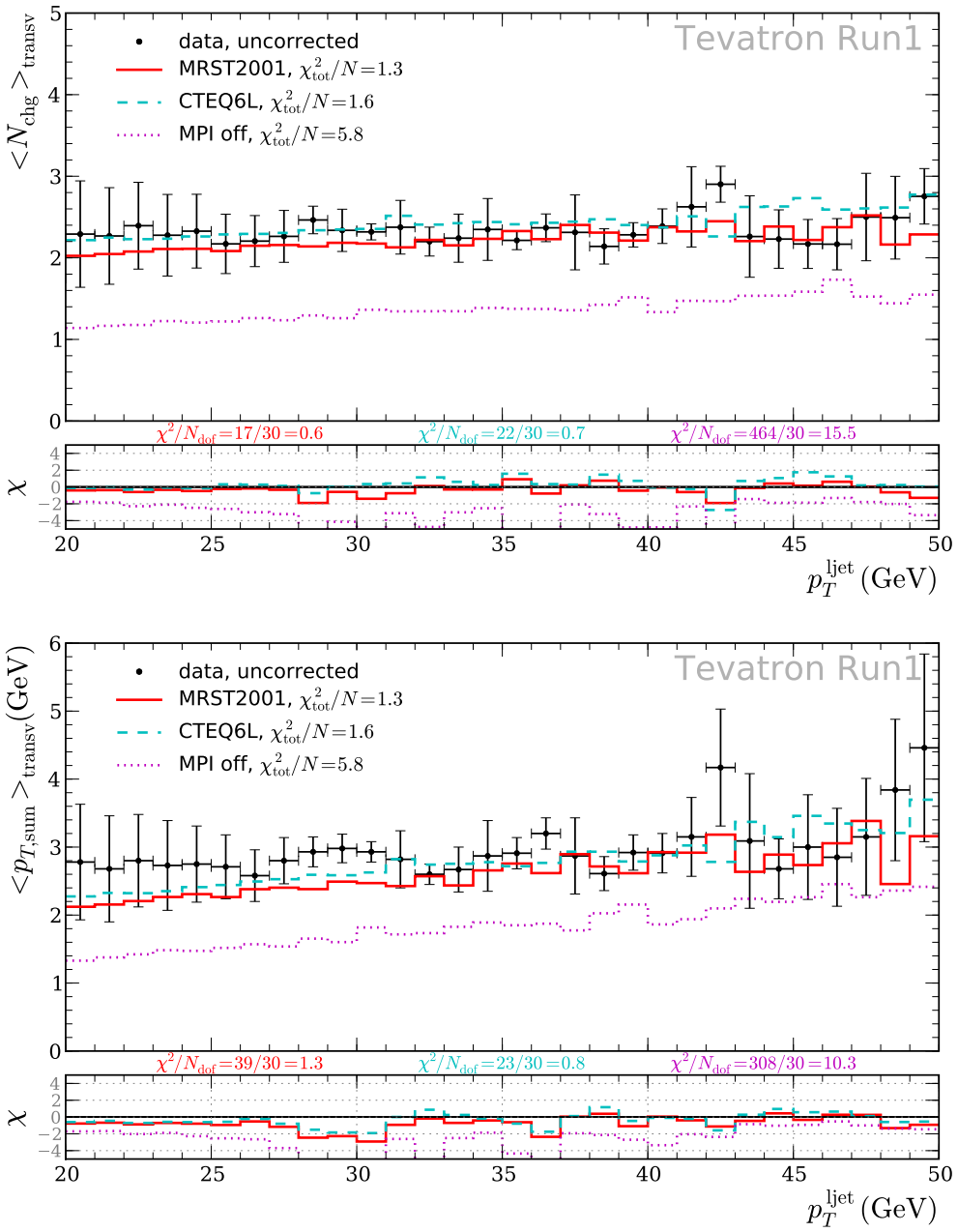

Figure 4.7: Multiplicity and $p_t^{\rm sum}$ in the **transverse** region. CDF data are shown as black circles. Herwig++ without MPI is drawn in green dots, Herwig++ with MPI using MRST [114] PDFs in solid red and with CTEQ6L [115] as blue dashed. The lower plot shows the statistical significance of the disagreement between Monte Carlo prediction and the data. The legend on the upper plot shows the total χ^2 for all observables, whereas the lower plot has the χ^2 values for this particular observable.

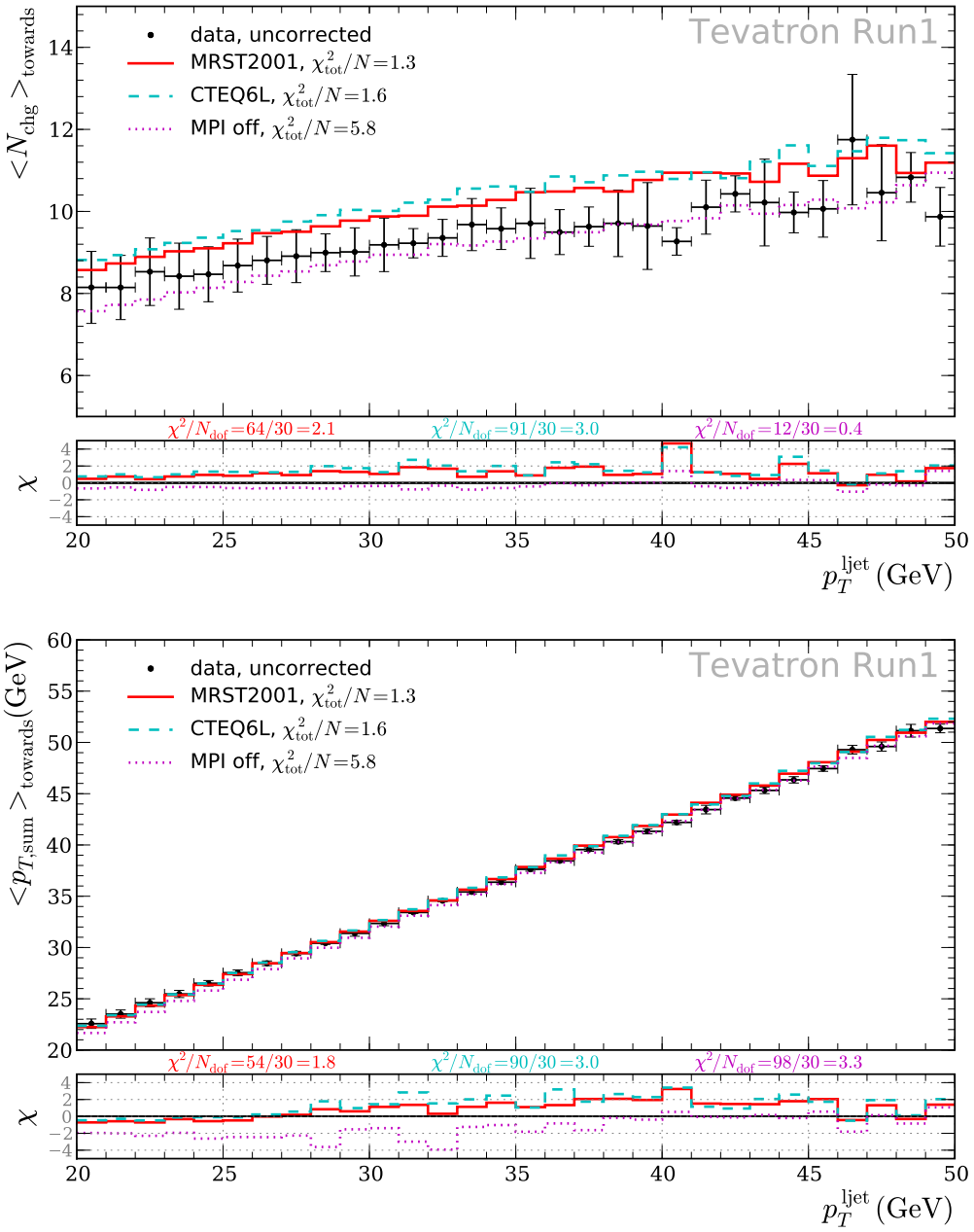

Figure 4.8: Multiplicity and $p_t^{\rm sum}$ in the **towards** region. CDF data are shown as black circles. Herwig++ without MPI is drawn in green dots, Herwig++ with MPI using MRST [114] PDFs in solid red and with CTEQ6L [115] as blue dashed. The lower plot shows the statistical significance of the disagreement between Monte Carlo prediction and the data. The legend on the upper plot shows the total χ^2 for all observables, whereas the lower plot has the χ^2 values for this particular observable.

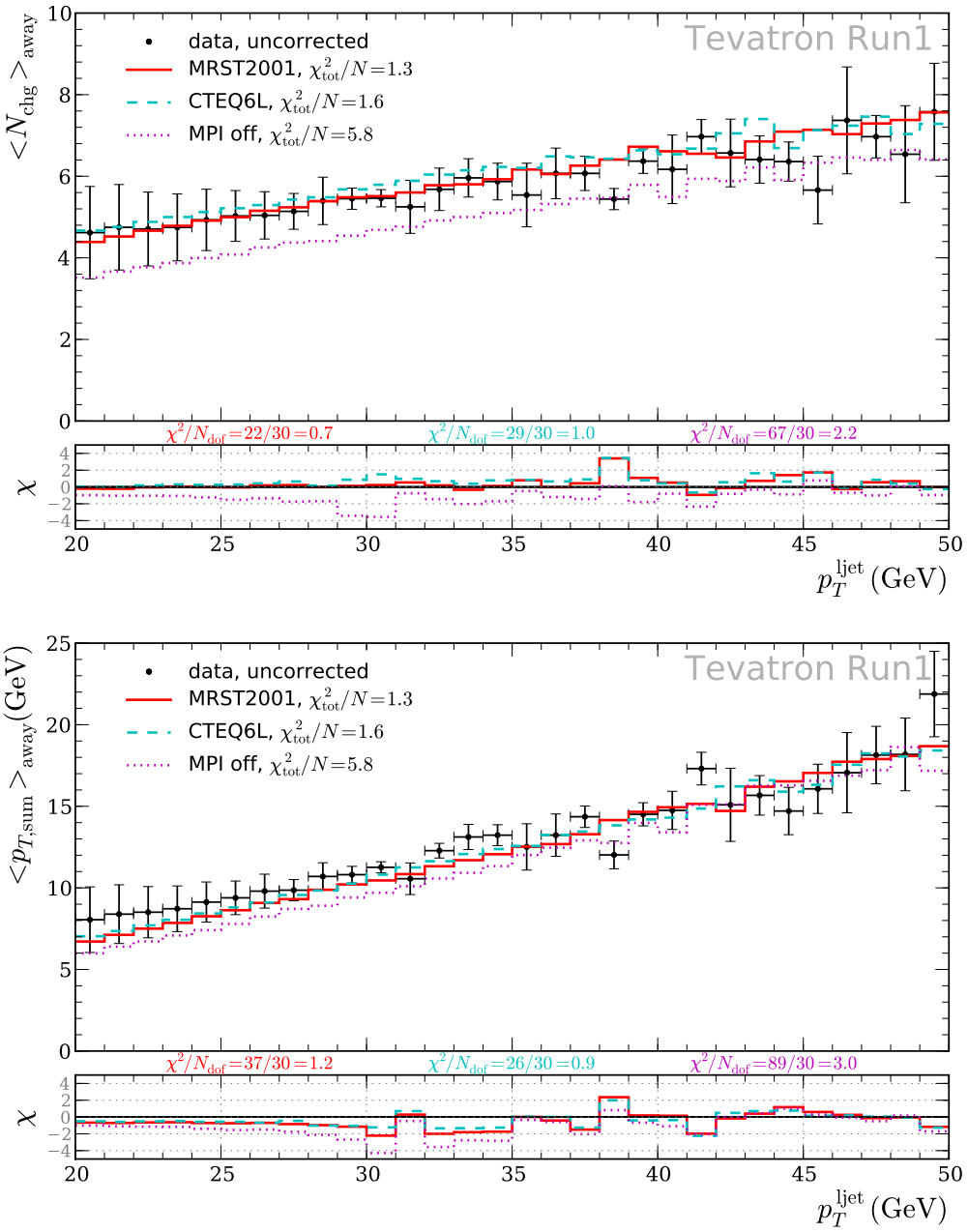

Figure 4.9: Multiplicity and $p_t^{\rm sum}$ in the **away** region. CDF data are shown as black circles. Herwig++ without MPI is drawn in green dots, Herwig++ with MPI using MRST [114] PDFs in solid red and with CTEQ6L [115] as blue dashed. The lower plot shows the statistical significance of the disagreement between Monte Carlo prediction and the data. The legend on the upper plot shows the total χ^2 for all observables, whereas the lower plot has the χ^2 values for this particular observable.

all the regions, most noticeably in the towards region, and too little p_t^{sum} in all the regions, most noticeably in the away region. This corresponds to having a slightly too soft spectrum of individual particles and has also been observed in attempts to fit the fortran Herwig+Jimmy model, the forerunner of ours, to the data of [109]. We note that in the towards region, which is dominated by the primary jet, Herwig++ without MPI is already close to the data, leaving very little room for MPI effects. Almost any model of the underlying event will produce more than enough multiplicity here and overshoot the data. The same is true to a lesser extent in the away region. In the process of χ^2 minimisation, there is therefore a slight pressure to suppress the underlying event effect, which results in the slight undershooting of the p_t^{sum} predictions. The same effect is true even more weakly in the transverse region, where one would say that the description is very good, but there is a slight trend to be above the data for N_{chg} and below it for p_t^{sum}. Since the effect is strongest for the regions dominated by the primary jets, we conclude that this is a general Herwig++ issue not specifically related to the MPI model. In any case, it is clear that it vastly improves the description of data relative to the no-MPI model.

We want to stress that the data from the experimental analysis are uncorrected. We already obtain a total χ^2 per degree of freedom very close to unity even with the over-simplified implementation of the reconstruction efficiency as used in the original analysis. A more precise examination would have to take detector effects into account in a more complete manner.

4.4.2 PDF uncertainties

For precision studies it is important to quantify the extent to which hard scattering cross sections are uncertain due to uncertainties in the PDFs. As we have already mentioned, jet cross sections are particularly sensitive to the amount of underlying event activity, which introduces an additional dependence on the PDF in our model. In particular, it relies on the partonic scattering cross sections down to small transverse momenta, which probe momentum fractions as small as $x \sim 10^{-7}$ at the LHC and $x \sim 10^{-6}$ at the Tevatron, where the PDFs are only indirectly constrained by data. One will have measured the amount of underlying event activity

at the LHC by the time precision measurements are being made, so one might think that the size of the underlying event correction will be known. However, in practice, jet cross section corrections depend significantly on rare fluctuations and correlations in the underlying event, so the correction must be represented by a model tuned to data, rather than by a single number measured from data. This will therefore entail in principle a retuning of the parameters of the underlying event model for each new PDF. This would make the quantification of PDF errors on a given jet cross section, or of extracting a new PDF set from jet data, much more complicated than a simple reweighting of the hard scattering cross section.

In this section we explore the extent to which this effect is important, by studying how the predictions with fixed parameters vary as one varies the PDF. We do this by comparing the central values of two different PDF sets (MRST and CTEQ) and also using the quantification of the uncertainties within one of them (CTEQ). Similar issues were also discussed in Ref. [116] for the uncertainty in parton shower corrections, which were found to be relatively small.

The results in Figs. 4.7–4.9 show the predictions of our model with MRST 2001[114] and CTEQ6L[115] PDFs with the parameters fixed to the values obtained from our fit with the MRST PDFs. We see that the difference in the amount of underlying event activity, quantified by the results in the transverse region between 30 and 40 GeV as an example, is some 10% higher with CTEQ6L than with MRST.

To quantify the effect of the uncertainties within a given PDF set, we have used the error sets provided with the CTEQ6 family, and the formula

$$\Delta X = \frac{1}{2}\left(\sum_{i=1}^{N_p}\left[X(S_i^+) - X(S_i^-)\right]^2\right)^{1/2}, \tag{4.19}$$

from Ref. [115]. Here X is the observable of interest and $X(S_i^\pm)$ are the predictions for X based on the PDF sets $S_i^\pm$ from the eigenvector basis. Doing this naïvely, we found that the statistical error on independent runs with each PDF set was greater than the variation between the sets. To try to overcome this obstacle, we have studied the relative PDF uncertainty, *i.e.* $\Delta X/X(S_0)$, as a function of the number of points used for each $X(S_i^\pm)$.

As an example, we show the result in Fig. 4.10 for one bin corresponding to $35-36$

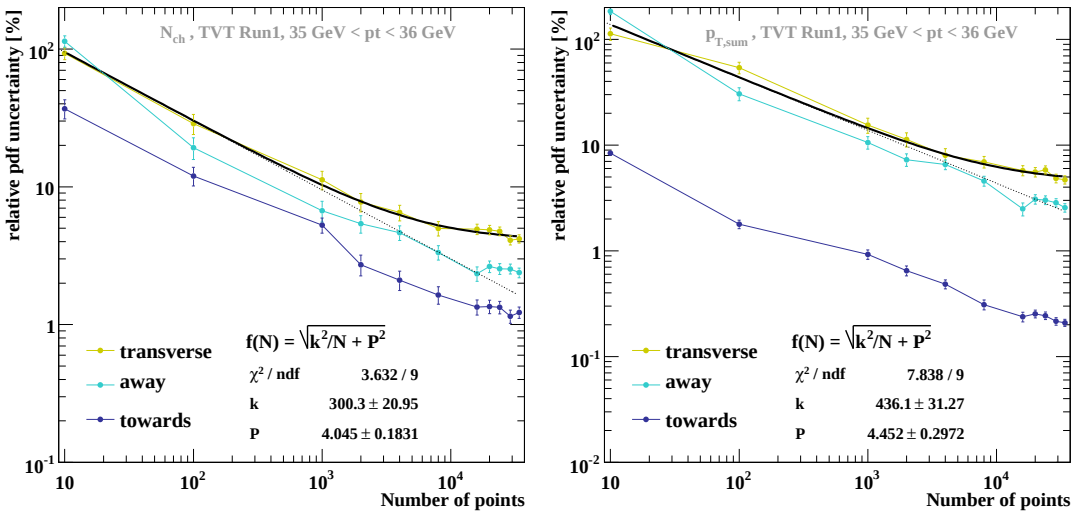

Figure 4.10: Relative PDF uncertainty, $\Delta X/X(S_0)$, in percent. Left for the multiplicity observables and right for the p_t^{sum} observables. The different curves show the results for the three different regions defined in the experimental analysis. The PDFs used are CTEQ6M [115] and its corresponding error sets. The fit result shown as a solid line is for the transverse region. Also shown as a light dashed line is the fit assuming a purely statistical error.

GeV of the leading jet. The final statistics are obtained from 20M fully generated events for each PDF set and the value on the x axis is the number of events falling within this bin. We see that with these 20M events, we have still not completely eliminated the statistical uncertainties. However, a departure from the straight line on a log–log plot that would be expected for pure statistical errors, $\sim 1/\sqrt{N}$, is clearly observed. We use this to extract the *true* PDF uncertainty, by fitting a curve of the form

$$f(N) = \sqrt{\frac{k^2}{N} + \mathrm{P}^2} \tag{4.20}$$

to these data. In performing the fit we get a reliable result already for a moderate number of events. From the fit results we can estimate the number of events that would be necessary to eliminate the contribution of the statistical uncertainty. Requiring it to be less than 10^{-1} of the total uncertainty leads to $N \sim 10^6$, which translates into $\sim 10^9$ fully generated events for each of the 40 PDF sets, which is

not feasible in practice. Instead, using our fit, we have a clear indication that the PDF uncertainty is around 4% for the multiplicity and 4.5% for the p_t^{sum} in the transverse region.

It is note-worthy that the difference between the two PDF sets is larger than the uncertainty on each. Although, as we have already mentioned, the underlying event will have already been measured before making precision measurements or using jet cross sections to extract PDFs, a model tuned to that underlying event measurement will have to be used and its tuning will depend on the PDF set. We consider an uncertainty of 5–10% large enough to warrant further study in this direction.

4.4.3 LHC expectation

We start the discussion of our predictions for the LHC with the plots in Fig. 4.11, which are related to the total multiplicity and mean multiplicity flow in jet events. We show Herwig++ with and without MPI. We used QCD jet production with a minimal p_t of 20 GeV as signal process. The MPI parameters were left at their default values, *i.e.* the fit to Tevatron CDF data.

The first plot in Fig. 4.11 shows the Koba-Nielsen-Olesen (KNO) distribution[117]. The MPI model satisfies KNO scaling fairly well, whereas Herwig++ without an underlying event clearly violates it.

The second plot in Fig. 4.11 shows the mean charged multiplicity as a function of pseudorapidity, η. The effect of MPI is clearly visible, growing significantly from the Tevatron to the LHC.

In Ref. [98] a comparison of different predictions for an analysis modelled on the CDF one discussed earlier was presented. As a benchmark observable the charged particle multiplicity for the transverse region was used. All expectations reached a plateau in this observable for $p_t^{ljet} > 10$ GeV. Our prediction for this observable is shown in Fig. 4.12, where it can be seen to have also reached a roughly constant plateau within the region shown. The height of this plateau can be used for comparison. In Ref. [98] PYTHIA 6.214 ATLAS tune reached a height of ~ 6.5, PYTHIA 6.214 CDF Tune A of ~ 5 and PHOJET 1.12 of ~ 3. Our model reaches

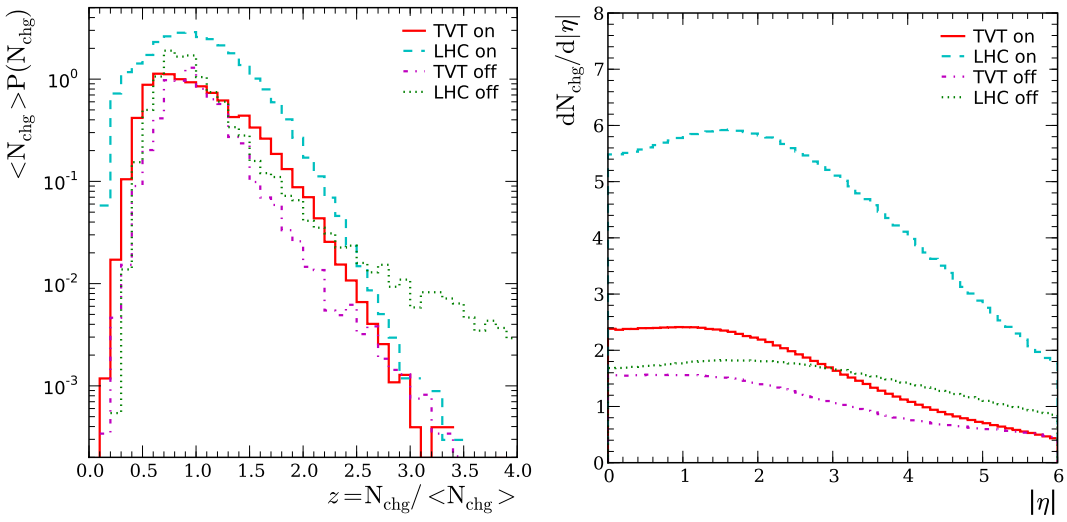

Figure 4.11: KNO plot (left) and differential multiplicity distribution (right) for Tevatron and LHC runs.

a height of ~ 5 and seems to be close to the PYTHIA 6.214 CDF tune, although our model parameters were kept constant at their values extracted from the fit to Tevatron data.

We have seen already in Sec. 4.4.1 that our fit results in a flat valley of parameter points, which all give a very good description of the data. We will briefly estimate the spread of our LHC expectations, using only parameter sets from this valley. The range of predictions that we deduce will be the range that can be expected assuming no energy dependence on our main parameters. Therefore early measurements could shed light on the potential energy dependence of the input parameters by simply comparing first data to these predictions. We extracted the average value of the two transverse observables shown in Fig. 4.12 for a given parameter set in the region 20 GeV $< p_t^{ljet} <$ 30 GeV. We did that for the best fit points at three different values for $p_t^{\min}$, namely 2 GeV, 3.4 GeV and 4.5 GeV. The resulting values are displayed in Table 4.1.

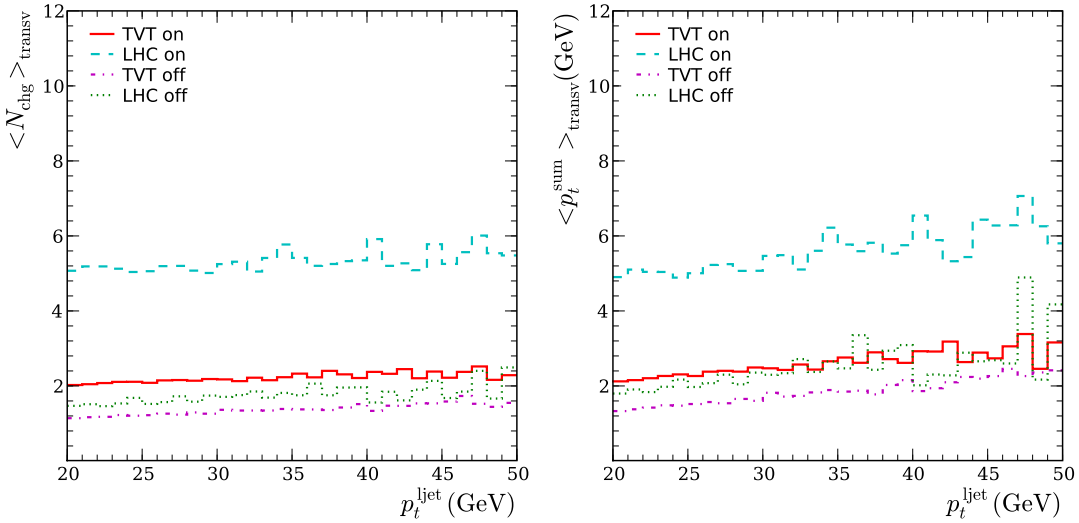

Figure 4.12: Multiplicity and $p_t^{\rm sum}$ in the transverse region for LHC runs with Herwig++. The different data sets are (from bottom to top): Tevatron with MPI off, LHC with MPI off, Tevatron with MPI on and LHC with MPI on.

LHC predictions	$\langle N_{\rm chg}\rangle^{\rm transv}$	$\langle p_t^{\rm sum}\rangle^{\rm transv}$(GeV)
TVT best fit	5.1 ± 0.3	5.0 ± 0.5

Table 4.1: LHC expectations for $\langle N_{\rm chg}\rangle$ and $\langle p_t^{\rm sum}\rangle$ in the transverse region. The uncertainties are obtained from varying $p_t^{\rm min}$ within the range we considered. For μ^2 we have taken the corresponding best fit values.

4.5 Conclusions

We have implemented a model of multiple semi-hard partonic interactions into the Herwig++ event generator. We have tuned its two free parameters to Tevatron data and found a good overall description. We have shown the extrapolation of its predictions to the LHC.

We consider the present work as only a first step towards our eventual goal of providing a complete description of the final-state of minimum bias collisions and underlying events in hard hadron–hadron collisions, validated on and tuned to all available data and extrapolated to the LHC with quantified uncertainties.

Among the various phenomenological and theoretical studies that will be needed to achieve this goal, the most prominent one is to consider the contribution from non-perturbative partonic scatterings below $p_t^{\min}$. We will pursue this path in Chap. 6 and Chap. 7, which will then allow us to describe minimum bias events, as well as the underlying event.

Chapter 5

Double Parton Scattering

We have already discussed, that current direct measurements of multiple partonic scatterings are limited to the case, where two of them happen in one hadronic collision. These special cases are called *double parton scattering* events. We will discuss their measurement as well as the simulation of these events in the context of our multiple scattering model, introduced in the previous chapter. We will show results for the case of like sign di-lepton production. In the double parton scattering case, these leptons stem from two like sign W's that are produced in two separate Drell Yan processes.

5.1 Introduction

The term *double parton scattering* events typically refers to two partonic scatterings in one hadronic collision, where both interactions occur at similar scales. These scales are typically larger than the ones in underlying event processes and at least one of the partonic interactions is not pure jet production. This characterisation is mainly due to the experimental needs to distinguish double parton scattering from the average underlying event and other QCD backgrounds. Several channels might be interesting, among them the production of several b quark pairs as discussed in Ref. [118], but also W production with an additional b quark pair [119], which can act as a background to $pp \to W + H(\to b\bar{b})$. In general, additional b production offers a copious source of double parton scattering events due to its

large cross section. Also like sign W production was discussed in Ref. [120]. The best measurement so far used the $\gamma j + jj$ double parton scattering channel [108].

Double parton scattering is not only of interest as background to certain signal processes. Many models [41, 84, 85, 90, 96, 97, 121] of underlying event physics, including ours, rely on multiple partonic interactions as their perturbative contribution. Measuring this contribution directly and not only via certain final-state measurements can provide valuable insights and constraints to existing models.

5.1.1 Effective cross section

We will now discuss the link between double parton scattering and our model with special emphasis on the so-called *effective cross section*. This quantity has been measured by CDF [108] and was defined as,

$$\sigma_{ab,2} = \frac{\sigma_a \, \sigma_b}{\sigma_{\text{CDF,eff}}} \,, \tag{5.1}$$

where $\sigma_{ab;2}$ is the cross section for a colliding proton anti-proton pair to have *exactly* two scatters, one of type a and one of type b, assumed to be of different types, *i.e.* distinguishable, and $\sigma_{a,b}$ are their *inclusive* cross sections. We denoted the scale factor above with $\sigma_{\text{CDF,eff}}$ as this definition has some deficiencies which can be eliminated by the more convenient definition,

$$\sigma_{ab;\text{incl}} = \frac{\sigma_a \, \sigma_b}{\sigma_{\text{eff}}} \,, \tag{5.2}$$

where $\sigma_{ab;\text{incl}}$ is the *inclusive* double-scattering cross section. As we will see, σ_{eff} is related to the distribution of partons in the transverse plane and can serve as a constraint to our model.

We will calculate the double parton scattering cross sections within our model and see explicitly why Eq. (5.2) is the more appropriate definition. To derive Eq. (5.1) we start with the expression for the exclusive n scattering cross section from Eq. (4.13),

$$\sigma_n(\sigma^{\text{inc}}) = \int \mathrm{d}^2\mathbf{b} \;\; \mathcal{P}_n(A(b) \cdot \sigma^{\text{inc}}) = \int \mathrm{d}^2\mathbf{b} \;\; \frac{(A(b) \cdot \sigma^{\text{inc}})^n}{n!} \, e^{-A(b)\cdot\sigma^{\text{inc}}} \,.$$

The cross section is obtained by integrating over all values of impact parameter the probability of the scatters: each has a probability $\sigma^{\text{inc}} A(b)$; there are n independent of them giving the power of n; and they are all of the same type, giving the $n!$ factor. Finally, the exponential gives the probability that there are no other scatters (of type b). It's generalisation to the case of two distinct scattering types leads to Eq. (4.16),

$$\sigma_{k,m}(\sigma_a, \sigma_b) = \int \mathrm{d}^2\mathbf{b}\ \frac{(A(b)\sigma_a)^k}{k!}\, e^{-A(b)\sigma_a}\ \ \frac{(A(b)\sigma_b)^m}{m!}\, e^{-A(b)\sigma_b}\ .$$

Eq. (5.1) corresponds to $\sigma_{1,1}(\sigma_a, \sigma_b)$. Assuming that at least one cross section (σ_a) is small enough to approximate the exponential with unity leads to

$$\sigma_{ab;2} = \sigma_a \sigma_b \int \mathrm{d}^2\mathbf{b}\ A^2(b)\, e^{-A(b)\sigma_b}\ , \tag{5.3}$$

where the integral corresponds to $(\sigma_{\text{CDF,eff}})^{-1}$. The problem is that this definition is not process independent. We see that for individual cross sections σ_a, σ_b that are large enough, the effective cross section receives a contribution from the exponential.

However, by simply using the *inclusive* instead of the *exclusive* double parton scattering cross section this problem can be avoided. Equation (4.13) gives the cross section for having exactly n scatters by integrating over the probability for having exactly n scatters. One obtains the inclusive probability by removing the exponential, which took into account that no other scattering happened. Hence,

$$\sigma_n^{\text{incl}}(\sigma_a) = \int \mathrm{d}^2\mathbf{b}\ \frac{(A(b)\sigma_a)^n}{n!} \tag{5.4}$$

is the cross section for having n or more interactions. The generalisation to two distinct scatters leads to

$$\begin{aligned} \sigma_{ab;\text{incl}} &= \sigma_a \sigma_b \int \mathrm{d}^2\mathbf{b}\ A^2(b) \\ &= \frac{\sigma_a \sigma_b}{\sigma_{\text{eff}}}\,, \end{aligned} \tag{5.5}$$

as expression for the double parton scattering cross section. σ_{eff} is now completely process independent and its measurement gives a direct handle on the partonic

overlap function $A(b)$ in impact parameter space.

It's clear that Eqs. (5.1) and (5.2) will give the same effective cross section in the limit $\sigma_a, \sigma_b \to 0$. The CDF measurement however used the exclusive definition and obtained a value of

$$\sigma_{\text{CDF,eff}} = (14.5 \pm 1.7^{+1.7}_{-2.3})\ \text{mb}\,. \tag{5.6}$$

It is possible to correct [122, 123] this measurement for the theoretically more useful definition of σ_{eff}, which then leads to

$$\sigma_{\text{eff}} = (11.5 \pm 1.3^{+1.3}_{-1.5})\ \text{mb}\,. \tag{5.7}$$

To calculate the inclusive double parton scattering cross section, given the inclusive cross sections of the individual scatterings of type a and b, we therefore use

$$\sigma_{ab,\text{incl}} = \frac{\sigma_a\,\sigma_b}{(1+\delta_{ab})\,\sigma_{\text{eff}}}\,, \tag{5.8}$$

which also gives the right formula in case of identical scattering types ($a \equiv b$), where it introduces the combinatorial factor of two in the denominator.

5.2 Like sign di-lepton production

There are several analyses where double parton scattering contributions to various processes have been studied at lower energies [124–130]. We will use like sign di-lepton production (from like sign Ws in the double parton scattering case) to demonstrate the successful operation of the double parton scattering simulation inside our model of multiple interactions. We will examine the event properties of double Drell-Yan events as suggested in Ref. [120] and depicted in Figure 5.1, but now with fully exclusive, *i.e.* hadronic, final-state simulation and decay of the W bosons. W production will be used as a *standard candle* for Standard Model physics and like sign W pair production may as well be used to measure and calibrate double parton scattering. To what extend that is possible and in which kinematical regions that is achieved most easily is subject of the subsequent

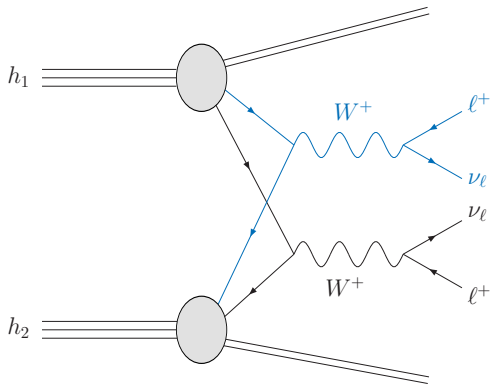

Figure 5.1: Diagram of the double parton scattering event with two W^+ bosons produced in Drell Yan processes that leads to the signature $pp \to \ell_1^+\ell_2^+ + \text{jets} + \not{E}_t$. The normally invoked parton showers as well as additional QCD-like multiple interactions are not drawn.

sections.

Additionally, like sign di-lepton production is a very distinct signature that appears in various models of physics beyond the Standard Model (BSM). Analyses searching for Supersymmetry using this channel are for example discussed in Ref. [131]. We will also discuss the background contribution to these analyses arising from double parton scattering.

5.2.1 Simulation

Using the definition above, it is clear that double parton scattering is a subset of our multiple scattering model, where the additional interactions fluctuate up, in scales, to the level of the *hard* interaction. This is of course very inefficient since the rate at which these fluctuations would appear without changing the cross section,

$$\mathcal{R} \sim \frac{\sigma_{\text{signal}}}{\sigma_{\text{ue}} + \sigma_{\text{signal}}}\,, \tag{5.9}$$

is very small in all cases of interest. We therefore introduced the possibility in Herwig++ to exclusively request the number of additional scatters of a certain type using specific cuts. We describe these settings in detail in Appendix A.4.

Figure. 5.1 shows the process that was requested to simulate the double parton scattering background to like sign di-lepton production. The total cross section for these events has to be reweighted though. Equation (5.8) will give the correct cross section for this process. All histograms are normalised to this cross section, which is then compared to the Standard Model background to the di-lepton signal $pp \to \ell_1^+ \ell_2^+ + \text{jets} + \not{E}_t$. At leading order the subprocesses considered are

$$q_1 q_2 \to \ell_1^+ \ell_2^+ \nu_{\ell_1} \nu_{\ell_2} \; q_1' q_2' \,, \tag{5.10}$$

with $q = u, c$ and $q' = d, s$ and the crossed subprocesses. Some example Feynman diagrams for the subprocess $uu \to \ell_1^+ \ell_2^+ \nu_{\ell_1} \nu_{\ell_2} dd$ are shown in Fig. 5.2. We used `Madgraph` and `Madevent` [132, 133] to generate the parton level events and read them into Herwig++ where the parton showers, underlying event and hadronisation was performed. The Standard Model processes as well as the double parton scattering events are calculated using the CTEQ6L leading order PDFs [115].

5.2.2 Results

We begin our discussion of the results with the cross sections for the processes when minimal acceptance cuts,

$$\begin{aligned} p_{t,j} &> 5 \text{ GeV}, & p_{t,\ell} &> 5 \text{ GeV} \\ |\eta_j| &< 2.5, & |\eta_\ell| &< 2.5 \\ \Delta R_{jj}, \Delta R_{j\ell} &> 0.2, & \Delta R_{\ell\ell} &> 0.2 \,, \end{aligned} \tag{5.11}$$

are applied at the parton level. In addition to these basic cuts, we reconstruct the lepton pair by checking the highest p_t leptons for the same charge. A further requirement is the reconstruction of at least one jet from the coloured final-state particles. We used the k_t algorithm [29, 30] of the `FastJet` package [31] with $R = 0.7$ for the jet reconstruction. In the case $\ell_1 = e = \ell_2$, this yields the cross sections displayed in Table 5.1. The double parton scattering cross section is comparable to the Standard Model cross section, both are at $\mathcal{O}(1 \text{ fb})$.

The production characteristics in double parton scattering are of course different

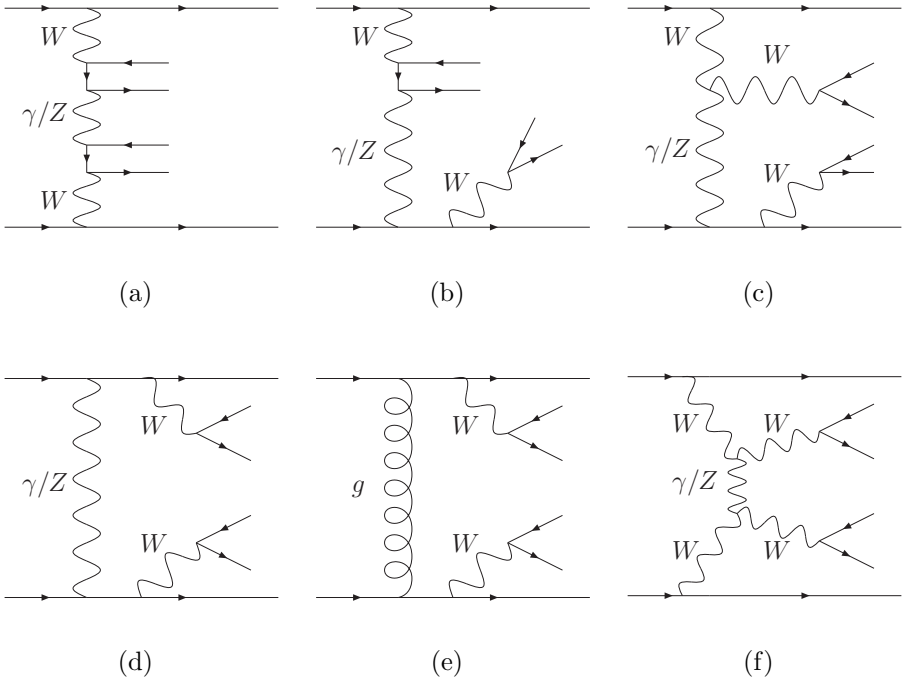

Figure 5.2: Examples of Feynman diagrams contributing to the subprocess $uu \to \ell_1^+ \ell_2^+ \nu_{\ell_1} \nu_{\ell_2} dd$. (e) is of $\mathcal{O}(\alpha_s^2 \alpha_{\mathrm{EW}}^4)$ whereas the others are at $\mathcal{O}(\alpha_{\mathrm{EW}}^6)$.

σ(fb)	SM $pp \to e^+e^+\nu\nu jj$	$2 \times qq \to W^+(\to e^+\nu)$
minimal cuts	2.29	1.52
$E_{t,j}^{\max} < 30$ GeV	0.09	1.28
$E_{t,j}^{\max} > 50$ GeV	2.05	0.12

Table 5.1: Cross sections in femtobarn for the Standard Model and double parton scattering process leading to the signature $pp \to e^+e^+ + \text{jets} + \not{E}_t$

to the Standard Model case. The p_t distribution of the charged leptons can be examined by the $p_{t,\ell}^{\max}$ ($p_{t,\ell}^{\min}$) observables. They measure the maximum (minimum) p_t of the two charged leptons for each event. Figures 5.3 and 5.4 show these observables comparing the two production mechanisms. The two independently produced W bosons in the double parton scattering case, result in lepton transverse momentum distributions that are peaked at similar values. The tails in these distributions are also much smaller than in the Standard Model case. This is

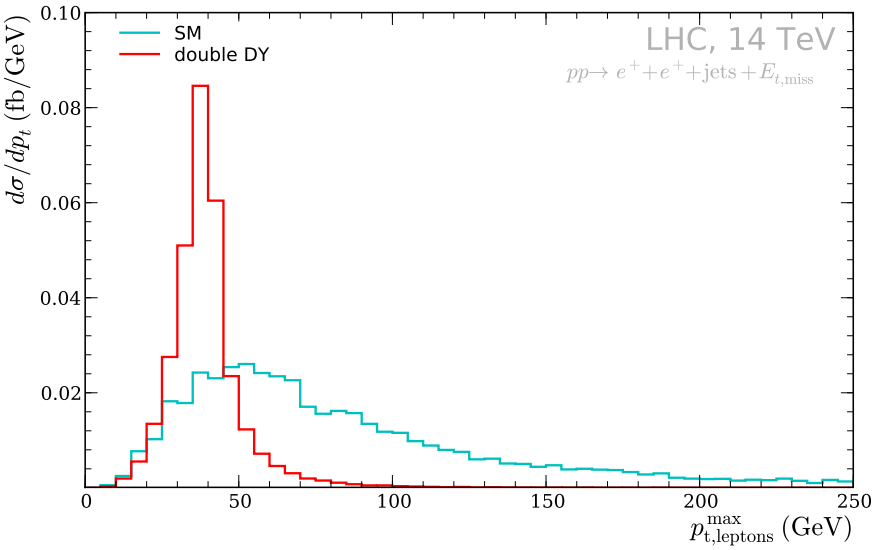

Figure 5.3: Differential cross section for the charged lepton maximum transverse momentum distribution. The Standard Model contribution is shown in cyan and the double parton scattering contribution in red.

due to the rather small transverse momentum at which the W boson is produced. The invariant mass of the lepton pair is the next observable we considered. It is displayed in Fig. 5.5 and is fairly similar for the two production processes. Double parton scattering again exhibits a more steeply falling distribution.

Our final-state required two charged, same sign leptons and at least one jet. We will have several jets in a typical event and decided to look only at the transverse energy (E_t) of the hardest jet. This observable has the largest discriminative power, which arises from the absence of any jet (apart from the proton remnants) in double parton scattering at the parton level. It leads to the steeply falling distribution shown in Fig. 5.6. To quantify this discriminative power we have chosen to use $E_{t,j}^{\text{max}}$ for a further cut. We considered two different scenarios. In the first one we consider double parton scattering as our signal and assume that we want to measure it in a very clean channel. This corresponds to a upper limit on the $E_{t,j}^{\text{max}}$ distribution. Restricting the maximum E_t of the jets to 30 GeV improves the signal to background ratio, $\sigma_{2\times\text{DY}}/\sigma_{\text{SM}} > 14$, tremendously. The inverse case, *i.e.* double parton scattering as background, can be covered by requiring a certain amount of transverse energy which automatically reduces the background contribution. For

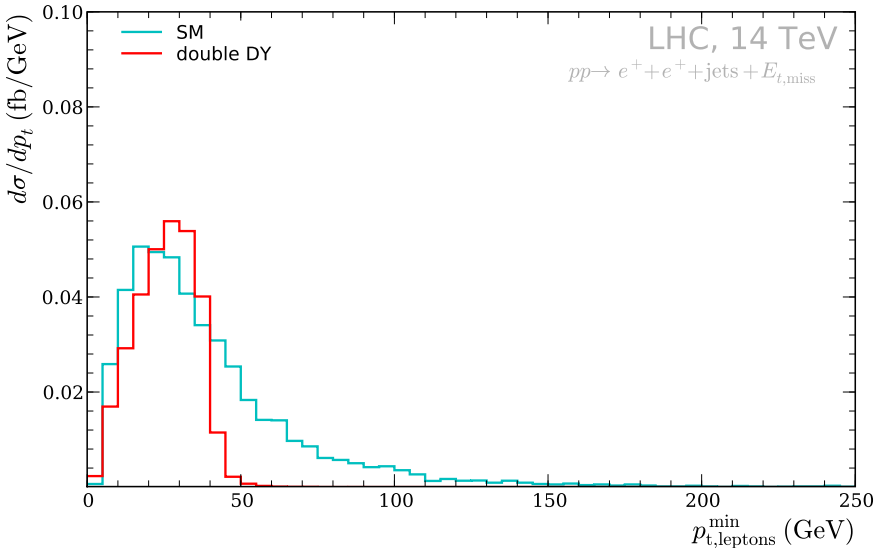

Figure 5.4: Differential cross section for the charged lepton minimum transverse momentum distribution. The Standard Model contribution is shown in cyan and the double parton scattering contribution in red.

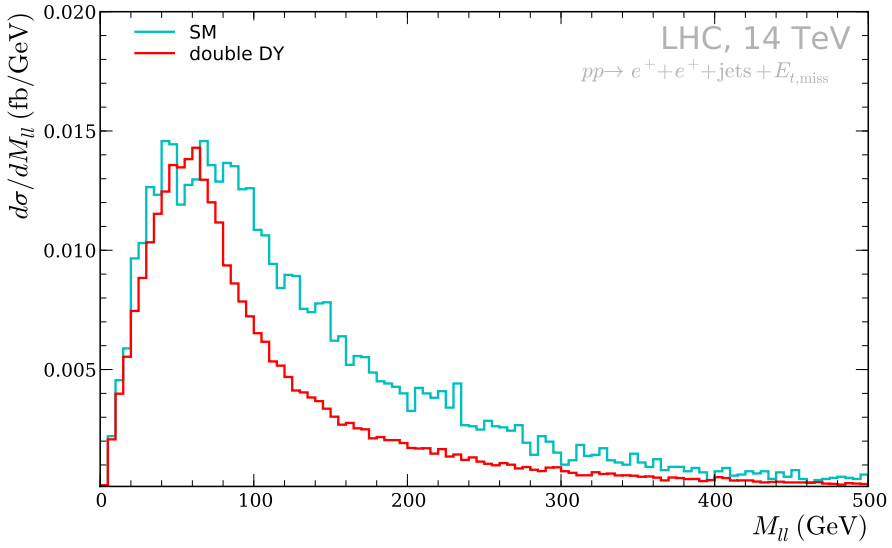

Figure 5.5: Differential cross section for the invariant mass distribution of the charge lepton pair. The Standard Model contribution is shown in cyan and the double parton scattering contribution in red.

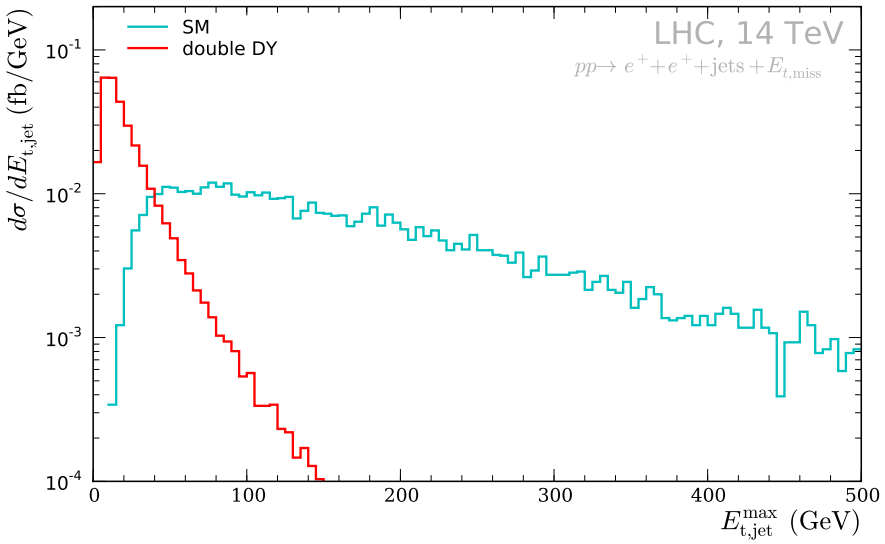

Figure 5.6: Differential cross section for the E_t distribution of the hardest jet. The Standard Model contribution is shown in cyan and the double parton scattering contribution in red.

$E_{t,j}^{\text{max}} > 50$ GeV the signal to background ratio exceeds 17. The cross sections using these additional cuts are also displayed in Table 5.1.

5.3 Conclusions

We have introduced the term double parton scattering and discussed the *effective cross section* as a way to quantify the rate at which double or multiple collisions of partons in the same hadronic interaction appear. We have seen that this rate is directly coupled to the partonic overlap in transverse space, once it is correctly defined. Thus, it offers a direct measurement of $A(\mathbf{b})$, which is a vital ingredient to most of the models that aim for a description of the underlying event in terms of multiple semi-hard scatterings. We then discussed the W^+W^+ channel in detail and examined how this channel would allow a measurement of double parton scattering. To simulate these events, we implemented and used a new infrastructure in Herwig++ that allows for an arbitrary combination of several hard interactions with completely independent cuts. This is an absolutely unique feature to this day.

We have seen that cutting on the $E_{t,j}^{\max}$ distribution eliminates the background process vastly. However, other sources of backgrounds may be important as well, but are left for further studies. The fake identification of charged leptons has not been considered for example. This opens up a large set of possible backgrounds, which don't need additional jets for charge conservation and may have a similar distribution of jets. Cross sections for these processes have to be weighted with the fake rate, which is typically at the per-mille level for leptons in the considered p_t range [134]. The influence of higher order corrections to the W production processes definitely distorts the spectrum of transverse energy of the additional jets. This could be studied using an algorithm [81, 135] to merge fixed (and higher) order matrix elements with the conventional all order resummation that the parton shower performs. We don't expect dramatic changes though. The parton shower is corrected for the first emission with respect to the full matrix element, which is known as *matrix element correction*. Changes will appear once higher jet multiplicities are considered, but as we are only interested in the hardest jet, the influence should be modest.

Finally, the considered double parton scattering process is a background to supersymmetric processes, where like sign di-leptons are produced. The potential of like sign di-muons in the search for Supersymmetry is discussed in Ref. [131]. Our results were obtained for the like sign di-electron channel but are of course almost unchanged when using muons instead. Like sign di-leptons in general can arise from gluino decays in various production channels because the gluino, being a Majorana particle, decays with equal probability to positively or negatively charged leptons. Squark production is another source of same sign di-leptons, since the squark charge tends to coincide with the valence quark charge of the colliding hadrons. The production mechanism always includes heavy (supersymmetric) resonances and therefore the jet transverse energy and missing transverse energy distributions are much broader than in the double parton scattering case. The analysis in Ref. [131] for example requires the hardest jet to have $E_{t,j}^{\max} > 175$ GeV, which reduces the double parton scattering signal to the level of $\mathcal{O}\,(1\text{ab})$, which is at least 3 orders of magnitude less than most of the considered BSM cross sections. We therefore conclude that these contributions to the total background can safely be neglected.

Chapter 6

Soft Interactions

Multiple partonic interactions are widely used to simulate the hadronic final-state in high energy hadronic collisions, and successfully describe many features of the data. It is important to make maximum use of the available physical constraints on such models, particularly given the large extrapolation from current high energy data to LHC energies. In eikonal models, the rate of multiparton interactions is coupled to the energy dependence of the total cross section. The eikonal formalism furthermore provides an unified description of additional scatters covering the entire transverse momentum spectrum. Hence, it removes the intrinsic deficiency of the model described in Chap. 4, which uses the perturbative jet cross section (above some transverse momentum cut-off) and therefore cannot describe events without any perturbative scale. Using a Monte Carlo implementation of such a model, we study the connection between the total cross section, the jet cross section, and the underlying event. By imposing internal consistency on the model and comparing to current data we constrain the allowed range of its parameters. We show that measurements of the total proton-proton cross section at the LHC are likely to break this internal consistency, and thus, to require an extension of the model. Likely such extensions are that semi-hard scatters probe a denser matter distribution inside the proton in impact parameter space than soft scatters, a conclusion also supported by Tevatron data on double-parton scattering, and/or that the basic parameters of the model are energy dependent. In the second part of this chapter we describe the implementation of an extension, where semi-hard scatters probe a different matter distribution than soft scatters. We tune this model with

the CDF data that we already used in Chap. 4, and show extrapolations to the LHC.

6.1 Introduction

Hadron-hadron collision events at high energies often contain high transverse energy jets, which in QCD arise from gluon or quark (generically, parton) scattering followed by QCD radiation and hadronisation. This model is generally taken to be realistic above some minimum transverse momentum scale, $p_t^{\min}$. The contribution of these events to the total cross section rises with hadron-hadron centre-of-mass energy, s, since the minimum value of the x probed is given by $(2p_t^{\min})^2/s$, and the parton densities rise strongly for $x < 10^{-2}$ or so [136, 137].

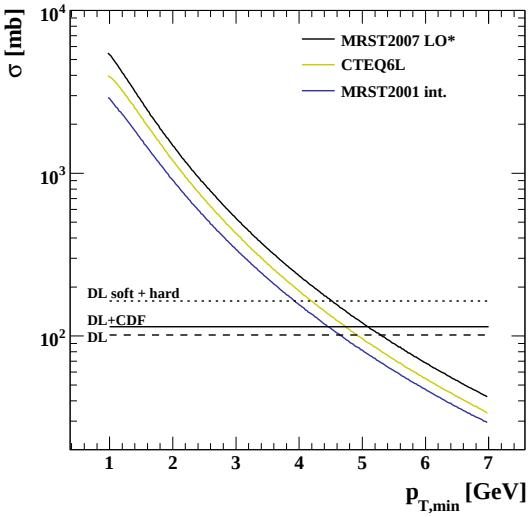

Figure 6.1: The inclusive hard jet cross section for three different proton PDFs, compared to various extrapolations of the non-perturbative fits to the total pp cross section at 14 TeV centre-of-mass energy.

One reason that this rising contribution to the cross section is of interest is that while perturbative QCD cannot predict total hadronic cross sections (since in many events no hard perturbative scale is present), rising hadronic cross sections are a feature also seen in successful non-perturbative approaches [6, 7], the behaviour of which must presumably emerge from the QCD Lagrangian in some manner. Thus by comparing the behaviour of the hard contribution to the cross section to the behaviour expected from fits to the total cross section, it may be possible to learn something about the connection between these approaches and about hadronic cross sections in general.

The connection between the hard partonic cross section and the total cross section is not one-to-one, however. There are certainly hadronic scatters in which no hard jets are produced, and some non-perturbative scattering process must be added to the perturbative jet contribution to model the total cross section. In addition, at the high parton densities probed at recent, current and future colliders, simple assumptions lead to the conclusion that the probability of multiple partonic scatters in a single hadron-hadron collision is significant. In fact, Fig. 6.1 shows that for $p_t^{\min}$ values below about 5 GeV, the total "hard" cross section calculated assuming one parton-parton scatter per proton-proton collision *exceeds the total cross section* as extrapolated using the non-perturbative fits, at LHC energies. This means that there is no room left for any elastic or soft contribution to the total cross section and strongly implies that the average number of partonic scatters in an inelastic collision must be greater than one.

Introducing the possibility of such multiparton interactions also seems to be required in order to describe the hadronic final-state [84, 109, 138]. In general, softer additional scatters occurring in a high-p_t event manifest themselves as additional particles and energy-flow, the underlying event.

In the first sections of this chapter we examine the predictions of the model that was implemented in [35, 85, 90, 121] including the possibility of soft scatters. We explore the consistency constraints that would be imposed by comparing a given value of the total cross section to the predicted jet cross section, and attempt to identify allowed regions of parameter space within which the model must lie if it is to be consistent with the measured cross section at the LHC. We also discuss ways in which energy dependencies in the parameters could arise, and their impact upon these constraints. The studies are all carried out using the new implementation in Herwig++ [35, 121]; however, they are also relevant to the fortran implementation JIMMY [85], if the same hard cross section is used.

6.2 Total and elastic cross section parameterisations

Throughout these sections we will exploit the connection that can be established between the eikonal model of Refs. [85, 90, 121] and the total cross section. To give

a reasonable range of expectations for the latter, we use the successful parameterisation of Donnachie and Landshoff [6, 7]. We will use three different variations;

1. The *standard* parameterisation from [6] with the following behaviour at high energies:

$$\sigma_{\text{tot}} \sim 21.7 \text{ mb} \cdot \left(\frac{s}{\text{GeV}^2}\right)^{0.0808} \rightarrow \sigma_{\text{tot}}(14 \text{ TeV}) = 101.5 \text{ mb}\,. \tag{6.1}$$

2. Using the same energy dependence but normalising it to the measurement [139] by CDF:

$$\sigma_{\text{tot}} \sim 24.36 \text{ mb} \cdot \left(\frac{s}{\text{GeV}^2}\right)^{0.0808} \rightarrow \sigma_{\text{tot}}(14 \text{ TeV}) = 114.0 \text{ mb}\,. \tag{6.2}$$

3. Using the most recent fit [7], which takes the contributions from both hard and soft Pomerons into account:

$$\begin{aligned} \sigma_{\text{tot}} &\sim 24.22 \text{ mb} \cdot \left(\frac{s}{\text{GeV}^2}\right)^{0.0667} + 0.0139 \text{ mb} \cdot \left(\frac{s}{\text{GeV}^2}\right)^{0.452} \\ \rightarrow \sigma_{\text{tot}}(14 \text{ TeV}) &= 164.4 \text{ mb}\,. \end{aligned} \tag{6.3}$$

Other parameterisations and models for the total cross section exist [140, 141], but their predictions for the total cross section at 14 TeV generally lie within the range covered by these three[1]. As will be seen, the range is wide, and early measurements of the total cross section at the LHC can be expected to have a big impact [144].

We will also find it useful to compare our model with the elastic slope parameter, b_{el}, defined in terms of the differential elastic scattering cross section, $\mathrm{d}\sigma/\mathrm{d}t$, as

$$b_{\text{el}}(s) = b_{\text{el}}(s, t = 0) = \left[\frac{\mathrm{d}}{\mathrm{d}t}\left(\ln\frac{\mathrm{d}\sigma}{\mathrm{d}t}\right)\right]_{t=0}. \tag{6.4}$$

In the Donnachie-Landshoff parameterisation, this is given by:

$$b_{\text{el}}(s) = 2\alpha' \ln\frac{s}{s_0} \tag{6.5}$$

[1] The most recent models of [142, 143] predict $\sigma_{\text{tot}}(14 \text{ TeV}) \simeq 90$ mb, which is 10 % below the smallest expectation we use. Since the difference this introduces is similar to the one between our first and second parameterisation it can easily be estimated by the reader.

with $\alpha' = 0.25$ GeV^{-2}. Together with the CDF data[145], this implies

$$\begin{aligned} b_{\text{el}}(s) &= \left(\ln \frac{\sqrt{s}}{1800 \text{ GeV}} + (17 \pm 0.25) \right) \text{ GeV}^{-2} \\ &= \left(\ln \frac{\sqrt{s}}{14 \text{ TeV}} + (19 \pm 0.25) \right) \text{ GeV}^{-2}. \end{aligned} \tag{6.6}$$

The most recent fit[7] has the same value for α' and hence b_{el}, while those of [140, 141] are a little higher: 20–22 GeV^{-2}. We therefore use the CDF value for the Tevatron energy and the range 19–22 GeV^{-2} to represent the range of possible measurements from the LHC.

6.3 Eikonal model

We have seen in Sect. 2.1.2, that the scattering amplitude $\mathcal{A}(s,t)$ can, in the Regge limit, be expressed as the Fourier transform of the elastic scattering amplitude $a(\mathbf{b}, s)$ in impact parameter space (Eq. (2.17)) as

$$\mathcal{A}(s,t) = 4s \int \mathrm{d}^2\mathbf{b} \;\; a(\mathbf{b}, s)\, e^{i\mathbf{q}\cdot\mathbf{b}} \;\; ,$$

where $\mathbf{q}$ is the transverse momentum transfer vector, with, in the high energy limit, $\mathbf{q}^2 = -t$. In this limit, $a(\mathbf{b}, s)$ can be assumed to be purely imaginary and therefore be expressed in terms of a real eikonal function $\chi(\mathbf{b}, s)$, as

$$a(\mathbf{b}, s) = \frac{1}{2i} \left[e^{-\chi(\mathbf{b},s)} - 1 \right] . \tag{6.7}$$

The total pp ($p\bar{p}$) cross section as well as the elastic cross section can be obtained from that parameterisation as (Eq. (2.18)),

$$\sigma_{\text{tot}}(s) = 2 \int \mathrm{d}^2\mathbf{b} \;\; \left[1 - e^{-\chi(\mathbf{b},s)} \right] , \qquad \sigma_{\text{el}}(s) = \int \mathrm{d}^2\mathbf{b} \;\; \left| 1 - e^{-\chi(\mathbf{b},s)} \right|^2 . \tag{6.8}$$

The inelastic cross section is obtained as the difference between the two cross

sections and therefore counts non-diffractive as well a diffractive processes

$$\begin{aligned}\sigma_{\text{inel}} &= \sigma_{\text{tot}} - \sigma_{\text{el}} \\ &= \int \mathrm{d}^2\mathbf{b} \quad \left[1 - \; e^{-2\chi(\mathbf{b},s)}\right] .\end{aligned} \tag{6.9}$$

The elastic slope parameter at zero momentum transfer is also calculable within this framework and yields [2]

$$b_{\text{el}} = \frac{1}{\sigma_{\text{tot}}} \int \mathrm{d}^2\mathbf{b}\; b^2 \quad \left[1 - \; e^{-\chi(\mathbf{b},s)}\right] . \tag{6.10}$$

In the first step we want to reproduce the results from Chap. 4, before we extend that model to include also scatters below the transverse momentum cut-off. This can be done by comparing the inelastic cross sections in the two models, *i.e.* Eq. (4.15) and (6.9) and yields the simple relation

$$\chi(\mathbf{b}, s) = \frac{1}{2}\langle n(\mathbf{b}, s)\rangle . \tag{6.11}$$

We identify this as the *hard* part of a universal eikonal function, which then has the form,

$$\chi_{\text{tot}}(\mathbf{b}, s) = \chi_{\text{QCD}}(\mathbf{b}, s) + \chi_{\text{soft}}(\mathbf{b}, s) , \tag{6.12}$$

with the perturbative part

$$\chi_{\text{QCD}}(\mathbf{b}, s) = \frac{1}{2} A(\mathbf{b})\; \sigma^{\text{inc}}_{\text{hard}}(s; p_t^{\text{min}}) . \tag{6.13}$$

That is, we assume that the distribution of partons in hadrons factors into an impact parameter dependence, independent of the longitudinal momentum fraction dependence. Here $\sigma^{\text{inc}}_{\text{hard}}$ denotes the inclusive cross section above a transverse momentum cutoff $p_t > p_t^{\text{min}}$. $A(\mathbf{b})$ describes the overlap distribution of the partons in impact parameter space.

In the models of Refs. [90, 146, 147], the soft eikonal function has the form

$$\chi_{\text{soft}}(\mathbf{b}, s) = \frac{1}{2} A_{\text{soft}}(\mathbf{b})\; \sigma^{\text{inc}}_{\text{soft}} , \tag{6.14}$$

where $\sigma_{\text{soft}}^{\text{inc}}$ is the purely non-perturbative cross section below p_t^{min}, which is a free parameter of the model. That is, we assume that soft scatters are the result of partonic interactions that are local in impact parameter.

The elastic slope parameter discussed above relates to bulk interactions of the proton. Thus it can be taken as directly constraining the matter distribution "seen" by soft scatters. Higher p_t scatters might be expected to see a different matter distribution, for example they might probe denser "hot spots" within the proton. However, at present we take the simplest assumption for the perturbative part of the eikonal function, *i.e.* that the semi-hard scatters "see" the same matter distribution as the soft ones and therefore take $A(\mathbf{b}) \equiv A_{\text{soft}}(\mathbf{b})$. This is clearly a simplifying assumption, but offers us the possibility to study the model in a generic way.

According to the definition in Eq. 6.9, the inelastic cross section contains all inelastic processes, including diffraction. This is not in contradiction with the definition of the inclusive hard cross section, which is calculated from the conventional parton distribution functions, which describe the *inclusive* distribution of partons in a hadron whatever their source, *i.e.* whether the proton remains intact or not. Thus the model of the final-state of the partonic collisions should include this diffractive fraction of events. This would be particularly important when implementing a model for the final-state of $\sigma_{\text{soft}}^{\text{inc}}$.

6.3.1 Overlap parameterisation

The only remaining freedom in the eikonal model is the functional form of the overlap function $A(|\mathbf{b}| = b)$. $A(b)$ is the convolution of the individual spatial parton distributions of the colliding hadrons,

$$A(b) = \int d^2\mathbf{b}' \; S_{h_1}(|\mathbf{b} - \mathbf{b}'|) \; S_{h_2}(|\mathbf{b}'|) \, . \tag{6.15}$$

In Chap. 4 we have used $S(\mathbf{b})$ proportional to the electromagnetic form factor as suggested in Ref. [148],

$$S_{\bar{p}}(\mathbf{b}) = S_p(\mathbf{b}) = \int \frac{d^2\mathbf{k}}{(2\pi)^2} \frac{e^{i\mathbf{k}\cdot\mathbf{b}}}{(1+\mathbf{k}^2/\mu^2)^2} \ . \tag{6.16}$$

μ is the only parameter and has the dimensions of an inverse radius. In ep scattering its value was measured to be 0.71 GeV^2. This is a loose constraint, since the distribution of partons may not necessarily coincide with the distribution of electromagnetic charge. Actually, using the results from the previous section, the CDF data on the total cross section ($\sigma_{\rm tot} = 81.8 \pm 2.3$ mb [139]) and the elastic slope ($b_{\rm el} = 16.98 \pm 0.25$ GeV^{-2} [145]) one can solve for the total inclusive cross section and for μ^2, yielding $\mu^2 = 0.56 \pm 0.01$ GeV^2.

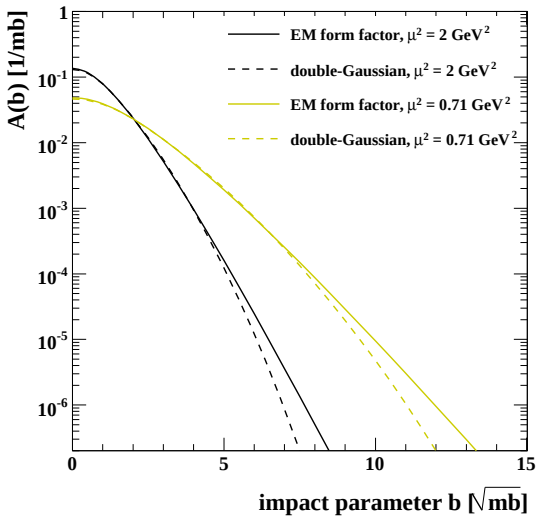

Figure 6.2: $A(b)$ for the two parameterisations.

In order to investigate the dependence on the assumed shape of the matter distribution, we have compared our default results with those obtained with a double-Gaussian distribution, as chosen in Refs. [38, 39, 96],

$$S(b) = \frac{1-\beta}{\pi r^2} \cdot e^{-\frac{b^2}{r^2}} + \frac{\beta}{\pi (k\cdot r)^2} \cdot e^{-\frac{b^2}{(k\cdot r)^2}} \ . \tag{6.17}$$

Here β, k and r are all free parameters, but we choose to fix β and k at values that are reasonably generic, but also close to the tuned values used in [38, 39, 96], with the relative strengths given by $\beta = 0.5$ and the relative widths by $k = 2$, and view r as the only free parameter. The parameters μ^2 and r in the two models are arbitrary and should ultimately be fit to data. However, in order to have a like-for-like comparison, we choose to relate them in such a way that the rms value of

$S(b)$ is identical. That is, we describe the double-Gaussian also as being a function of μ^2, with r set via b_{rms}. We illustrate the shapes of the two resulting overlap functions for two different values of μ^2 in Fig. 6.2.

We find that for small values of μ^2 (~ 1 GeV^2) the results of the two models are extremely similar, differing at most by ± 2 %. For large values (~ 3 GeV^2) they differ more, the double Gaussian distribution giving a larger de-eikonalised cross section (see next section) by between 30 % with the standard Donnachie–Landshoff total cross section prediction at the LHC and 150 % with the soft+hard Pomeron prediction. While these lead to somewhat different predictions, in our final results they effectively correspond to a distortion of the μ^2 axis. The effect on our final plots, Figures 6.6-6.8, is small, since our consistency requirement is mainly active at small μ^2.

6.3.2 Connection to the total cross section

For a given point in the parameter space $(p_t^{\min}, \mu^2)$ of our model, we are able to calculate $\chi_{\rm QCD}$ using Eq. 6.13. The remaining uncertainty is in $\sigma_{\rm hard}^{\rm inc}(s; p_t^{\min})$, which depends on the PDF choice, the treatment of α_s etc. If we now choose a value for the non-perturbative cross section below $p_t^{\min}$, $\sigma_{\rm soft}^{\rm inc}$, we have the full eikonal function,

$$\chi_{\rm tot}(\mathbf{b}, s) = \frac{1}{2} A(b)(\sigma_{\rm hard}^{\rm inc} + \sigma_{\rm soft}^{\rm inc}) \,,$$

at hand and can calculate the total cross section from Eq. (6.8).

We will, however, turn this argument around and use predictions [6, 7] for the total cross section as input to fix the additional parameter in our non-perturbative part of the eikonal function ($\sigma_{\rm soft}^{\rm inc}$). To examine the validity of that procedure, we extracted the sum $\sigma_{\rm hard}^{\rm inc} + \sigma_{\rm soft}^{\rm inc} \equiv \sigma_{\rm de-eik}$ from Eq. (6.8), which now reads

$$\sigma_{\rm tot}(s) = 2 \int {\rm d}^2\mathbf{b} \, \left[1 - \, e^{-\frac{1}{2} A(b) \sigma_{\rm de-eik}} \right] \,,$$

for a given value of μ^2 and a given value of the total cross section. We will call this cross section the *de-eikonalised* cross section. In Fig. 6.3 we plot the de-

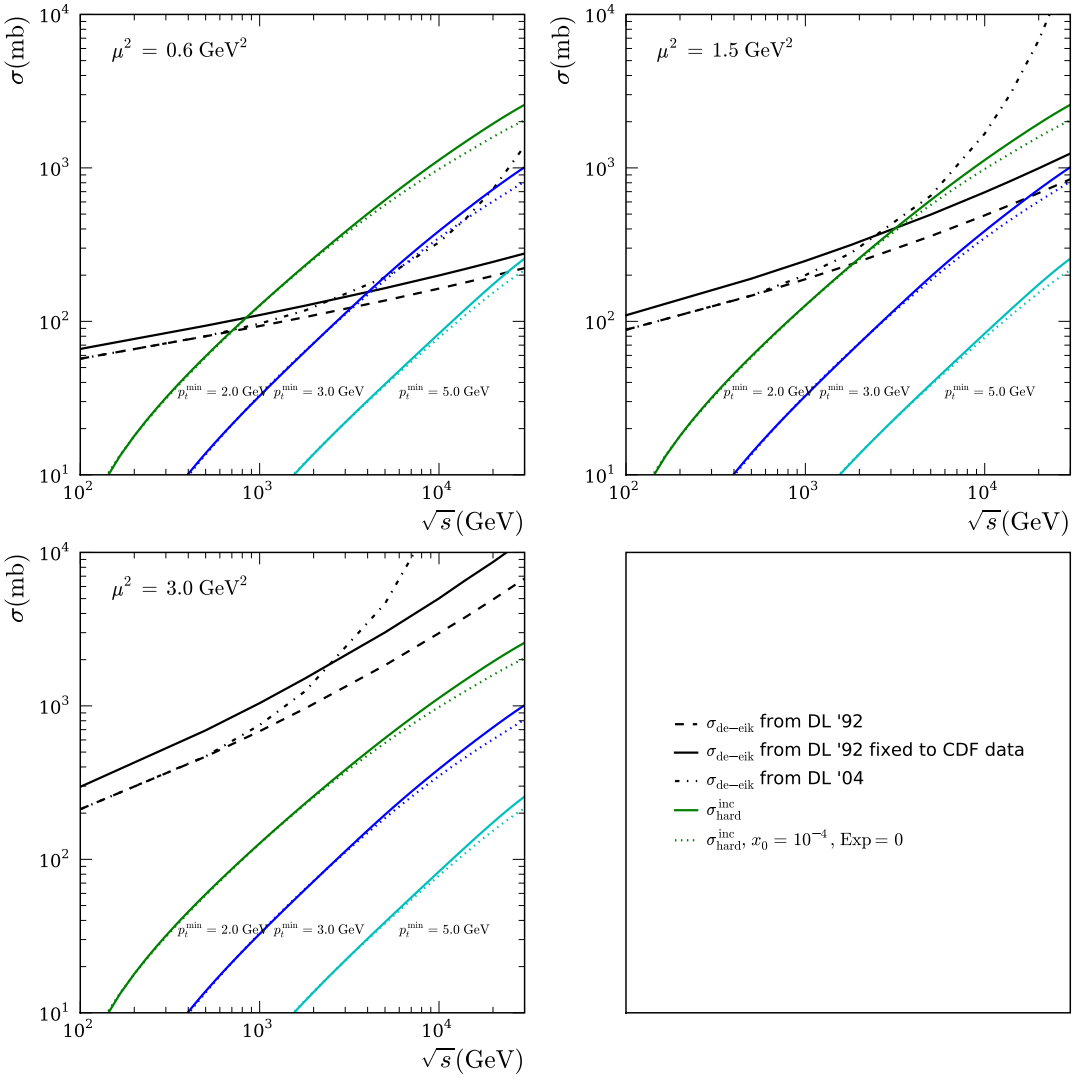

Figure 6.3: Cross sections in millibarn as a function of the centre-of-mass energy in GeV. The three different plots vary the value of μ^2 from 0.6 to 3 GeV^2. The black curves show de-eikonalised total cross sections. We use the total cross section parameterisation of Ref. [6] for the dashed curves. The solid curves use the same exponent, but the normalisation is rescaled to fit the total cross section measurement of CDF. The dashed-dotted curve uses the parameterisation of Ref. [7]. The coloured solid curves show $\sigma_{\text{hard}}^{\text{inc}}$ for different values of $p_t^{\min}$. The coloured dotted curves incorporate the simple small-x deviations discussed in Sect. 6.3.3.

eikonalised cross sections for the three different total cross section extrapolations as a function of the centre-of-mass energy. Furthermore we show the value of $\sigma_{\text{hard}}^{\text{inc}}$ using different cutoffs. $\sigma_{\text{soft}}^{\text{inc}}$ is now given by the difference of these curves. This has the implication that whenever the inclusive hard cross section is larger than the de-eikonalised one, the model is not able to reproduce the total cross section as expected. We will investigate this behaviour in more detail in Sect. 6.4.1.

From the plots in Fig. 6.3 the values for $\sigma_{\text{soft}}^{\text{inc}}$ can in principle be read off. However, due to the logarithmic scale it is not easy to see what is implied for the energy dependence of the soft cross section. Therefore, for selected points in parameter space, $\sigma_{\text{soft}}^{\text{inc}}$ is shown separately in Fig. 6.4. Note that where the de-eikonalised line for $p_t^{\min} = 3.0$ GeV crosses and re-crosses the total cross section extrapolation in the top left plot of Fig. 6.3, the soft cross section in the top left plot of Fig. 6.4 first becomes negative and then positive again. The dependence of $\sigma_{\text{soft}}^{\text{inc}}$ on the centre-of-mass energy reveals two main points: First, it is noticeable that one observes a more-or-less constant behaviour with increasing energy only in a limited range of our parameter space. This behaviour is mainly present for lower values of μ^2. Second, for the most extreme total cross section prediction, $\sigma_{\text{hard}}^{\text{inc}}$ is *never* sufficient to explain the strong rise with energy. There, essentially all parameter choices require a strongly rising *soft* cross section, in addition to the expected strong rise in the hard cross section. This is, at very least, counter-intuitive.

6.3.3 Parton saturation physics

The main motivation for allowing multiparton scatterings is the rise of the inclusive cross section, for fixed $p_t^{\min}$, with increasing centre-of-mass energy. Multiparton scattering provides a mechanism to allow this quantity to exceed the total cross section. Eikonal models that incorporate this fact unitarise the inclusive cross section. There is however a second source of unitarisation, the physics of parton saturation, which is a competing effect. To estimate the influence on our studies, we have used a simple modification of the PDFs recently introduced [36] into Herwig++ to mimic parton saturation effects for any PDF. The modification replaces

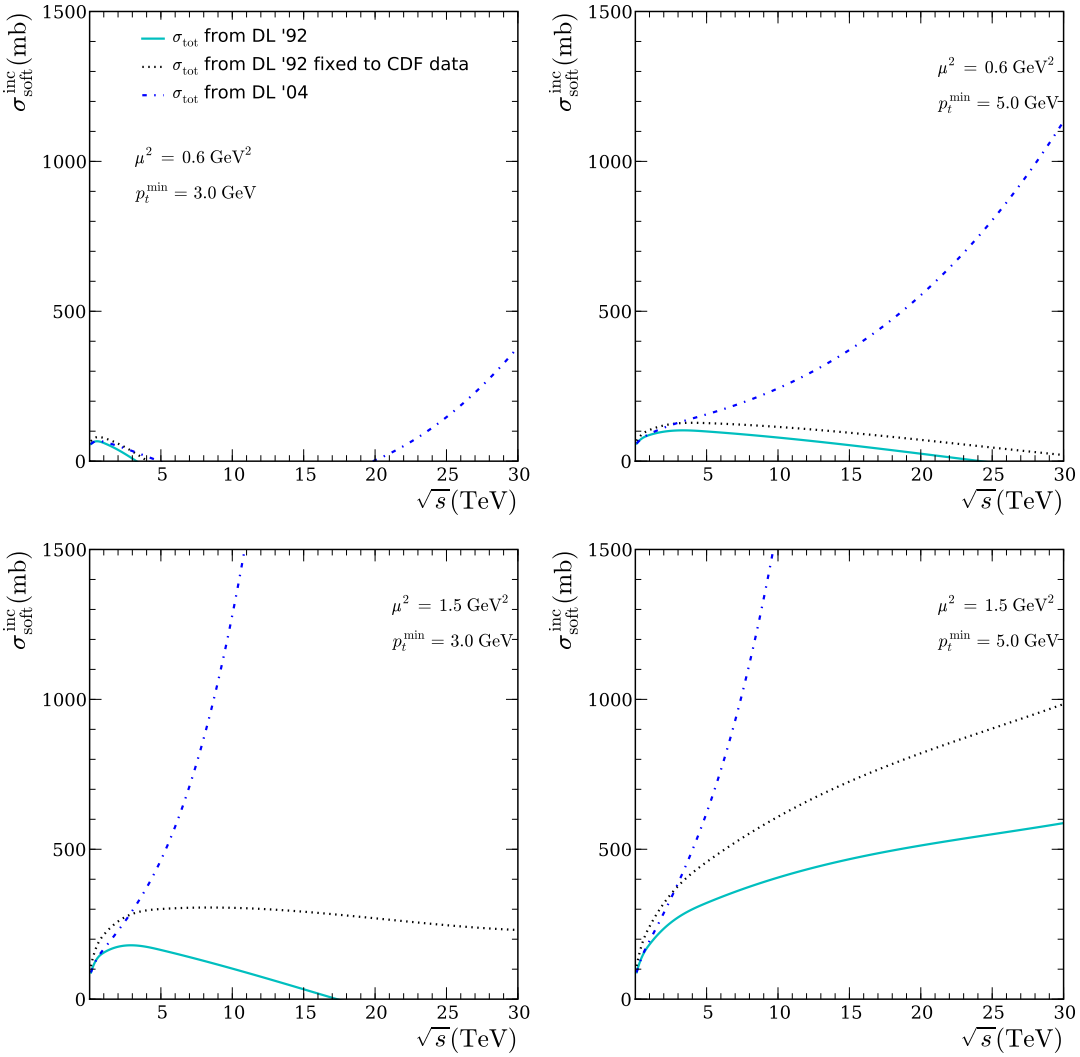

Figure 6.4: $\sigma_{\rm soft}^{\rm inc}$ for four different points in parameter space. Each of the three different curves shows the soft cross section that would appear when the respective parameterisation for the total cross section is used as input to fix $\sigma_{\rm soft}^{\rm inc}$.

$xf(x)$ below x_0 by

$$xf(x) \to \left(\frac{x}{x_0}\right)^{\alpha} x_0 f(x_0) \quad \forall\, x < x_0\,, \tag{6.18}$$

where x_0 and α are changeable parameters. HERA data indicate that saturation is unlikely to be a strong effect above $x \approx 10^{-4}$. Therefore, the strongest reasonable influence from this effect is obtained by setting $x_0 = 10^{-4}, \alpha = 0$. The results are shown in Fig. 6.3, where the effect is visible, but small, at LHC energies.

6.4 Parameter space constraints from data

In discussing the de-eikonalised cross section, we noted that for some parameter values the hard partonic cross section exceeds it. This implies in our model that the soft cross section should be negative. We take this as an inconsistency that would, for a given measured σ_{tot} at the LHC, rule out such parameter space points. In this section we discuss the extent to which the space of parameter values can be limited by this and other constraints.

6.4.1 Consistency

The parameter space in μ^2 and $p_t^{\min}$ is shown in Fig. 6.5 for the Tevatron, and Figs. 6.6-6.8 for the LHC.

The horizontal band shows the range of μ^2 values allowed for a given value of the elastic slope, calculated with Eq. (6.10), in conjunction with the indicated σ_{tot}. For Tevatron energies, both b_{el} and σ_{tot} are chosen according to the CDF measurement from Refs. [139] and [145] respectively.

Our expectations on the value of the elastic slope at LHC energies simply reflect the range of predictions that the models of [6, 7, 140, 141] give, as discussed in Sect. 6.2. For the value of σ_{tot} at the LHC we show a range of possible values motivated by these parameterisations.

For a particular value of σ_{tot} (or for a given range of possible values at the LHC),

we are able to extract constraints on the allowed parameters, by simply requiring a sensible performance of the eikonal model. The most basic requirement, which was just mentioned, is that the non-perturbative cross section that is needed to match the total cross section prediction is positive. A negative value means that the model cannot be applied and therefore this requirement puts a stringent limit on the allowed values of μ^2 and $p_t^{\min}$. This limit will depend on the value of $\sigma_{\text{hard}}^{\text{inc}}$, which is not a stable prediction itself. We therefore calculate this limit with several variations. We use three different PDF sets [114, 115, 149], vary the running of α_s from 1-loop, which is the default in Herwig++ to 2-loop and finally apply the modifications to the PDF's described in Sect. 6.3.3. The solid lines in Figs. 6.5 and 6.6-6.8 show these limits, where the entire range below the curves is excluded. The limits impose a minimal μ^2 for any given value of $p_t^{\min}$. Points on that line are parameter sets where $\sigma_{\text{soft}}^{\text{inc}} = 0$ mb.

Another, weaker, consistency constraint we apply is related to the simulation of the final-state of these collisions. We observe that when we embed them into the full simulation of Herwig++, including backward evolution of the initial-state, each collision consumes, on average, about a tenth of the available total energy, so that the approximation that individual semi-hard scatters are independent must break down, at least due to energy conservation, when there are more than about ten of them. We therefore indicate on Figs. 6.6-6.8 the points in parameter space where the average multiplicity of scatters above $p_t^{\min}$ reaches 10. This is certainly not a stringent limit but a sensible parameter choice most likely avoids this region.

The classic CDF analysis of the distribution in azimuth of the mean charged multiplicity and scalar p_t sum as a function of the transverse momentum of the leading jet[109] also provides constraints on the model as embedded in Herwig++. Chapter 4 described the implementation of multiparton scattering into Herwig++ (*i.e.* the simulation of the final-state corresponding to $\sigma_{\text{hard}}^{\text{inc}}$) and made a two-parameter fit (μ^2 and $p_t^{\min}$) to these data. Since this fit was obtained without a simulation of the final-state corresponding to $\sigma_{\text{soft}}^{\text{inc}}$, we do not take the results of this fit as a strong constraint on the parameter space, but an indication of the effect such a tuning could have once a complete description is available. The result is that, although one obtains a best fit with the values $\mu^2 = 1.5$ GeV^2, $p_t^{\min} = 3.4$ GeV, the best-fit values of the parameters are strongly correlated, with the χ^2 function hav-

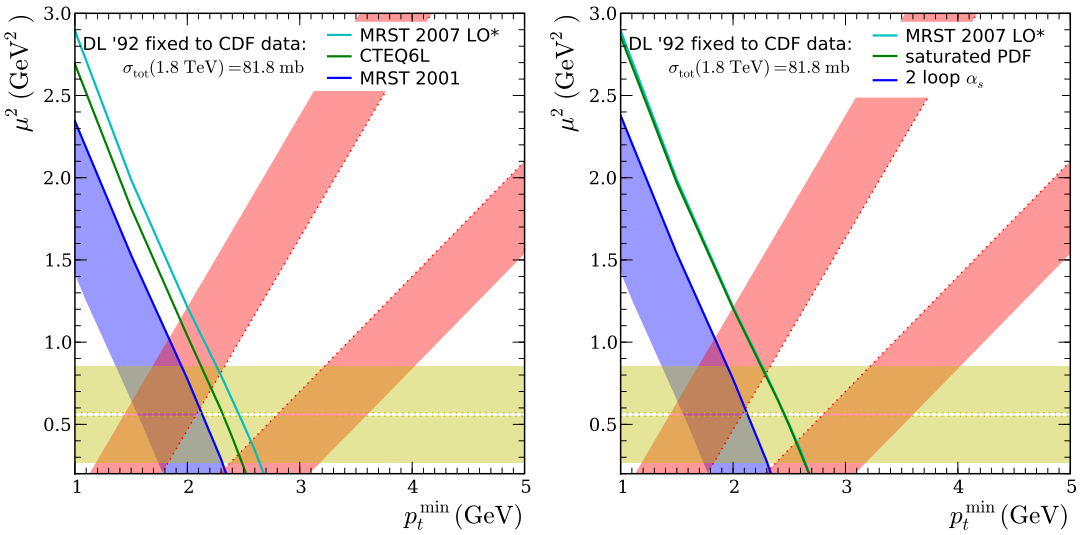

Figure 6.5: The plots show the parameter space of the eikonal model at Tevatron energies. The solid curve imposes a minimum allowed value of μ^2, for a given value of $p_t^{\rm min}$ by requiring a positive value of $\sigma_{\rm soft}^{\rm inc}$. The horizontal lines correspond to the measurement of $b_{\rm el} = 16.98 \pm 0.25$ GeV^{-2} from CDF [139]. The excluded regions are shaded. The dashed lines constitute the boundaries of the preferred parameters for a fit to Tevatron final-state data from Ref. [121], which used the MRST2001 PDF set. The left plot shows the PDF uncertainty by varying the PDF set. The right plot shows the uncertainty that is implied by using 2-loop α_s running and using the saturation modifications.

ing a long, thin, rather flat valley running from ($p_t^{\rm min} = 2.5$ GeV, $\mu^2 \sim 0.7$ GeV^2) to ($p_t^{\rm min} = 4.5$ GeV, $\mu^2 \sim 2.5$ GeV^2), and beyond. For any given value of $p_t^{\rm min}$ in this range one can find a μ^2 value that gives a good description of these data.

Combining these constraints at the Tevatron, a small allowed region remains around $p_t^{\rm min} = 2.3$ GeV and $\mu^2 = 0.6$ GeV^2.

At the LHC, this region would be ruled out for all the values of $\sigma_{\rm tot}$ we have considered. Note that if the LHC measurement were as high a 164 mb, this would on its own imply an energy-dependent μ^2, in contradiction with our initial assumptions.

In the next section we discuss different ways in which the assumptions of the model might be modified to account for this potential inconsistency.

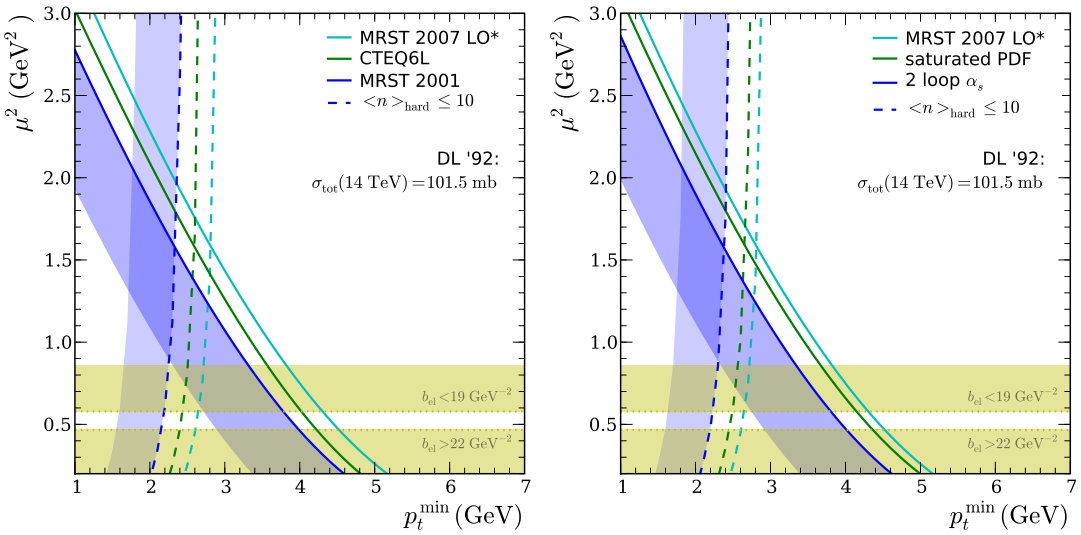

Figure 6.6: The plots show the parameter space of the eikonal model and three constraints assuming a total cross section behaviour as predicted in [6]. The first one drawn as solid curve imposes a minimum allowed value of μ^2, for a given value of $p_t^{\min}$ by requiring a positive value of $\sigma_{\text{soft}}^{\text{inc}}$. The second one, in dashed lines is deduced from an upper limit of the average number of additional semi-hard scatters in a typical minimum bias event. The excluded regions are shaded. The third constraint comes from the expected range of values for the elastic slope $b_{\text{el}} \in [19 - 22]$ GeV^{-2}. The left column shows the PDF uncertainty by varying the PDF set. The right column shows the uncertainty that is implied by using 2-loop α_s running and using the saturation modifications.

6.4.2 Extensions to the model

Some authors have suggested, within multiparton scattering models, that the parameters of the model, analogous to our μ^2 and $p_t^{\min}$, should be energy dependent. In this section we briefly discuss the arguments for these models.

In [150] a simple model of the spatial/momentum structure of a hadron was constructed from which it was argued that the colour screening length decreases slowly with increasing energy. This translates into a $p_t^{\min}$ that increases slowly with energy, for which they estimated $p_t^{\min} \sim s^{\epsilon}$ with ϵ in the range 0.025 to 0.08. The actual value used in Refs. [38, 39, 96] is 0.08, leading to a 35% increase in $p_t^{\min}$ from the Tevatron to the LHC.

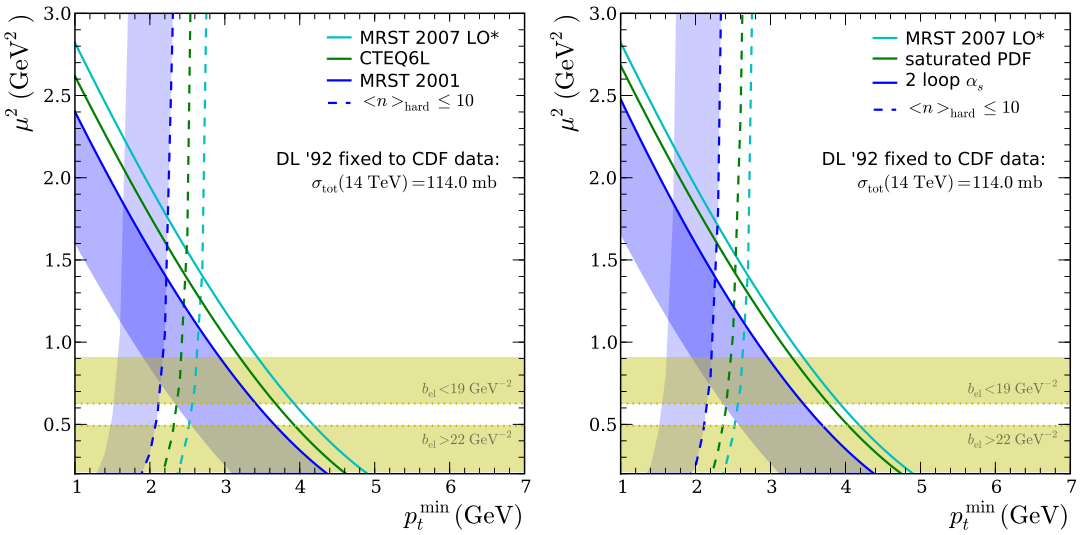

Figure 6.7: The plots show the parameter space of the eikonal model and three constraints assuming a total cross section behaviour as predicted in [6], but rescaled to match the CDF measurement [139]. The first one drawn as solid curve imposes a minimum allowed value of μ^2, for a given value of $p_t^{\min}$ by requiring a positive value of $\sigma_{\rm soft}^{\rm inc}$. The second one, in dashed lines is deduced from an upper limit of the average number of additional semi-hard scatters in a typical minimum bias event. The excluded regions are shaded. The third constraint comes from the expected range of values for the elastic slope $b_{\rm el} \in [19 - 22]$ GeV^{-2}. The left column shows the PDF uncertainty by varying the PDF set. The right column shows the uncertainty that is implied by using 2-loop α_s running and using the saturation modifications.

In [151, 152] a multiparton model was constructed that is very similar to ours at low energy, with an impact parameter distribution of partons given by the electromagnetic form factor. However, soft gluon effects were estimated and summed to all orders, to give a mean parton-parton separation, b_{rms}, that falls with energy, quickly at first, but then saturating: the value at 1 TeV is about a factor of two smaller than at low energy, while the value at 14 TeV is only about 10% smaller still. In terms of our simple model in which the matter distribution always has the form factor form and is parameterised by μ^2, $\langle b^2 \rangle \propto 1/\mu^2$ and this corresponds to $\mu^2 \sim 2.8$ GeV^2 at the Tevatron and ~ 3.4 GeV^2 at the LHC. Not only would this introduce an energy dependence in μ^2, but the values imply a different μ^2 for semi-hard partonic interactions than that derived from the measured elastic slope parameter, a point that we will return to below.

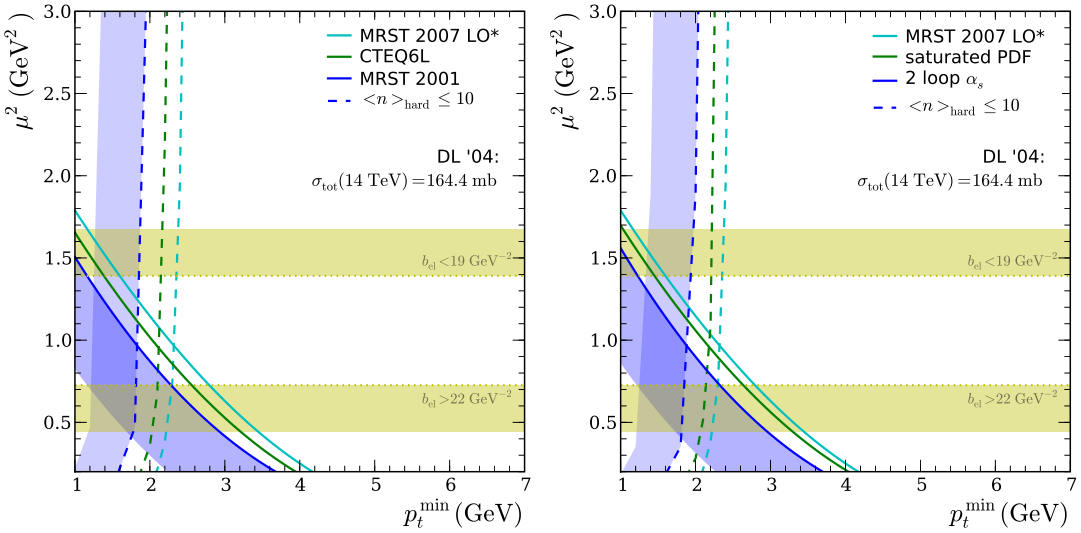

Figure 6.8: The plots show the parameter space of the eikonal model and three constraints assuming a total cross section behaviour as predicted in [7]. The first one drawn as solid curve imposes a minimum allowed value of μ^2, for a given value of $p_t^{\min}$ by requiring a positive value of $\sigma_{\text{soft}}^{\text{inc}}$. The second one, in dashed lines is deduced from an upper limit of the average number of additional semi-hard scatters in a typical minimum bias event. The excluded regions are shaded. The third constraint comes from the expected range of values for the elastic slope $b_{\text{el}} \in [19 - 22]$ GeV^{-2}. The left column shows the PDF uncertainty by varying the PDF set. The right column shows the uncertainty that is implied by using 2-loop α_s running and using the saturation modifications.

Note that both these sources of energy dependence would act in the right direction to evade the potential consistency constraints at the LHC. Allowing $p_t^{\min}$ and/or μ^2 to increase with energy would move the model towards the allowed region in Figs. 6.6-6.8.

The CDF collaboration have published measurements of the double-parton scattering cross section[108, 153]. As pointed out in Chap. 5, the quantity called σ_{eff} there is not the effective cross section as it is usually defined,

$$\sigma_{\text{eff}} = \frac{1}{\int d^2\mathbf{b}\big(A(b)\big)^2}, \tag{6.19}$$

but is related to the latter by a small correction. Using the value of this correction

estimated in Ref. [123], we obtain $\sigma_{\rm eff} \sim 11.5 \pm 2$ mb. In our form factor model, this corresponds to $\mu^2 \sim 3.0 \pm 0.5$ GeV^2. It is interesting to note that this value is close to the one predicted by the analysis of Refs. [151, 152] mentioned earlier. Again, this value is inconsistent with the assumption that the semi-hard scatters "see" a form factor matter distribution derived from the elastic slope parameter. Recall from our earlier discussion that we do not expect significant qualitative differences for other models of the matter distribution in the proton, merely some distortions of the parameter-space plane.

Improved analyses of these and other observables are under way and, once completed, in particular with a simulation of the final-state of $\sigma_{\rm soft}^{\rm inc}$, will provide strong constraints on the values of the parameters μ^2 and $p_t^{\rm min}$ in our model.

6.4.3 Conclusions

The connections between our underlying event model and the total proton-proton cross section have been discussed. Requiring consistency of the model up to LHC energies imposes constraints on the allowed parameter values, for a given range of possible measurements of $\sigma_{\rm tot}$ at the LHC. Our main result is summarised in Figs. 6.6-6.8, which show these constraints for various values of the total cross section at the LHC and various inputs to the perturbative cross section calculation. Taking the Tevatron data together with the wide range of possible values of $\sigma_{\rm tot}$ considered at LHC, no allowed set of constant parameters (μ^2, $p_t^{\rm min}$) remains for our simple model.

This would imply that soft and semi-hard scatters see different matter distributions as a function of impact parameter and/or that the parameters of our model are energy dependent. The measurement of double-parton scattering at the Tevatron supports the idea that hard scatters see a more dense matter distribution than is implied by the t-slope of the elastic cross section. Various phenomenological models also predict such effects. We will therefore study this possibility in the next Chapter as well as describing the Monte Carlo implementation of such a model.

Chapter 7

Hot Spot Model

"In God we trust, all others bring data."
— Dr. W. Edwards Deming 1900-1993, American Statistician

We have seen in the last sections that the measurements of the elastic t-slope reveal our initial assumption of identical matter overlaps for both hard and soft scatters eventually as being too simple. The idea of different matter distributions for hard and soft scatters is furthermore supported by several models and indicated by the measurement of the double parton scattering cross section. We therefore relax this condition and go back to the initial form of the soft eikonal function from Eq. (6.14), with $A_{\text{soft}}(b) \neq A(b)$. For simplicity we choose the same functional form but use a new free parameter, μ^2_{soft}, to describe its shape. The strongest constraints came from the measurements of the elastic t-slope so the main idea of this improved model now is to fix this additional parameter by requiring the elastic t-slope to be correctly described. The details are slightly more complicated because we still have to fix $\sigma^{\text{inc}}_{\text{soft}}$. Since we have two unknowns, $\sigma^{\text{inc}}_{\text{soft}}$ and μ^2_{soft}, and two additional constraints, t-slope and σ_{tot}, we can aim to solve this system for any given parameter set (p_t^{min}, μ^2, CM energy, PDFs, etc.).

7.1 Details

Our goal, to describe interactions over the entire p_t spectrum, can be achieved by using $\chi_{\mathrm{QCD}}(\mathbf{b}, s)$ for interactions with $p_t > p_t^{\min}$ and $\chi_{\mathrm{soft}}(\mathbf{b}, s)$ for interactions with 0 GeV $< p_t < p_t^{\min}$. With this procedure we become to some extent independent of $p_t^{\min}$, as it doesn't control the amount of additional activity but rather its decomposition in hard and soft scatters. $\chi_{\mathrm{tot}}(\mathbf{b}, s)$ reads now

$$\begin{aligned}\chi_{\mathrm{tot}}(\mathbf{b}, s) =& \chi_{\mathrm{QCD}}(\mathbf{b}, s) + \chi_{\mathrm{soft}}(\mathbf{b}, s) \\ =& \frac{1}{2}\left[A(\mathbf{b}; \mu^2)\ \sigma_{\mathrm{hard}}^{\mathrm{inc}}(s; p_t^{\min}) + A_{\mathrm{soft}}(\mathbf{b}; \mu_{\mathrm{soft}}^2)\ \sigma_{\mathrm{soft}}^{\mathrm{inc}}\right] ,\end{aligned} \tag{7.1}$$

where the two additional free parameters compared to the model of QCD-like additional scatters, μ_{soft}^2 and $\sigma_{\mathrm{soft}}^{\mathrm{inc}}$, are fixed by solving Eqs. (6.8) and (6.10) respectively,

$$\begin{aligned}\sigma_{\mathrm{tot}}(s) &= 2\int \mathrm{d}^2\mathbf{b}\ \ \left[1 - \ e^{-\chi_{\mathrm{tot}}(\mathbf{b},s)}\right] , \\ b_{\mathrm{el}}(s) &= \frac{1}{\sigma_{\mathrm{tot}}}\int \mathrm{d}^2\mathbf{b}\ b^2\ \left[1 - \ e^{-\chi_{\mathrm{tot}}(\mathbf{b},s)}\right] .\end{aligned} \tag{7.2}$$

The left-hand-side of both equations is evaluated using one of the parameterisations discussed in Sect. 6.2. They describe all available data below 1.8 TeV and give a sensible range of possible measurements at e.g. LHC energies. This leaves then the same parameter space as before, since all free parameters in the *soft sector* are fixed by external constraints.

With the full eikonal from Eq. (7.1), we can construct our model for additional scatters, by imposing the additional assumptions,

- The probability distributions of semi-hard and soft scatters are independent
- Soft scatters are uncorrelated and therefore obey Poissonian statistics

The probability $\mathcal{P}_{h,n}(\mathbf{b}, s)$, for having exactly h semi-hard and n soft scatters at impact parameter $\mathbf{b}$ and centre-of-mass energy s is then given by,

$$\mathcal{P}_{h,n}(\mathbf{b}, s) = \frac{(2\chi_{\mathrm{QCD}}(\mathbf{b}, s))^h}{h!}\ \frac{(2\chi_{\mathrm{soft}}(\mathbf{b}, s))^n}{n!}\ e^{-2\chi_{\mathrm{tot}}(\mathbf{b},s)} . \tag{7.3}$$

From Eq. (7.3) we can now deduce the cross section for having exactly h semi-hard and n soft scatters as,

$$\sigma_{h,n}(s) = \int \mathrm{d}^2\mathbf{b}\ \mathcal{P}_{h,n}(\mathbf{b}, s)\,. \tag{7.4}$$

The cross section for an inelastic collision (either semi-hard or soft), is obtained by summing over the appropriate multiplicities and yields

$$\begin{aligned}\sigma_{\mathrm{inel}}(s) &= \int \mathrm{d}^2\mathbf{b} \sum_{h+n\geq 1} \mathcal{P}_{h,n}(\mathbf{b}, s) \\ &= \int \mathrm{d}^2\mathbf{b}\ \left[1 - e^{-\chi_{\mathrm{tot}}(\mathbf{b},s)}\right]\,.\end{aligned} \tag{7.5}$$

The inelastic cross section for at least one semi-hard scattering is

$$\begin{aligned}\sigma_{\mathrm{inel}}^{\mathrm{semi-hard}}(s) &= \int \mathrm{d}^2\mathbf{b} \sum_{h\geq 1,n\geq 0} \mathcal{P}_{h,n}(\mathbf{b}, s) \\ &= \int \mathrm{d}^2\mathbf{b}\ \left[1 - e^{-\chi_{\mathrm{QCD}}(\mathbf{b},s)}\right]\,.\end{aligned} \tag{7.6}$$

With the cross sections from Eqs. (7.4) and (7.5) we can construct the basis of our multiple soft and semi-hard scattering model, the probability, $P_{h,n}$, of having exactly h semi-hard and n soft scatters in an inelastic event ($h+n \geq 1$). It is given by

$$P_{h,n}(s) = \frac{\sigma_{h,n}(s)}{\sigma_{\mathrm{inel}}(s)} = \frac{\int \mathrm{d}^2\mathbf{b}\ \mathcal{P}_{h,n}(\mathbf{b}, s)}{\int \mathrm{d}^2\mathbf{b}\ \left[1 - e^{-\chi_{\mathrm{tot}}(\mathbf{b},s)}\right]}\,, \quad h+n \geq 1\,, \tag{7.7}$$

which is analogous to Eq.(4.14) for the case of solely semi-hard additional scatterings. Equation (7.7) defines a matrix of probabilities for individual multiplicities. This matrix is evaluated at the beginning of each run and the corresponding multiplicities are drawn for each event from this matrix according to their probability.

Presence of a different scattering type

Equation (7.7) leads to very inefficient generation of additional scatters in cases where a rare hard scattering, with cross section σ_{rare}, takes place. Equation (4.17)

has been deduced for this case, by exploiting the independence of different scatters. The presence of soft scatters doesn't alter that result as our assumption is that the soft scatters are independent from each other and from the other scatterings. Hence, the probability for h hard scatters (from which one is distinct, *i.e.* $h = m+1$) and n soft scatters is given by

$$P_{h=m+1,n}(s) = \frac{\int \mathrm{d}^2\mathbf{b}\ \mathcal{P}_{m,n}(\mathbf{b},s)\ \frac{(A(b)\sigma_{\mathrm{rare}})^1}{1!}\ e^{-A(b)\sigma_{\mathrm{rare}}}}{\int \mathrm{d}^2\mathbf{b}\ A(b)\sigma_{\mathrm{rare}}} \tag{7.8}$$

$$\approx \int \mathrm{d}^2\mathbf{b}\ \mathcal{P}_{m,n}(\mathbf{b},s)A(b) \tag{7.9}$$

$$= \frac{h}{\sigma^{\mathrm{inc}}_{\mathrm{QCD}}} \int \mathrm{d}^2\mathbf{b}\ \mathcal{P}_{h,n}(\mathbf{b},s)\,. \tag{7.10}$$

The probability for m semi-hard ($p_t \geq p_t^{\mathrm{min}}$) and n soft additional scatters is multiplied in Eq (7.8) with the probability for exactly one scattering with an inclusive cross section of σ_{rare}. The denominator is the inclusive cross section for this distinct scattering, *i.e.* summed over all multiplicities for additional semi-hard and soft scatters. By approximating the exponential with unity and exploiting the normalisation of $A(b)$ ($\int \mathrm{d}^2\mathbf{b}\ A(b) = 1$), we finally deduce Eq. (7.10).

7.1.1 Monte Carlo implementation

In this section, we will describe in detail how the additional soft scatterings are implemented. The corresponding description for the semi-hard part of the underlying event is given in Sect. 4.3.2. At the end of this section we will give a brief overview over the entire event generation with respect to the underlying event.

At large centre-of-mass energies, s, and small scale of interactions, Q^2, the parton densities suggest a proliferation of small-x gluons. That is the reason why we chose to model the soft scattering contributing to the underlying event as elastic collisions between soft gluons. We start the generation of these soft scatters after all perturbative evolution has terminated, since p_t^{min} is typically at the order of the parton shower cut-off scale. The non-perturbative remnant decays, that are described in detail in Sect. 4.3.2, produce diquarks from which the soft gluons are radiated and scatter off each other. Such a scattering is depicted in Fig. 7.1.

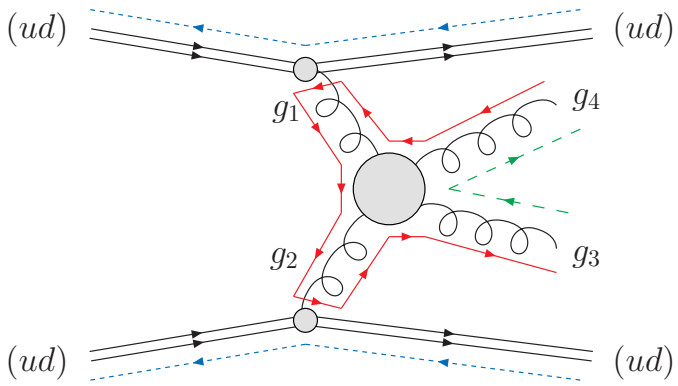

Figure 7.1: Soft gluon collision in a diquark scattering. The diquarks are in a anti-triplet state and remain unchanged with respect to their colour state. Figure 4.3.2 is the corresponding figure from Chap. 4.

All soft gluons carry colour charge and have an effective gluon mass, $m_g = 0.75$ GeV, in correspondence to the effective gluon mass that is used during parton showers and hadronisation. As simplest solution, we chose to sever the colour connections to the diquarks so that the two outgoing gluons from each soft scattering are colour connected to each other. This is motivated by a assuming a Pomeron-like structure for this soft forward interactions.

The scattering of the soft gluons can be described by the variables x_1, x_2, p_t, ϕ. x_1 and x_2 are the longitudinal momentum fractions of the two incoming gluons (g_1, g_2), so that their 4 momenta in the lab frame are,

$$p^{\mu}_{g_{1,2}} = \left(\sqrt{\frac{x^2_{1,2}\ s}{4} + m_g^2}\ ,\ 0,\ 0,\ \pm\sqrt{\frac{x^2_{1,2}\ s}{4}} \right)^T . \tag{7.11}$$

p_t and ϕ are the transverse momentum and azimuthal angle, in the CM frame, of the outgoing gluons (g_3, g_4) respectively. Their four-momenta can therefore be parameterised as,

$$p^{\mu}_{g_{3,4}} = \left(\sqrt{p_t^2 + p_z^2 + m_g^2}\ ,\ \pm p_t \cos\phi,\ \pm p_t \sin\phi,\ \pm p_z \right)^T , \tag{7.12}$$

where the longitudinal momentum, p_z, is fixed by total energy-momentum conser-

vation,

$$p_z^2 = \frac{(p_{g_1}^\mu + p_{g_2}^\mu)^2}{4} - p_t^2 - m_g^2 \,. \tag{7.13}$$

The kinematics of the soft processes are fixed by choosing values for the four parameters. x_1 and x_2 are sampled from a $f(x) = 1/x$-distribution in the range $[x_{\min}, x_{\max}]$. $x_{\min}$ is a cut-off to avoid numerical instabilities. $x_{\max}$ corresponds to the maximum available energy, that is left in the diquarks. The azimuthal angle is sampled from a uniform distribution, $\phi \in (0, 2\pi)$. The transverse momentum is the last remaining degree of freedom. By construction the transverse momentum distribution must not exceed $p_t^{\min}$, but the functional form of it is not predetermined. We use a Gaussian distribution,

$$\frac{\mathrm{d}\sigma_{\text{soft}}^{\text{inc}}}{\mathrm{d}p_t^2} = A\, e^{-\beta\, p_t^2} \;, \tag{7.14}$$

to parameterise it. To fix the free parameters A and β, we impose the following constraints:

- The resulting soft cross section has to match the total soft cross section, which has been fixed to describe σ_{tot} and b_{el} with Eqs. (6.8) and (6.10),

$$\int \mathrm{d}p_t^2 \, \frac{\mathrm{d}\sigma_{\text{soft}}^{\text{inc}}}{\mathrm{d}p_t^2} \;\overset{!}{=}\; \sigma_{\text{soft}}^{\text{inc}} \tag{7.15}$$

- The transverse momentum distribution of semi-hard and soft scatterings should be continuous at the matching scale,

$$H(s; p_t^{\min}) := \left.\frac{\mathrm{d}\sigma_{\text{hard}}^{\text{inc}}}{\mathrm{d}p_t^2}\right|_{p_t = p_t^{\min}} \;\overset{!}{=}\; \left.\frac{\mathrm{d}\sigma_{\text{soft}}^{\text{inc}}}{\mathrm{d}p_t^2}\right|_{p_t = p_t^{\min}} \;, \tag{7.16}$$

  where we introduced H as shorthand for the hard inclusive jet cross section at $p_t = p_t^{\min}$.

These conditions are fulfilled by the parameterisation,

$$\frac{\mathrm{d}\sigma_{\text{soft}}^{\text{inc}}}{\mathrm{d}p_t^2} = H(s; p_t^{\min})\, e^{-\beta(p_t^2 - p_t^{\min 2})} \;, \tag{7.17}$$

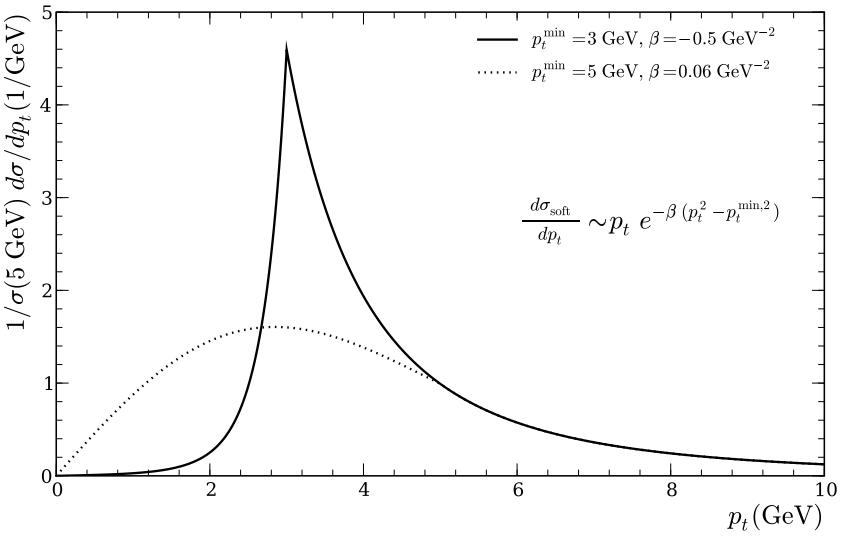

Figure 7.2: Transverse momentum distribution of additional scatters

where the slope, β, must satisfy,

$$\frac{e^{\beta {p_t^{\min}}^2} - 1}{\beta} = \frac{\sigma_{\rm soft}^{\rm inc}}{H(s; p_t^{\min})}\,. \tag{7.18}$$

Figure 7.2 shows the transverse momentum spectrum for two different cut-off values. The slope, β, is chosen such that both curves correspond to the same integrated cross section.

After the kinematics has been generated in the CM frame, we boost back to the lab frame and reshuffle the diquark momenta such, that they remain on their original mass shell. Now we can determine the available energy for the next soft interaction and iterate the process until the requested multiplicity has been reached or all available energy of the diquarks has been used.

Overview

After this detailed description of how the soft scatters are modelled, we give an overview of the event flow. During initialisation the following steps are performed:

1. Calculation and pre-sampling of the inclusive hard jet cross section above

$p_t^{\min}$ according to the standard QCD $2 \to 2$ matrix elements and the parton densities that are selected.

2. Optional calculation and pre-sampling of other hard processes that are selected for the simulation of double parton scattering events, as for example in Chap. 5.

3. Determination of the parameters for the soft eikonal, *i.e.* μ^2_{soft} and $\sigma^{\text{inc}}_{\text{soft}}$ according to Eqs. (6.8) (σ_{tot}) and (6.10) (b_{el}). If it is not possible to fulfil both constraints, the run is aborted indicating that this parameter choice is unable to reproduce sensible values for σ_{tot} and b_{el}.

4. Determination of the slope, β, for the soft gluon transverse momentum distribution. This is obtained by solving Eq. (7.18).

5. Calculation of $P_{h,n}(s)$ from Eqs. (7.7) or (7.10) respectively.

For each event we now have to go through the following list, as far as the multiple interaction model is concerned:

1. Sampling and generation of the requested additional hard scatters (for double parton scattering). Evolution of the external partons down to the hadronic scale using the parton shower algorithm.

2. Generation of additional semi-hard scatters as described in Chap. 4 according to the multiplicity distribution of $P_{h,n}(s)$ and evolution using parton showers.

3. Execution of the forced splitting algorithm as described in Sect. 4.3.2 and decay of each beam remnant to a (anti)diquark system according to their flavour content.

4. Generation of soft scatters as described above and governed by $P_{h,n}(s)$.

7.2 Parameter space

To study the features of our improved model, we try to repeat the analyses done for the case where semi-hard and soft scatters used the same matter distribution. We

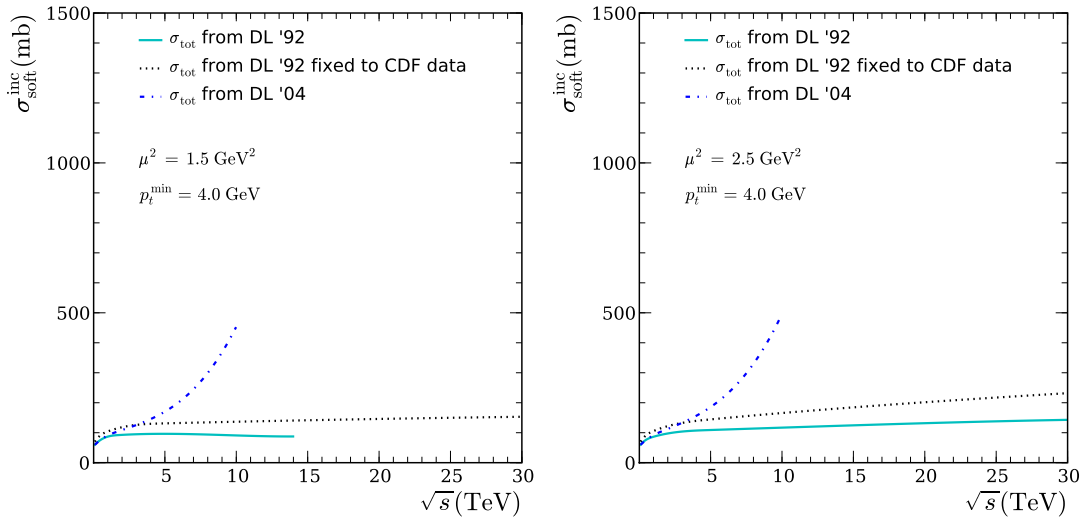

Figure 7.3: $\sigma_{\rm soft}^{\rm inc}$ for two different points in parameter space. Each of the three different curves shows the soft cross section that would appear when the respective parameterisation for the total cross section is used as input to fix $\sigma_{\rm soft}^{\rm inc}$. The y-axis range is identical to Fig. 6.4, which allows easy comparison. Curves that don't reach out to 30 TeV correspond to parameters choices that are unable to reproduce $\sigma_{\rm tot}$ and $b_{\rm el}$ correctly at these energies.

started the discussion there with the *de-eikonalised* cross section. It is not possible to define this quantity in the improved model however, since $\mu^2_{\rm soft}$ is in general different from μ^2. $\chi_{\rm tot}(\mathbf{b}, s)$ has therefore no simple relation to a cross section any more. The *de-eikonalised* cross section was defined as $\sigma_{\rm de-eik} = \sigma_{\rm soft}^{\rm inc} + \sigma_{\rm hard}^{\rm inc}$. We find it therefore illustrative to extract and discuss $\sigma_{\rm soft}^{\rm inc}$ for a fixed set of parameters as a function of the centre-of-mass energy. Figure 7.3 shows this quantity and reveals interesting features. First, it is noticeable that not all parameter combination are valid over the considered range of centre-of-mass energies. Whenever a curve is not available at a certain energy, it means that this model instance is not able to describe $\sigma_{\rm tot}$ *and* $b_{\rm el}$, from Sect. 6.2, simultaneously, *i.e.* Eq. (7.2) had no solution. In particular, the most recent Donnachie-Landshoff parameterisation from Ref. [7] is only functional up to energies of $\approx$ 10 TeV. The second feature that can be extracted from Fig. 7.3 is, that the soft cross section is more-or-less constant when going from 1-30 TeV. In the previous model (Fig. 6.4) this was extremely different and at least an undesirable feature. We used an identical y-axis range to allow

easy comparison between the two models. This behaviour is even retained when going to larger values of μ^2.

To further examine the parameter space of the model we fix the centre-of-mass energy and calculate the boundaries of the allowed parameter space in analogy to Figs. 6.5 and 6.6-6.8 respectively. We start with Tevatron energy of 1.8 TeV where we rely on the measurement of the elastic slope ($b_{\mathrm{el}} = 16.98 \pm 0.25$ GeV^{-2} [145]). Figure 7.4 incorporates this requirement along with the total cross section in the three different variants described in Sect. 6.2. It shows the remaining parameter space, where the blue curve corresponds to the CDF measurement ($\sigma_{\mathrm{tot}} = 81.8 \pm 2.3$ mb [139]). The disallowed regions are partly shaded. From Fig. 7.4 we can deduce that for values of $p_t^{\mathrm{min}} > 3$ GeV essentially no restriction with respect to μ^2 remains (except for $\mu^2 > 0.5$ GeV^2, which is within the usually considered region). The differences between the curves at low p_t^{min} are due to the different total cross sections they describe. DL '92 assumes the smallest total cross section, whereas the CDF measurement is the largest one.

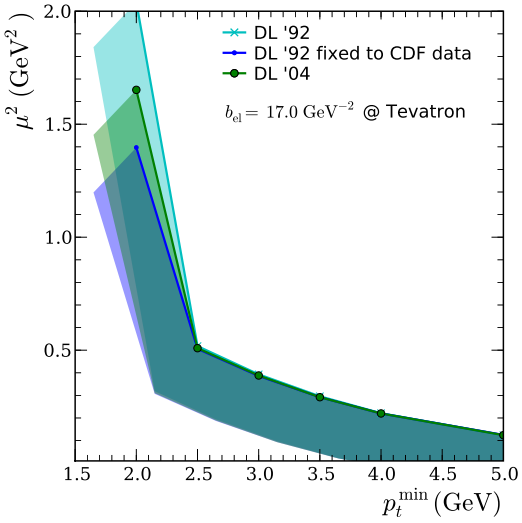

Figure 7.4: Parameter space of the improved eikonal model at 1.8 TeV. The solid curves impose a minimum allowed value of μ^2, for a given value of p_t^{min} by requiring a valid description of σ_{tot} and b_{el}. The excluded regions are shaded.

The next point in energy we consider is of course the nominal LHC energy, 14 TeV, and the corresponding constraints are shown in Fig. 7.5. The total cross section parameterisation from Ref. [7] is omitted there, because no valid parameter configuration could be found. We have seen that already in Fig. 7.3, where 10 TeV was the upper limit of validity. This problem is due to the very steeply rising total cross section that requires also a strongly rising soft cross section component. However, since the slope parameter remains at its values from the old extrapolation

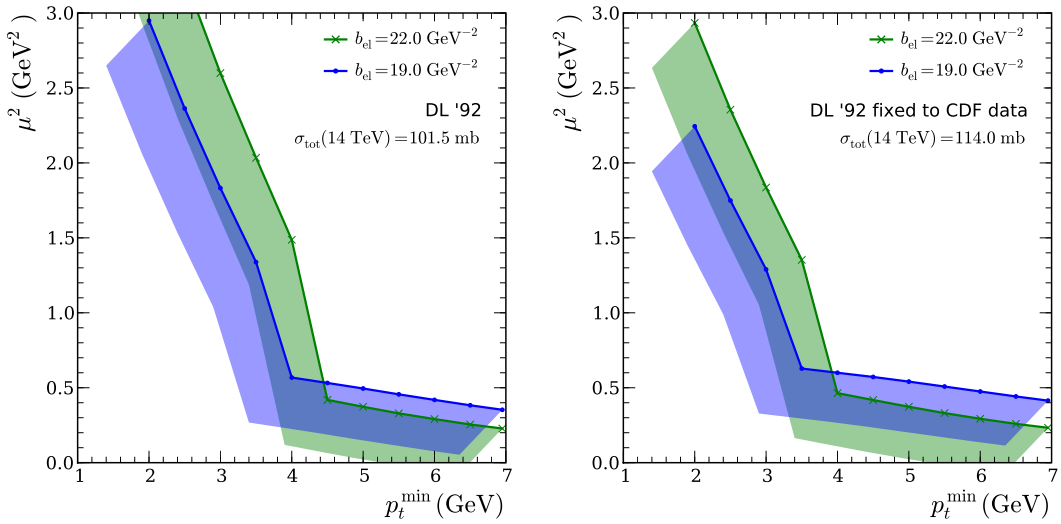

Figure 7.5: The plots show the parameter space of the eikonal model assuming a total cross section behaviour as predicted in Ref. [6] (left) and (right). The solid curves impose a minimum allowed value of μ^2, for a given value of $p_t^{\min}$ by requiring a valid description of σ_{tot} and b_{el}. The excluded regions are shaded. The two different curves correspond to the boundaries of the expected elastic slope measurements at LHC ($b_{\text{el}} \in [19-22]$ GeV^{-2}). We used the MRST 2001 LO[114] PDFs for these plots.

the two constraints cannot be fulfilled at high energies. In general, Ref. [7] predicts a cross section that is $\sim 40\%$ larger than any of the predictions from Refs. [6, 140–143] and therefore we do not draw any conclusion until the total and elastic cross sections have been measured at LHC.

At LHC energies we see that the region, where essentially no restrictions to μ^2 are active moves towards larger values of $p_t^{\min}$, *i.e.* above ~ 4 GeV, compared to Tevatron. Below we need significantly larger values of μ^2. For $\mu^2 \sim 3$ GeV^2, which is implied by CDFs double parton scattering measurement, all values of $p_t^{\min} > 3$ GeV are allowed.

7.3 Results

We have determined the general shape of the allowed parameter space for Tevatron and LHC in the previous section. In this section we simulate events and infer from the resulting final-states on the goodness of fit for individual parameter configurations in this allowed region.

7.3.1 Tevatron

We start by comparing the simulation to existing data from the Tevatron and use the analysis described in Sect. 4.2.1 for that purpose. In contrast to Chap. 4, we can now make use of all available data, *i.e.* the Jet20 *and* MinBias sample. Figure 7.6 displays the χ^2 values of describing this data as colour code in our two-dimensional parameter space. We show the contour plots for all six observables in the left plot and for the observables solely from the transverse region in the right plot. We have used the MRST 2001 LO[114] PDFs built in to Herwig++. Because we almost doubled the data points to which we compare, the overall χ^2 increased. Nevertheless, the optimum still gives a good description of the data and exhibits a value of $\chi^2/N_{\text{dof}} < 3.0$. One has to keep in mind that these two parameters are the only variables in this fit, where all other parameters are fixed by LEP-, B-factory and Tevatron data. The white areas in Fig. 7.6 are the ones predicted in Fig. 7.4 for disallowed regions. We could identify clearly a best-fit region which lies within $p_t^{\min} \in (3.5, 4.5)$ and $\mu^2 \in (1.2, 1.8)$. This region is also confirmed by the χ^2-contour for the transverse observables, although generally larger values of $\mu^2$are preferred there.

To find the optimal parameter choice we extracted the χ^2-profile along the μ^2-axis, *i.e.* for fixed values of $p_t^{\min}$. These profiles are displayed in Fig. 7.7 again for all observables and only for the transverse ones. Crosses indicate the simulated parameter configurations. The curves are quadratic fits to these points and the legend indicates the minimum of each parabola, calculated using the fit coefficients. From that we extract our final tune, which consists of the values,

$$p_t^{\min} = 4 \text{ GeV} \qquad \text{and} \qquad \mu^2 = 1.5 \text{ GeV}^2 \,. \tag{7.19}$$

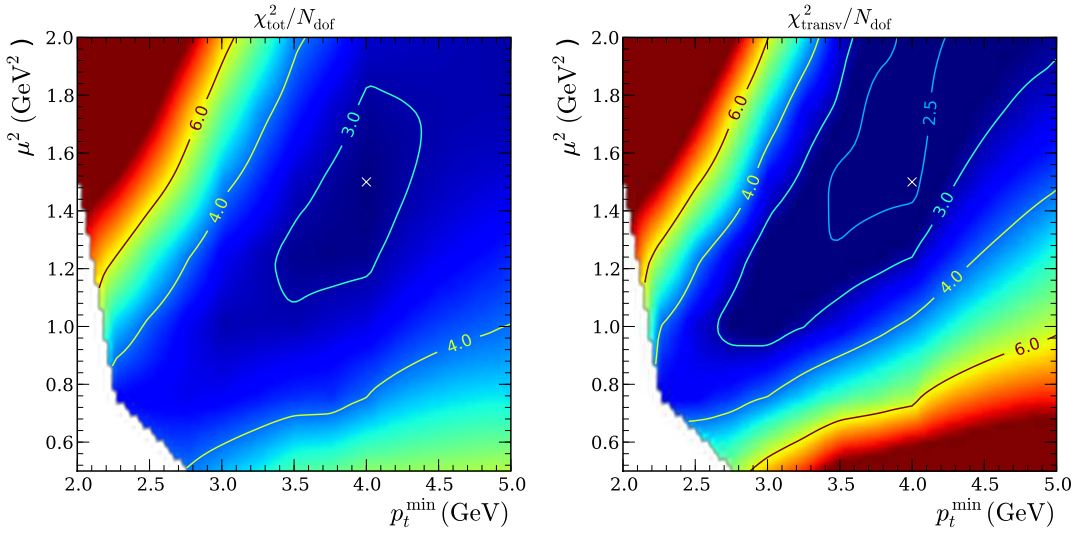

Figure 7.6: Contour plots for the χ^2 per degree of freedom of all discussed observables (left) and only the ones from the transverse region (right). The cross indicates the location of our preferred tune and the white area consist of parameter choices where the elastic t-slope and the total cross section cannot be reproduced simultaneously. For this scan we used all available bins

It is indicated in Fig. 7.6 by the white cross. If we compare Fig. 7.7 with Fig. 4.6, we see that the sensitivity on the transverse momentum cut-off is clearly reduced. In the old model, the optimal parameter choices for μ^2 varied in the range 0.9–2.4, whereas in the new model the range is reduced to 1.0–1.5. In both cases, the μ^2 range is extracted for a variation of p_t^{min} (p_t^{min}) in the range 3-4 GeV. The absolute χ^2 is larger in the new model, but this is due to the additional data points we included for the fit.

Figures 7.8, 7.9 and 7.10 show the final-state result for the transverse, towards and away region respectively. The plots compare 3 points in parameter space including our final tune. The subplot below each main plot shows the ratio of the simulation to the data and indicates the error on the data points as yellow band.

Although we are happy with the overall description of the data, we clearly see a systematic deviation for the first bins in each observable. Our simulation tends to overshoot the data there for both the multiplicities and the transverse momentum sums. Since this seems to be independent of our parameter choice, we repeated

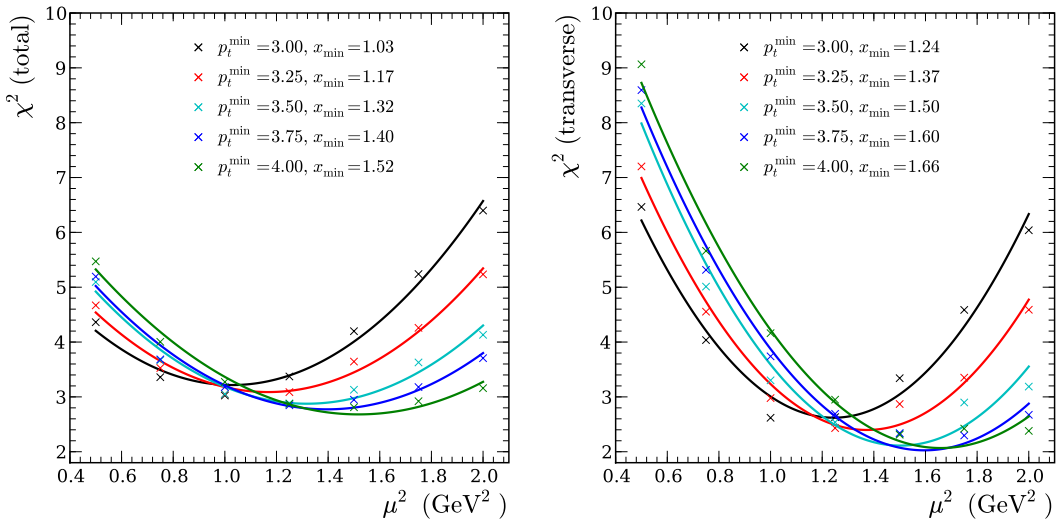

Figure 7.7: Line scans at fixed values of $p_t^{\min}$ of all discussed observables (left) and only the ones from the transverse region (right). The curves show a quadratic fit for each dataset. $x_{\min}$ is the position of the minimum calculated using the fit parameters. For this scan we used all available bins

the χ^2-contour plots for the case where we neglect the first 4 bins. The result is shown in Fig. 7.11 and shows that we are not biased towards a completely different χ^2-map. We attribute this behaviour to the missing implementation of diffractive events within our model. Our inelastic cross section implicitly contains these events and e.g. double diffraction would lead to event topologies that would be triggered but won't give any activity in any region. All observables are averaged quantities so that this effect could very well move the average in the first bins into the right direction.

Another slight discrepancy is present in the $\langle p_t^{\text{sum}} \rangle$-observable for the transverse region. The data reaches a plateau for $p_t^{\text{ljet}} \gtrsim 10$ GeV, whereas our simulation does for $p_t^{\text{ljet}} \gtrsim 20$ GeV. At the same time, the particle flow is well described, which means that the particles there are too soft.

We see that in the towards region, which is dominated by the primary jet, Herwig++ overshoots the data systematically. This has already been described in Chap. 4 and is due to the fact, that Herwig++ without MPI is already close to the data, leaving very little room for additional activity. Almost any model of the

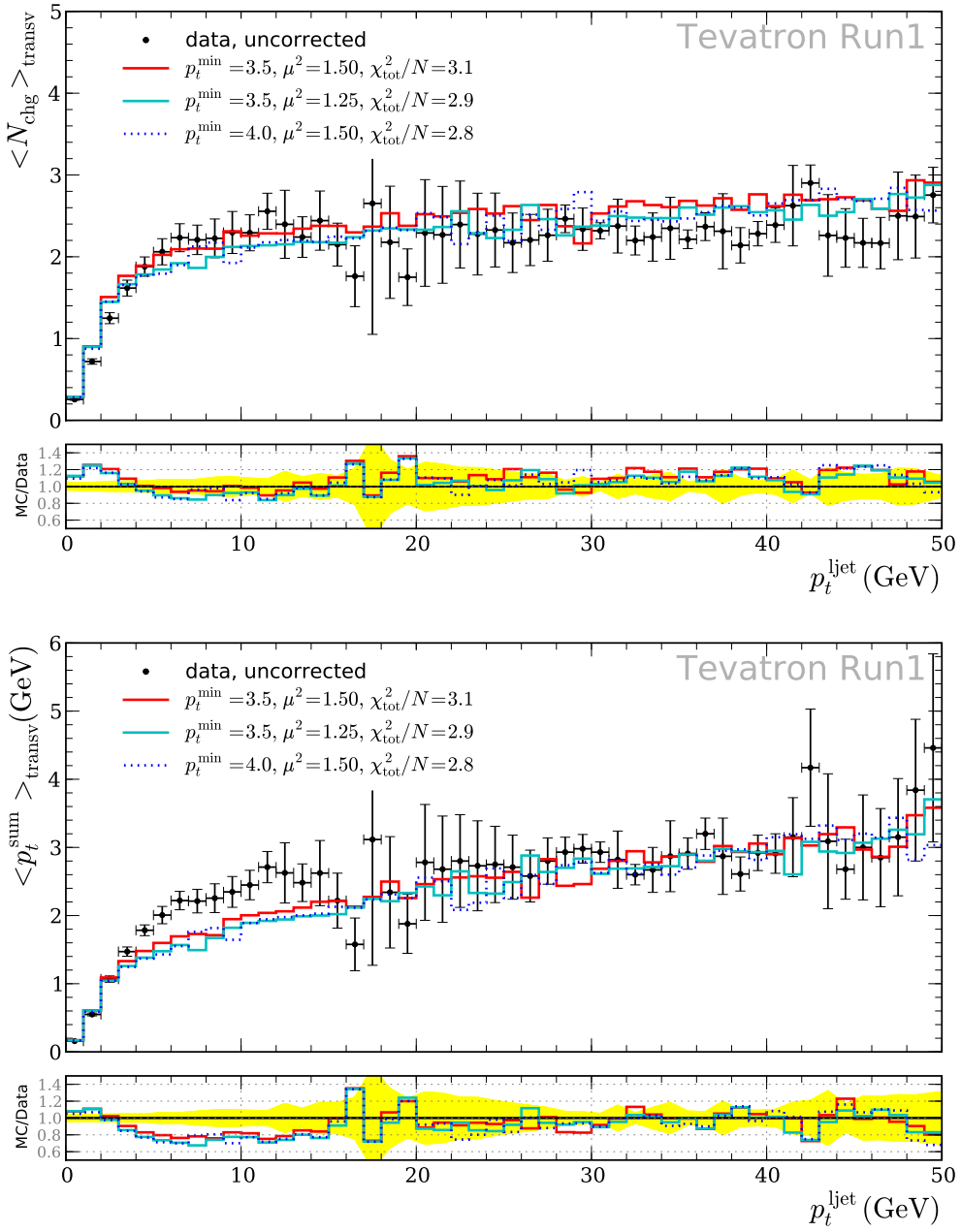

Figure 7.8: Multiplicity and $p_t^{\rm sum}$ in the **transverse** region. CDF data are shown as black circles. The histograms show Herwig++ with the improved model for semi-hard and soft additional scatters using the MRST 2001 LO [114] PDFs for three different parameter sets. The lower plot shows the ratio Monte Carlo to data and the data error band. The legend on the upper plot shows the total χ^2 for all observables.

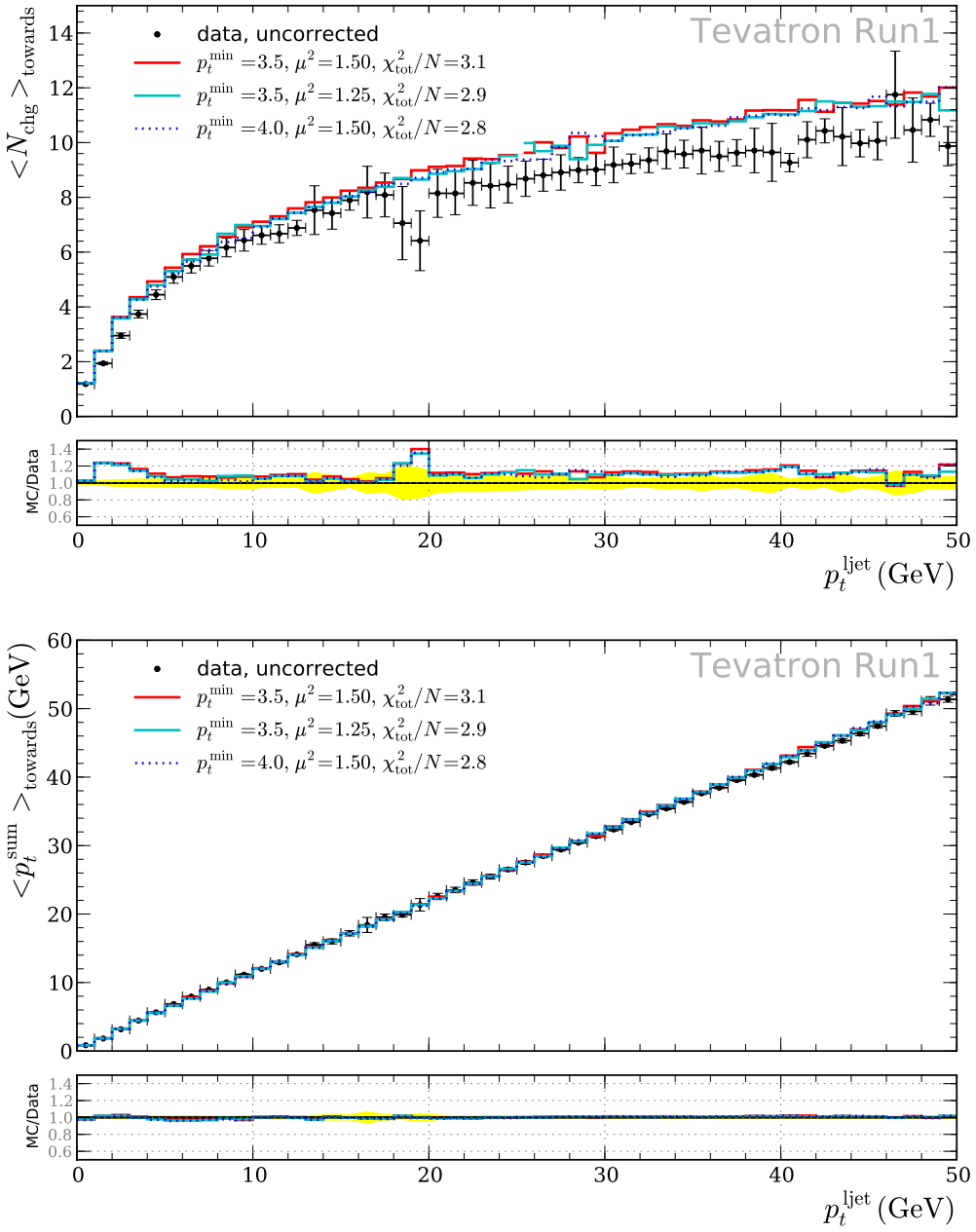

Figure 7.9: Multiplicity and $p_t^{\rm sum}$ in the **towards** region. CDF data are shown as black circles. The histograms show Herwig++ with the improved model for semi-hard and soft additional scatters using the MRST 2001 LO [114] PDFs for three different parameter sets. The lower plot shows the ratio Monte Carlo to data and the data error band. The legend on the upper plot shows the total χ^2 for all observables.

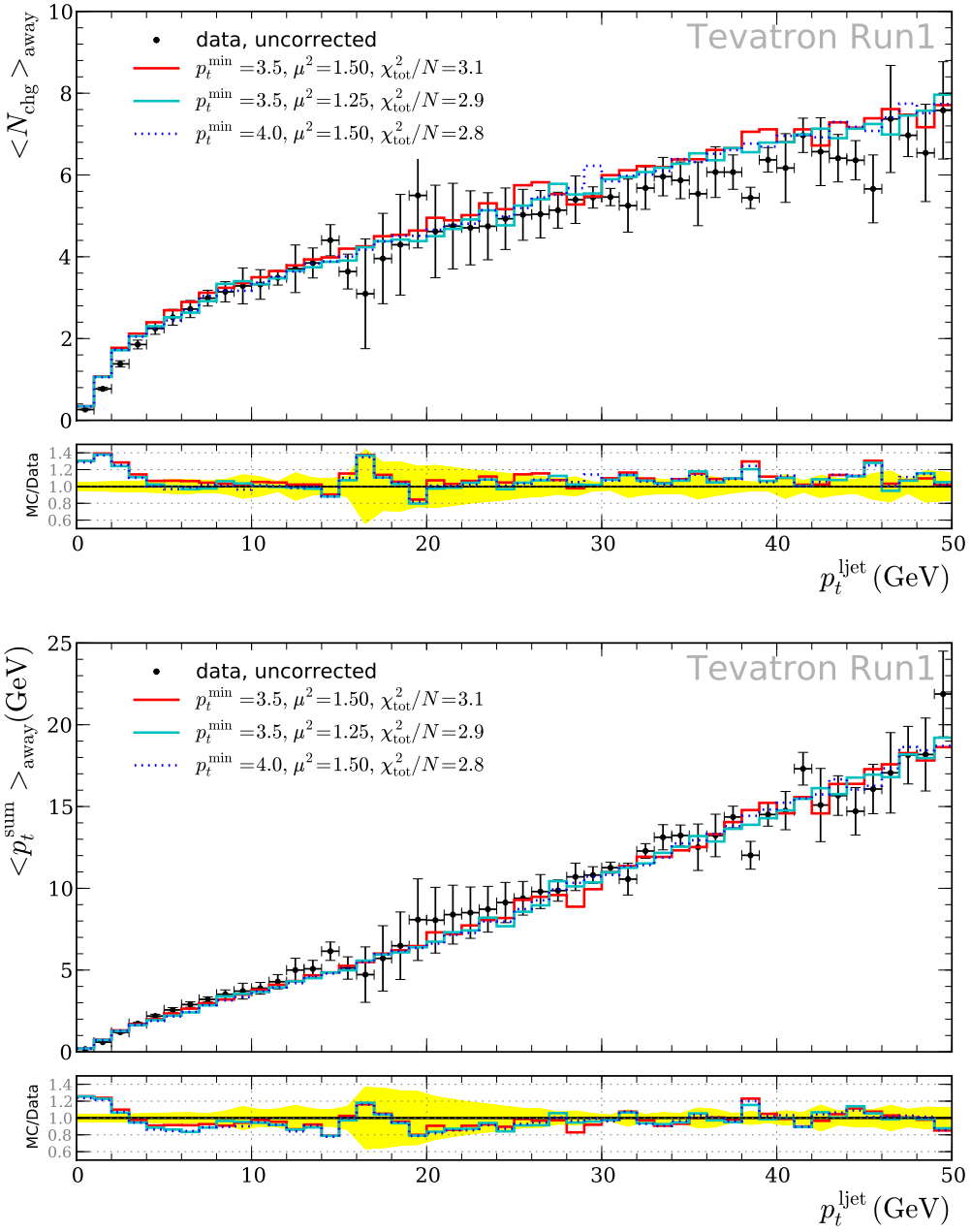

Figure 7.10: Multiplicity and $p_t^{\rm sum}$ in the **away** region. CDF data are shown as black circles. The histograms show Herwig++ with the improved model for semi-hard and soft additional scatters using the MRST 2001 LO [114] PDFs for three different parameter sets. The lower plot shows the ratio Monte Carlo to data and the data error band. The legend on the upper plot shows the total χ^2 for all observables.

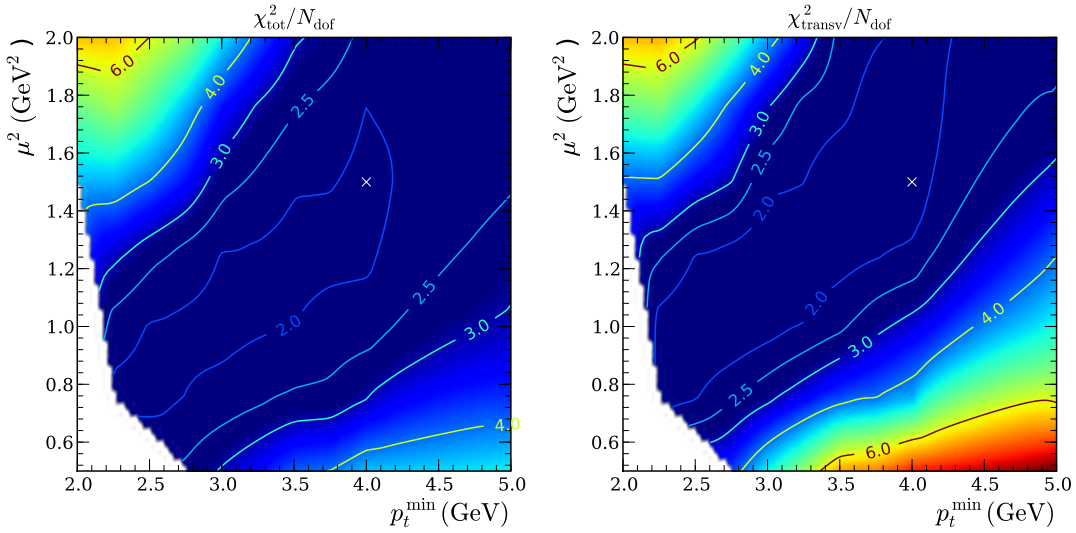

Figure 7.11: Contour plots for the χ^2 per degree of freedom of all discussed observables (left) and only the ones from the transverse region (right). The cross indicates the location of our preferred tune and the white area consist of parameter choices where the elastic t-slope and the total cross section cannot be reproduced simultaneously. For this scan we left out the first 4 bins to gain insight in the question whether the first bins bias the tune.

underlying event will produce more than enough multiplicity here and overshoot the data. In the process of χ^2 minimisation, there is therefore a slight pressure to suppress the underlying event. Nevertheless we see that compared to the results from Chap. 4 the imbalance between particle- and energy-flow is significantly reduced. This is most visible the away region.

7.3.2 LHC

Our discussion of the final-state simulation using the improved model will be completed by showing extrapolations to the LHC using the best fit point at the Tevatron. We start with the observables from Fig. 7.12, where the left plot shows the KNO distribution[117]. The right plot shows the mean charged multiplicity as a function of pseudorapidity, η. In comparison to Fig. 4.11, which displays these observables for the model without the soft component, we see an increase

$(\boldsymbol{p_t^{\min}}, \mu^2)$	$\langle N_{\rm chg}\rangle^{\rm transv}$	$\langle p_t^{\rm sum}\rangle^{\rm transv}$(GeV)
(3.0, 1.5)	5.2	4.5
(4.0, 1.5)	5.7	5.1
(5.0, 1.5)	4.3	3.9
$(p_t^{\min}, \boldsymbol{\mu^2})$		
(4.0, 1.0)	4.9	4.4
(4.0, 1.5)	5.7	5.1
(4.0, 2.0)	6.2	5.4

Table 7.1: LHC expectations for $\langle N_{\rm chg}\rangle$ and $\langle p_t^{\rm sum}\rangle$ in the transverse region for $p_t^{\rm ljet}$/ GeV $\in (10, 20)$. The values are obtained from varying our Tevatron best fit along the $p_t^{\min}$- and μ^2- axes respectively.

of ~ 0.5 particles per unit rapidity in the central region. Especially at Tevatron energies this might be counter-intuitive, since both models are tuned to the same data. However, for these plots we don't impose any cut on the charged particle transverse momentum, whereas the CDF analysis has a lower cut of 0.5 GeV. The increase we see is therefore due to additional soft particles, which we expect to appear once we include a model for soft interactions.

Finally we show the benchmark observables from Fig. 4.12 simulated with the improved model in Fig. 7.13. They show the average multiplicity (left) and average $p_t^{\rm sum}$ (right) for the transverse region. Our new LHC expectation is very close to the old one with minor increase in activity. Due to this stabilisation we are confident that the uncertainties in the LHC extrapolation are significantly reduced.

We try to give an estimate on possible LHC measurements by varying our best parameter choice along the $p_t^{\min}$- and μ^2- axes respectively. We want to emphasise that the varied parameters do not necessarily give a good fit for the Tevatron data. But since the possibility of energy dependent parameters is not ruled out, they give the range of possible final-states at LHC. The resulting values of $\langle N_{\rm chg}\rangle^{\rm transv}$ and $\langle p_t^{\rm sum}\rangle^{\rm transv}$ are shown in Table 7.1.

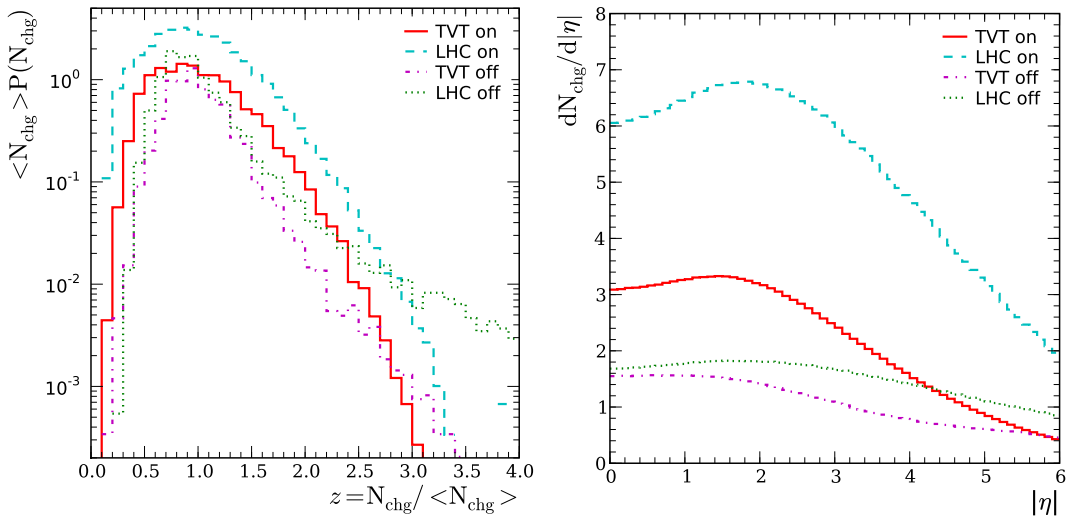

Figure 7.12: KNO plot (left) and differential multiplicity distribution (right) for Tevatron and LHC runs in the improved model. The different data sets are (from bottom to top): Tevatron with MPI off, LHC with MPI off, Tevatron with MPI on and LHC with MPI on.

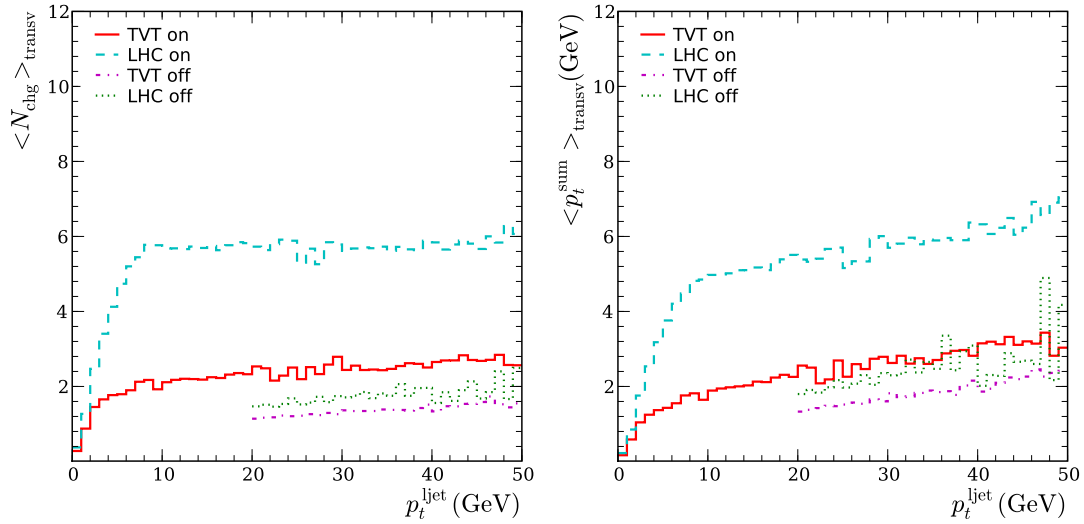

Figure 7.13: Multiplicity and p_t^{sum} in the transverse region for LHC runs with Herwig++. The different data sets are (from bottom to top): Tevatron with MPI off, LHC with MPI off, Tevatron with MPI on and LHC with MPI on.

7.4 Conclusions

We have studied an eikonal model to describe semi-hard and soft additional scatterings. We used the value of the total hadronic cross section to fix additional free parameters of the soft sector. Its initial formulation, discussed in the last Chapter, with identical matter distributions seen by these two components, appeared to have deficiencies in describing the elastic t-slope over a large range of centre-of-mass energies. We therefore implemented and studied a model, where the semi-hard scatters probe a different matter distribution than the soft ones. We tuned this model to CDF data and found a good overall description with fitting only two free parameters. Furthermore we studied the details of this improved model for several centre-of-mass energies and derived the allowed parameter space, for a given range of possible LHC measurements. We have seen that the resulting soft cross section stabilises with respect to the simpler model and remains almost constant when going from 1-30 TeV. The biggest unknown in our analysis is the total cross section at the LHC. With even a first imprecise measurement of this cross section, we could strengthen our parameter space analysis considerably.

Chapter 8

Summary and Conclusions

Our eventual goal of providing a complete description of the final-state in minimum bias collisions and underlying events in hard hadron–hadron collisions has been attained. This code is officially available inside Herwig++, has been tested in various circumstances and approved by all members of the collaboration. In addition, we systematically studied the parameter space of the model with respect to the description of available data and applicability of the model at various centre-of-mass energies.

We started by implementing a model for semi-hard additional scatters. Before, Herwig++ had to rely on a simple parameterisation of underlying event data (UA5). With the new model, it was possible to give a good overall description of CDF data on the underlying event by only tuning its two free parameters. Predictions for LHC have been made and their uncertainties have been quantified. Additionally, the uncertainties implied by the PDFs have been addressed.

Next, we extended this model to also describe events, where several hard scatterings occur. The flexible implementation for double parton scatterings is an absolutely unique feature that is only available for Herwig++ so far. We used it to examine the same-sign di-lepton channel and compared it to the Standard Model background. We concluded that this channel may offer a very clean way to measure double parton scattering, but is negligible with respect to BSM signatures.

In Chaps. 6 and 7 we described the inclusion of soft partonic scatters, which al-

lows Herwig++, for the first time, to describe minimum bias interactions but also gives a more realistic description of the underlying event. We were lead to the conclusion, that semi-hard interactions are very likely to probe a denser matter distribution inside the proton than soft interactions. This *hot spot*-like model was then examined with respect to its applicability at various centre-of-mass energies, where it uses existing parameterisations of total and elastic cross sections to fix additional free parameters. We finally tuned it to the CDF data, where we could include additional minimum bias data points.

The form of the respective overlap functions in our model has to be determined by measurements. Chapter 5 shows a clean way to determine the overlap function of hard scatters, whereas the measurement of the elastic slope gives a handle on the soft overlap function. With steadily improving data from the Tevatron, more detailed phenomenological analyses being performed and the prospect of data from the LHC, there is a real hope that the various simplifying assumptions that go into our model will be tested to the limit and we will discover where, if anywhere, more detailed understanding of the dynamics of underlying event physics is needed.

Appendix A

Program details

A.1 Code structure

We briefly discuss the classes that are responsible for the generation of additional partonic scatters and the implementation of the models discussed in Chapters 4, 6 and 7. In addition to being the main class responsible for the administration of the shower, the ShowerHandler steers also the generation of the additional semi-hard scattering processes. It has a reference to the MPIHandler set in the input files, which is used to actually create the additional scattering processes. It invokes the parton shower on all the available scatters and connects them properly to the incoming beam particles. This includes potential re-extraction of the incoming parton if it is changed as a result of initial-state radiation. It modifies the RemnantParticles that were initially created by the PartonExtractor. A number of classes are used by the ShowerHandler to generate the additional scattering processes. Soft additional scatters are generated in the HwRemDecayer class.

MPIHandler: The MPIHandler administers the calculation of the underlying event activity. The sampling and cross section calculation of the physical processes is performed using the ProcessHandler class. Using the cross section computed inside that class, the probabilities for the individual multiplicities of additional scatters are calculated during initialization. The method MPIHandler::multiplicity() samples a number of extra scatters from that pretabulated probability distribution.

The method MPIHandler::generate() creates one subprocess according to the phase space and returns it.

ProcessHandler: The ProcessHandler class is used to sample and calculate cross sections of a physical process. This is necessary once several physical processes with independent cuts are included in the underlying event. In that case several instances of the ProcessHandler are assigned to the MPIHandler. Each instance uses the MPISampler to sample the phase space of the processes that is connected to it.

MPISampler: The MPISampler performs the phase-space sampling for the additional scatterings. It inherits from SamplerBase and implements the Auto Compensating Divide-and-Conquer phase space generator, ACDCGen.

HwRemDecayer: The HwRemDecayer is responsible for decaying the RemnantParticles to something that can be processed by the cluster hadronization, *i.e.* (anti)quarks or (anti)diquarks. This includes the forced splittings to valence quarks and gluons respectively. Also the colour connections between the additional scatters and the remnants are set here. If additional soft partonic interactions, *i.e.* the non-perturbative part of the underlying event, are enabled, they are generated inside this class after the remnants have been decayed to the (anti)diquarks.

MPIPDF: The MPIPDF class is used to modify the PDF's used for the initial state shower of additional scatters. All sorts of rescaling are possible but currently the mode that is used is the one where the valence part of the PDF is removed. The objects are instantiated inside ShowerHandler and set to the default PDF's using `void ThePEG::CascadeHandler::resetPDFs(...)`

A.1.1 Interfaces

The most important interfaces to set parameters for the above mentioned classes are described here. An exhaustive description of all interfaces is provided by our Doxygen documentation.

MPIHandler

- **SubProcessHandlers**: Vector of references to SubProcessHandler objects. The first element is reserved for the underlying event process. Additional references can be set to simulate additional hard processes in a single collision. See Sect. A.4 for details of how to use this functionality.

- **Cuts**: Vector of references to Cuts objects. The first element is used to impose the minimal p_t of the additional scatters, $p_t^{\min}$. This is one of the two main parameters of the model. The current default, obtained from a fit to Tevatron data is 4.0 GeV. See Chap. 7 for details. Additional cuts object may be defined for additional hard processes that should be simulated in the same event.

- **additionalMultiplicities**: Vector of integer values to specify the multiplicity of additional hard scattering processes in a single collision. See Sect. A.4 for an example.

- **InvRadius**: The inverse beam particle radius squared, μ^2. The current default is 1.5 GeV^2, obtained from the fit performed in Chap. 7.

- **IdenticalToUE**: An integer parameter specifying which element of the list of SubProcessHandlers in **SubProcessHandlers** is identical to the underlying event process. Zero means the the conventional hard subprocess is QCD jet production. -1 means that no process is identical. Any number > 0 means that one of the additional hard scatterings is QCD jet production, where the exact number specifies the position in the vector. The default is -1, which is appropriate as long as no QCD jet production is simulated.

- **colourDisrupt**: Real number in the range $[0, 1]$, which gives the probability for an additional semi-hard scattering to be disconnected from other subprocesses as far as the colour connections are concerned. The current default is 0.

- **softInt**: Switch to turn the inclusion of non-perturbative scatters to the underlying event model on (`Yes`) or off (`No`). The current default is `Yes`.

- **twoComp**: Switch to toggle between an independent overlap function for soft additional scatters (`Yes`) and identical ones $A_{\text{soft}}(\mathbf{b}) \equiv A(\mathbf{b})$ (`No`). If the two-component model is used, the parameters of the soft sector are automatically choosen to describe the total cross section as well as the elastic t-slope correctly.

- **DLmode**: Integer number $\in \{1, 2, 3\}$ to choose between three different parametrizations of the total cross section as a function of the centre-of-mass energy:

  1. Parametrization of Ref. [6].
  2. Parametrization of Ref. [6] but with rescaled normalization to match the central value of the measurement [139] by CDF. `Default`
  3. Parametrization of Ref. [7].

- **MeasuredTotalXSec**: Parameter to set the total cross section (in mb) explicitely. If this parameter is used, it will overwrite the parametrization selected with the previous switch. This is intended for first data on the total cross section and should be used instead of the parametrization, which may deviate substantially.

ShowerHandler

- **MPIHandler**: Reference to the MPIHandler. To switch multiple parton interactions off, this reference has to be set to `NULL`.

- **MaxTryMPI**: The maximum number of regeneration attempts for an additional semi-hard scattering that consumes more energy than the available one in the hadron remnants.

- **MaxTryDP**: The maximum number of regeneration attempts for an additional hard scattering that consumes more energy than the available one in the hadron remnants.

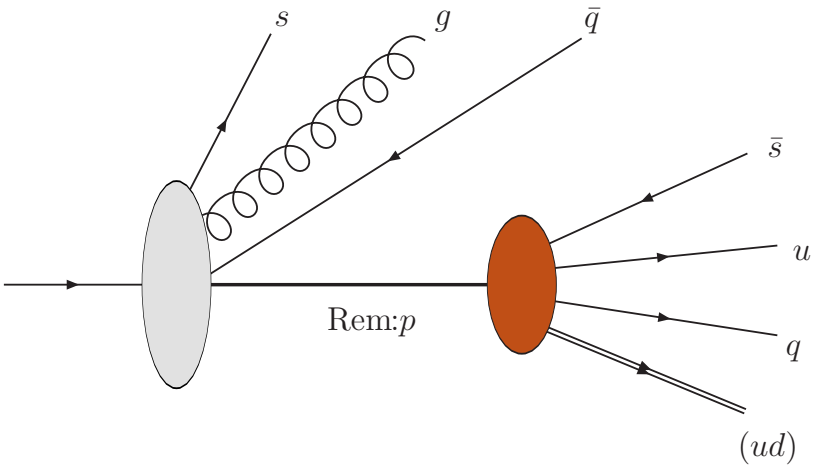

Figure A.1: The structure of the event as it is implemented in Herwig++.

A.2 Forced splitting: implementation in the event record

In Sect. 4.3 we have briefly described how the different hard scatters are correlated in colour space. This is of course an important model detail. In the event record, however, this will not be very obvious as this appears to be organised differently, in a way more closely related to the eikonal idea. In Fig. A.1 we show the same particles $(s, g, \bar{q})$ that have already been extracted from the proton in the example of Fig. 4.3.2. This time the particles that have been extracted as last particles of the parton shower are directly extracted from the proton. All additional emissions of partons that are related to the forced splitting, described in Sect. 4.3 appear as decay products of the intermediate remnant. In this way we emphasise the non-perturbative origin of these partons and draw a clear line between the perturbative parton shower model and the non-perturbative mechanism of forced splittings in the event record.

A.3 Setup for minimum bias runs

With the introduction of the new underlying event model from Herwig++ 2.3 onwards, we are able to simulate minimum bias events. However, the default setup is tailored for simulating underlying event activity in hard scattering events. We therefore have to change the setting at a few places. First, the specific minimum bias matrix element, MEMinBias, has to be selected

```
cd /Herwig/MatrixElements
insert SimpleQCD:MatrixElements[0] MEMinBias
```

Herwig++ simulates minimum bias collisions as events in which there is effectively no hard process. However, to maintain a uniform structure with the simulation of standard hard process events, we have implemented a matrix element class, MEMinBias that generates a *hard* process with as minimal an effect as possible. It extracts only light (anti)quarks (d, u, $\bar{d}$ or $\bar{u}$) from the hadrons and allows them to *scatter* through colourless exchange at zero transverse momentum, with matrix element set to unity, so that their longitudinal momentum is determined only by their parton distribution functions. To give a predominantly valence-like distribution, a cut on their longitudinal momentum fraction $x > 10^{-2}$ is recommended, as shown below. Note that because the matrix element is set to unity, the cross section that is printed to the output file at the end of the run is meaningless. The needed cuts on the process are as follows

```
##################################################
# Cuts on the hard process. MUST be ZERO for MinBias
##################################################
cd /Herwig/Cuts
set JetKtCut:MinKT 0.0*GeV
set QCDCuts:MHatMin 0.0*GeV

# Need this cut only for min bias
set QCDCuts:X1Min 0.01
set QCDCuts:X2Min 0.01
```

The remaining settings that need to be changed are the ones in the underlying event model, *i.e.* in the MPIHandler. The parameter that tells the model which hard process is identical to QCD jet production has to be set to zero as our primary hard process is QCD-like,

```
set /Herwig/UnderlyingEvent/MPIHandler:IdenticalToUE 0
```

The settings so far enable the new underlying event model with both perturbative and non-perturbative contributions. For completeness we report the switches that are available to turn the soft model off. In this case the simulation is identical to any version 2.x before 2.3.

```
set /Herwig/UnderlyingEvent/MPIHandler:softInt Yes
```

The modification that calculates the overlap function of soft scatters from the elastic t-slope data can be controlled by

```
set /Herwig/UnderlyingEvent/MPIHandler:twoComp Yes
```

A.4 Double parton scattering settings

We describe the needed settings to request explicitly a fixed number of hard interactions as done for the example in Chap. 5 To achieve that, the hard processes have to be specified along with the cuts that should be used for them. We will choose the example of like-sign W production as illustrative example.

We start with the conventional hard process and its cuts, where we select only W^+ production and decay to $e^+\nu_e$

```
cd /Herwig/MatrixElements
insert SimpleQCD:MatrixElements[0] MEqq2W2ff
# only W+
set MEqq2W2ff:Wcharge 1
# only positrons
set MEqq2W2ff:Process 3
```

To modify the cuts on that process we have to change the following

```
cd /Herwig/Cuts
set LeptonKtCut:MinKT 5.0*GeV
set LeptonKtCut:MaxEta 2.5

# inv mass cut on lepton pairs
set MassCut:MinM 0.*GeV
```

Now we can start adding additional hard processes. This is done in the MPIHandler class and always needs a SubProcessHandler that has a MatrixElement assigned and a compulsory reference to a Cuts object. This reference can be an existing one, in the case where we want to use identical cuts for the processes, but can also be an independent instance. To create such an independent instance we do

```
cd /Herwig/UnderlyingEvent/
# cut on pt. Without a specific matcher object, it works on all particles
create ThePEG::SimpleKTCut DPKtCut SimpleKTCut.so
set DPKtCut:MinKT 10
set DPKtCut:MaxEta 2.5

# create the cuts object for DP1
create ThePEG::Cuts DP1Cuts
# This should always be 2*MinKT!!
set DP1Cuts:MHatMin 20

insert DP1Cuts:OneCuts 0 DPKtCut
```

We first created an instance of the class SimpleKTCut to implement a cut on the transverse momentum and rapidity of the outgoing particles. This instance then has to be assigned to the instance of the Cuts object, `DP1Cuts`. To create a valid SubProcessHandler we have to specify

```
cd /Herwig/UnderlyingEvent/
create ThePEG::SubProcessHandler DP1
```

```
insert DP1:MatrixElements 0 /Herwig/MatrixElements/MEqq2W2ff
set DP1:PartonExtractor /Herwig/Partons/QCDExtractor
```

We have assigned the reference to the same MatrixElement instance and therefore also have W^+ production and decay to positrons. The PartonExtractor is needed to extract the partons from the beam particles but is always the reference to the `QCDExtractor`.

The last step now is to assign the subprocess and cuts instance to the MPIHandler and select the multiplicity at which they should appear. In our case this is of course simply one, but in the case of e.g. b-quark pairs or QCD dijets this may be different from one.

```
cd /Herwig/UnderlyingEvent/
# set the subprocesses and corresponding cuts
# 0 is reserved for the "usual" underlying events
# Each SubProcessHandler must be accompanied by a Cuts object!
insert MPIHandler:SubProcessHandlers 1 DP1
insert MPIHandler:Cuts 1 DP1Cuts

# now set what multiplicities you want. index = 0 means the first
# ADDITIONAL hard process

# this is SubProcessHandler 1 with multiplicity 1
insert MPIHandler:additionalMultiplicities 0 1
```

Appendix B

Systematic errors in the low p_t region

When making the initial comparison with the data from Ref. [109], we observed a $> 3\sigma$ discrepancy for the observable $p_{t,sum}^{tow}$ below 30 GeV of the leading jet. Above 30 GeV, this discrepancy is completely absent. However, we have almost no freedom to tune this observable, because it is completely dominated by the p_t of the jet itself. For the same reason, the relative error is extremely small in this region, $\sim 0.5\%$, so the absolute discrepancy is only about 2%. Nevertheless if we are going to fit to data in this region, we need to understand this effect, to avoid the χ^2 of the fit being completely dominated by it.

From Ref. [109] we find that the data sample was obtained by requiring a calorimeter tower with $E_t > 20$ GeV (including charged and neutral particles), described as the *Jet20* sample. The analysis however is based on charged particle tracks. In particular the x-axis in all observables is the scalar p_t sum of the charged particles defined to be in the hardest jet. It is clear that this sample is only unbiased for large enough values of p_t^{ljet} relative to the 20 GeV trigger. Where this happens however is not obvious. In Ref. [109] the sample was assumed to be perfectly unbiased from 20 GeV onwards. This statement is based on the good match between the *Jet20* data and the Min Bias sample around that value. Any judgement on the smoothness of the match is however limited by the statistical error on the minimum bias data, which is becoming large in the region where the two samples overlap.

region	$\sigma^0_{\rm sys}$
towards	440 MeV
away	1950 MeV
transverse	840 MeV

Table B.1: $\sigma^0_{\rm sys}$ for the three transverse momentum sum observables.

region	$\sigma^0_{\rm sys}$
towards	0.75
away	1.07
transverse	0.63

Table B.2: $\sigma^0_{\rm sys}$ for the three multiplicity observables.

Therefore we have added an additional systematic error in quadrature to the data points to reflect the precision with which we are confident they are unbiased. We choose this to have the form

$$\sigma_{add} = \frac{\sigma^0_{sys}}{10}\left(30.5 - \frac{p_t}{\rm GeV}\right) \text{ for } (20.5 < p_t/\text{ GeV} < 30.5)\ , \tag{B.1}$$

where $\sigma^0_{\rm sys}$ is extracted from the uncertainties in the bins $18-21$ GeV of the Min Bias data and the linear form ensures that the additional uncertainty goes to zero for $p_t \sim 30$ GeV. In more detail, we extract $\sigma^0_{\rm sys}$ by fitting these three bins with a linear function and use the uncertainty on the value at 20.5 GeV from this fit for $\sigma^0_{\rm sys}$ (in practice, this procedure gives only a slightly smaller error than simply averaging the errors on the three bins). The values for $\sigma^0_{\rm sys}$ that we obtained, are shown in Table B.1 and B.2 respectively.

Bibliography

[1] S. Donnachie, H. G. Dosch, O. Nachtmann, and P. Landshoff, *Pomeron physics and QCD*, *Camb. Monogr. Part. Phys. Nucl. Phys. Cosmol.* **19** (2002) 1–347.

[2] M. M. Block and R. N. Cahn, *High-Energy p anti-p and p p Forward Elastic Scattering and Total Cross-Sections*, *Rev. Mod. Phys.* **57** (1985) 563.

[3] J. R. Forshaw and D. A. Ross, *Quantum chromodynamics and the pomeron*, *Cambridge Lect. Notes Phys.* **9** (1997) 1–248.

[4] T. Regge, *Introduction to complex orbital momenta*, *Nuovo Cim.* **14** (1959) 951.

[5] G. F. Chew and S. C. Frautschi, *Regge trajectories and the principle of maximum strength for strong interactions*, *Phys. Rev. Lett.* **8** (1962) 41–44.

[6] A. Donnachie and P. V. Landshoff, *Total cross-sections*, *Phys. Lett.* **B296** (1992) 227–232, [hep-ph/9209205].

[7] A. Donnachie and P. V. Landshoff, *Does the hard Pomeron obey Regge factorisation?*, *Phys. Lett.* **B595** (2004) 393–399, [hep-ph/0402081].

[8] R. K. Ellis, W. J. Stirling, and B. R. Webber, *QCD and Collider Physics*, *Camb. Monogr. Part. Phys. Nucl. Phys. Cosmol.* **8** (1996) 1–435.

[9] **CTEQ** Collaboration, R. Brock *et. al.*, *Handbook of perturbative QCD; Version 1.1: September 1994*, . FERMILAB-PUB-94-316.

[10] G. Sterman, *QCD and jets*, hep-ph/0412013.

[11] H. Fritzsch, M. Gell-Mann, and H. Leutwyler, *Advantages of the Color Octet Gluon Picture*, *Phys. Lett.* **B47** (1973) 365–368.

[12] S. Bethke, *Determination of the QCD coupling alpha(s)*, *J. Phys.* **G26** (2000) R27, [hep-ex/0004021].

[13] D. J. Gross and F. Wilczek, *Ultraviolet behavior of non-abelian gauge theories*, *Phys. Rev. Lett.* **30** (1973) 1343–1346.

[14] H. D. Politzer, *Reliable perturbative results for strong interactions?*, *Phys. Rev. Lett.* **30** (1973) 1346–1349.

[15] G. Sterman and S. Weinberg, *Jets from Quantum Chromodynamics*, *Phys. Rev. Lett.* **39** (1977) 1436.

[16] T. Kinoshita, *Mass singularities of Feynman amplitudes*, *J. Math. Phys.* **3** (1962) 650–677.

[17] T. D. Lee and M. Nauenberg, *Degenerate Systems and Mass Singularities*, *Phys. Rev.* **133** (1964) B1549–B1562.

[18] J. D. Bjorken, *Asymptotic Sum Rules at Infinite Momentum*, *Phys. Rev.* **179** (1969) 1547–1553.

[19] J. C. Collins, D. E. Soper, and G. Sterman, *Factorization of Hard Processes in QCD*, *Adv. Ser. Direct. High Energy Phys.* **5** (1988) 1–91, [hep-ph/0409313].

[20] V. N. Gribov and L. N. Lipatov, *e+ e- pair annihilation and deep inelastic e p scattering in perturbation theory*, *Sov. J. Nucl. Phys.* **15** (1972) 675–684.

[21] G. Altarelli and G. Parisi, *Asymptotic Freedom in Parton Language*, *Nucl. Phys.* **B126** (1977) 298.

[22] Y. L. Dokshitzer, *Calculation of the Structure Functions for Deep Inelastic Scattering and e+ e- Annihilation by Perturbation Theory in Quantum Chromodynamics. (In Russian)*, *Sov. Phys. JETP* **46** (1977) 641–653.

[23] **CDF** Collaboration, F. Abe *et. al.*, *The Topology of three jet events in $\bar{p}p$ collisions at $\sqrt{s} = 1.8$ TeV*, *Phys. Rev.* **D45** (1992) 1448–1458.

[24] G. P. Salam and G. Soyez, *A practical Seedless Infrared-Safe Cone jet algorithm*, *JHEP* **05** (2007) 086, [arXiv:0704.0292].

[25] G. C. Blazey *et. al.*, *Run II jet physics*, hep-ex/0005012.

[26] **JADE** Collaboration, W. Bartel *et. al.*, *Experimental Studies on Multi-Jet Production in e+ e- Annihilation at PETRA Energies*, *Z. Phys.* **C33** (1986) 23.

[27] **JADE** Collaboration, S. Bethke *et. al.*, *Experimental Investigation of the Energy Dependence of the Strong Coupling Strength*, *Phys. Lett.* **B213** (1988) 235.

[28] S. Catani, Y. L. Dokshitzer, M. Olsson, G. Turnock, and B. R. Webber, *New clustering algorithm for multi - jet cross-sections in e+ e- annihilation*, *Phys. Lett.* **B269** (1991) 432–438.

[29] S. Catani, Y. L. Dokshitzer, M. H. Seymour, and B. R. Webber, *Longitudinally invariant K(t) clustering algorithms for hadron hadron collisions*, *Nucl. Phys.* **B406** (1993) 187–224.

[30] S. D. Ellis and D. E. Soper, *Successive combination jet algorithm for hadron collisions*, *Phys. Rev.* **D48** (1993) 3160–3166, [hep-ph/9305266].

[31] M. Cacciari and G. P. Salam, *Dispelling the N**3 myth for the k(t) jet-finder*, *Phys. Lett.* **B641** (2006) 57–61, [hep-ph/0512210].

[32] S. Gieseke, A. Ribon, M. H. Seymour, P. Stephens, and B. Webber, *Herwig++ 1.0: An Event Generator for* e^+e^- *Annihilation*, *JHEP* **02** (2004) 005, [hep-ph/0311208].

[33] S. Gieseke *et. al.*, *Herwig++ 2.0 Release Note*, hep-ph/0609306.

[34] M. Bähr *et. al.*, *Herwig++ 2.1 release note*, arXiv:0711.3137.

[35] M. Bähr *et. al.*, *Herwig++ Physics and Manual*, arXiv:0803.0883.

[36] M. Bähr *et. al.*, *Herwig++ 2.2 release note*, arXiv:0804.3053.

[37] G. Corcella *et. al.*, *HERWIG 6.5 Release Note*, hep-ph/0210213.

[38] T. Sjöstrand, S. Mrenna, and P. Skands, *PYTHIA 6.4 Physics and Manual*, *JHEP* **05** (2006) 026, [hep-ph/0603175].

[39] T. Sjöstrand, S. Mrenna, and P. Skands, *A Brief Introduction to PYTHIA 8.1*, 0710.3820.

[40] T. Gleisberg *et. al.*, *SHERPA 1α, A Proof-of-Concept Version*, *JHEP* **02** (2004) 056, [hep-ph/0311263].

[41] R. Engel, *Photoproduction within the two component dual parton model. 1. Amplitudes and cross-sections*, *Z. Phys.* **C66** (1995) 203–214.

[42] L. Lönnblad, *ARIADNE version 4: A Program for simulation of QCD cascades implementing the color dipole model*, *Comput. Phys. Commun.* **71** (1992) 15–31.

[43] G. Marchesini and B. R. Webber, *Simulation of QCD Jets including Soft Gluon Interference*, *Nucl. Phys.* **B238** (1984) 1.

[44] B. R. Webber, *A QCD Model for Jet Fragmentation including Soft Gluon Interference*, *Nucl. Phys.* **B238** (1984) 492.

[45] G. Marchesini and B. R. Webber, *Monte Carlo Simulation of General Hard Processes with Coherent QCD radiation*, *Nucl. Phys.* **B310** (1988) 461.

[46] G. Marchesini *et. al.*, *HERWIG: A Monte Carlo event generator for simulating Hadron Emission Reactions With Interfering Gluons. Version 5.1 - April 1991*, *Comput. Phys. Commun.* **67** (1992) 465–508.

[47] G. Corcella *et. al.*, *HERWIG 6: An event generator for Hadron Emission Reactions with Interfering Gluons (including supersymmetric processes)*, *JHEP* **01** (2001) 010, [hep-ph/0011363].

[48] L. Lönnblad, *ThePEG, PYTHIA7, Herwig++ and ARIADNE*, *Nucl. Instrum. Meth.* **A559** (2006) 246–248.

[49] O. Latunde-Dada, S. Gieseke, and B. Webber, *A Positive-Weight Next-to-Leading-Order Monte Carlo for e^+e- annihilation to hadrons*, *JHEP* **02** (2007) 051, [hep-ph/0612281].

[50] O. Latunde-Dada, *Herwig++ Monte Carlo at Next-to-Leading Order for e^+e^- annihilation and Lepton Pair Production*, 0708.4390.

[51] K. Hamilton, P. Richardson, and J. Tully, *A Positive-Weight Next-to-Leading Order Monte Carlo Simulation of Drell-Yan Vector Boson Production*, arXiv:0806.0290.

[52] O. Latunde-Dada, *Applying the POWHEG method to top pair production and decays at the ILC*, arXiv:0806.4560.

[53] N. Metropolis and S. Ulam, *The Monte Carlo Method*, *Journal of the American Statistical Association* **44** (1949) 335–341.

[54] M. R. Whalley, D. Bourilkov, and R. C. Group, *The Les Houches accord PDFs (LHAPDF) and LHAGLUE*, hep-ph/0508110.

[55] P. Richardson, *Spin Correlations in Monte Carlo Simulations*, *JHEP* **11** (2001) 029, [hep-ph/0110108].

[56] I. G. Knowles, *Spin Correlations in Parton-Parton Scattering*, *Nucl. Phys.* **B310** (1988) 571.

[57] I. G. Knowles, *A Linear Algorithm for Ccalculating Spin Correlations in Hadronic Collisions*, *Comput. Phys. Commun.* **58** (1990) 271–284.

[58] J. C. Collins, *Spin Correlations in Monte Carlo Event Generators*, *Nucl. Phys.* **B304** (1988) 794.

[59] M. Gigg and P. Richardson, *Simulation of Beyond Standard Model Physics in Herwig++*, *Eur. Phys. J.* **C51** (2007) 989–1008, [hep-ph/0703199].

[60] E. Boos *et. al.*, *Generic User Process Interface for Event Generators*, hep-ph/0109068.

[61] J. Alwall *et. al.*, *A Standard Format for Les Houches Event Files*, *Comput. Phys. Commun.* **176** (2007) 300–304, [hep-ph/0609017].

[62] V. V. Sudakov, *Vertex parts at very high-energies in quantum electrodynamics*, *Sov. Phys. JETP* **3** (1956) 65–71.

[63] A. Bassetto, M. Ciafaloni, G. Marchesini, and A. H. Mueller, *Jet Multiplicity and Soft Gluon Factorization*, *Nucl. Phys.* **B207** (1982) 189.

[64] A. Bassetto, M. Ciafaloni, and G. Marchesini, *Jet Structure and Infrared Sensitive Quantities in Perturbative QCD*, *Phys. Rept.* **100** (1983) 201–272.

[65] S. Catani and M. Ciafaloni, *Many Gluon Correlations and the Quark Form-Factor in QCD*, *Nucl. Phys.* **B236** (1984) 61.

[66] M. Ciafaloni, *Exponentiating Soft Emission in QCD*, *Phys. Lett.* **B95** (1980) 113.

[67] M. Ciafaloni, "Soft Gluon Contributions to Hard Processes." Lectures given at Summer Workshop on High Energy Physics, Trieste, Italy, Aug 1981.

[68] Y. L. Dokshitzer, V. A. Khoze, and S. I. Troian, *Coherence and Physics of QCD Jets*, *Adv. Ser. Direct. High Energy Phys.* **5** (1988) 241–410.

[69] A. H. Mueller, *On the Multiplicity of Hadrons in QCD Jets*, *Phys. Lett.* **B104** (1981) 161–164.

[70] B. I. Ermolaev and V. S. Fadin, *Log-Log Asymptotic Form of Exclusive Cross-Sections in Quantum Chromodynamics*, *JETP Lett.* **33** (1981) 269–272.

[71] Y. L. Dokshitzer, V. S. Fadin, and V. A. Khoze, *Coherent Effects in the Perturbative QCD Parton Jets*, *Phys. Lett.* **B115** (1982) 242–246.

[72] S. Gieseke, P. Stephens, and B. Webber, *New Formalism for QCD Parton Showers*, *JHEP* **12** (2003) 045, [hep-ph/0310083].

[73] S. Catani, S. Dittmaier, and Z. Trócsányi, *One-Loop Singular Behaviour of QCD and SUSY QCD Amplitudes with Massive Partons*, *Phys. Lett.* **B500** (2001) 149–160, [hep-ph/0011222].

[74] D. Amati and G. Veneziano, *Preconfinement as a Property of Perturbative QCD*, *Phys. Lett.* **B83** (1979) 87.

[75] D. Grellscheid and P. Richardson, *Simulation of Tau Decays in the Herwig++ Event Generator*, 0710.1951.

[76] D. Grellscheid, K. Hamilton, and P. Richardson, "Simulation of Meson Decays in the Herwig++ Event Generator." in preparation.

[77] **Particle Data Group** Collaboration, W. M. Yao *et. al.*, *Review of Particle Physics*, *J. Phys.* **G33** (2006) 1–1232.

[78] S. Jadach, Z. Wąs, R. Decker, and J. H. Kühn, *The Tau decay library TAUOLA: Version 2.4*, *Comput. Phys. Commun.* **76** (1993) 361–380.

[79] P. Golonka *et. al.*, *The TAUOLA-PHOTOS-F Environment for the TAUOLA and PHOTOS packages, release II*, hep-ph/0312240.

[80] A. L. Kagan and M. Neubert, *QCD anatomy of $B \to X_s\gamma$ Decays*, *Eur. Phys. J.* **C7** (1999) 5–27, [hep-ph/9805303].

[81] S. Catani, F. Krauss, R. Kuhn, and B. R. Webber, *QCD Matrix Elements + Parton Showers*, *JHEP* **11** (2001) 063, [hep-ph/0109231].

[82] J. Alwall *et. al.*, *Comparative study of various algorithms for the merging of parton showers and matrix elements in hadronic collisions*, *Eur. Phys. J.* **C53** (2008) 473–500, [0706.2569].

[83] **UA5** Collaboration, G. J. Alner *et. al.*, *The UA5 High-Energy $\bar{p}p$ Simulation Program*, *Nucl. Phys.* **B291** (1987) 445.

[84] T. Sjöstrand and M. van Zijl, *A Multiple Interaction Model for the Event Structure in Hadron Collisions*, *Phys. Rev.* **D36** (1987) 2019.

[85] J. M. Butterworth, J. R. Forshaw, and M. H. Seymour, *Multi-Parton Interactions in Photoproduction at HERA*, *Z. Phys.* **C72** (1996) 637–646, [hep-ph/9601371].

[86] J. M. Butterworth and M. H. Seymour, "Jimmy4 Manual." Downloadable under http://projects.hepforge.org/jimmy/.

[87] A. Capella, U. Sukhatme, C.-I. Tan, and J. Tran Thanh Van, *Jets in Small p(T) Hadronic Collisions, Universality of Quark Fragmentation, and Rising Rapidity Plateaus*, *Phys. Lett.* **B81** (1979) 68.

[88] A. Capella and J. Tran Thanh Van, *A New Parton Model Description of Soft Hadron-Nucleus Collisions*, *Phys. Lett.* **B93** (1980) 146.

[89] A. Capella and J. Tran Thanh Van, *Hadron - Nucleus Interactions and the Leading Particle Effect in a Dual Parton Model*, *Z. Phys.* **C10** (1981) 249–262.

[90] I. Borozan and M. H. Seymour, *An eikonal model for multiparticle production in hadron hadron interactions*, *JHEP* **09** (2002) 015, [hep-ph/0207283].

[91] A. Moraes, C. Buttar, and I. Dawson, *Prediction for minimum bias and the underlying event at LHC energies*, *Eur. Phys. J.* **C50** (2007) 435–466.

[92] L. Fano, *Minimum bias and underlying event at CMS*, *Acta Phys. Polon.* **B38** (2007) 435–442.

[93] D. Acosta *et. al.*, *The underlying event at the LHC*, . CERN-CMS-NOTE-2006-067.

[94] I. Borjanovic *et. al.*, *Investigation of top mass measurements with the ATLAS detector at LHC*, *Eur. Phys. J.* **C39S2** (2005) 63–90, [hep-ex/0403021].

[95] C. Hackstein, "Simulation of final states in vector boson fusion." Diploma thesis, Insitut für Theoretische Physik, Universität Karlsruhe, Nov. 2007.

[96] T. Sjöstrand and P. Z. Skands, *Multiple interactions and the structure of beam remnants*, *JHEP* **03** (2004) 053, [hep-ph/0402078].

[97] T. Sjöstrand and P. Z. Skands, *Transverse-momentum-ordered showers and interleaved multiple interactions*, *Eur. Phys. J.* **C39** (2005) 129–154, [hep-ph/0408302].

[98] S. Alekhin *et. al.*, *HERA and the LHC - A workshop on the implications of HERA for LHC physics: Proceedings Part A*, hep-ph/0601012.

[99] S. Catani, M. Ciafaloni, and F. Hautmann, *High-energy factorization and small x heavy flavor production*, *Nucl. Phys.* **B366** (1991) 135–188.

[100] J. C. Collins and R. K. Ellis, *Heavy quark production in very high-energy hadron collisions*, *Nucl. Phys.* **B360** (1991) 3–30.

[101] E. M. Levin, M. G. Ryskin, Y. M. Shabelski, and A. G. Shuvaev, *Heavy quark production in parton model and in QCD*, *Sov. J. Nucl. Phys.* **54** (1991) 867–871.

[102] S. Höche, F. Krauss, and T. Teubner, *Multijet events in the k(T)-factorisation scheme*, 0705.4577.

[103] J. Bartels, M. Salvadore, and G. P. Vacca, *AGK cutting rules and multiple scattering in hadronic collisions*, *Eur. Phys. J.* **C42** (2005) 53–71, [hep-ph/0503049].

[104] **Axial Field Spectrometer** Collaboration, T. Akesson *et. al.*, *Double parton scattering in pp collisions at* $\sqrt{S} = 63\ GeV$, *Z. Phys.* **C34** (1987) 163.

[105] J. Pumplin, *Hard underlying event correction to inclusive jet cross sections*, *Phys. Rev.* **D57** (1998) 5787–5792, [hep-ph/9708464].

[106] **CDF** Collaboration, F. Abe *et. al.*, *Study of four jet events and evidence for double parton interactions in* $p\bar{p}$ *collisions at* $\sqrt{s} = 1.8\ TeV$, *Phys. Rev.* **D47** (1993) 4857–4871.

[107] **D0** Collaboration, V. M. Abazov *et. al.*, *Multiple jet production at low transverse energies in* $p\bar{p}$ *collisions at* $\sqrt{s} = 1.8\ TeV$, *Phys. Rev.* **D67** (2003) 052001, [hep-ex/0207046].

[108] **CDF** Collaboration, F. Abe *et. al.*, *Double parton scattering in* $\bar{p}p$ *collisions at* $\sqrt{s} = 1.8\,TeV$, *Phys. Rev.* **D56** (1997) 3811–3832.

[109] **CDF** Collaboration, A. A. Affolder *et. al.*, *Charged jet evolution and the underlying event in* $p\bar{p}$ *collisions at 1.8 TeV*, *Phys. Rev.* **D65** (2002) 092002.

[110] **CDF** Collaboration, D. E. Acosta *et. al.*, *The underlying event in hard interactions at the Tevatron* $\bar{p}p$ *collider*, *Phys. Rev.* **D70** (2004) 072002, [hep-ex/0404004].

[111] K. A. Ter-Martirosyan, *On the particle multiplicity distributions at high energy*, *Phys. Lett.* **B44** (1973) 377–380.

[112] V. A. Abramovsky, V. N. Gribov, and O. V. Kancheli, *Character of inclusive spectra and fluctuations produced in inelastic processes by multi - pomeron exchange*, *Yad. Fiz.* **18** (1973) 595–616.

[113] P. Skands and D. Wicke, *Non-perturbative QCD effects and the top mass at the Tevatron*, *Eur. Phys. J.* **C52** (2007) 133–140, [hep-ph/0703081].

[114] A. D. Martin, R. G. Roberts, W. J. Stirling, and R. S. Thorne, *MRST2001: Partons and alpha(s) from precise deep inelastic scattering and Tevatron jet data*, *Eur. Phys. J.* **C23** (2002) 73–87, [hep-ph/0110215].

[115] J. Pumplin *et. al.*, *New generation of parton distributions with uncertainties from global QCD analysis*, *JHEP* **07** (2002) 012, [hep-ph/0201195].

[116] S. Gieseke, *Uncertainties of Sudakov form factors*, *JHEP* **01** (2005) 058, [hep-ph/0412342].

[117] Z. Koba, H. B. Nielsen, and P. Olesen, *Scaling of multiplicity distributions in high-energy hadron collisions*, *Nucl. Phys.* **B40** (1972) 317–334.

[118] A. Del Fabbro and D. Treleani, *Double parton scatterings in b-quark pairs production at the LHC*, *Phys. Rev.* **D66** (2002) 074012, [hep-ph/0207311].

[119] A. Del Fabbro and D. Treleani, *A double parton scattering background to Higgs boson production at the LHC*, *Phys. Rev.* **D61** (2000) 077502, [hep-ph/9911358].

[120] A. Kulesza and W. J. Stirling, *Like-sign W boson production at the LHC as a probe of double parton scattering*, *Phys. Lett.* **B475** (2000) 168–175, [hep-ph/9912232].

[121] M. Bähr, S. Gieseke, and M. H. Seymour, *Simulation of multiple partonic interactions in Herwig++*, *JHEP* **07** (2008) 076, [arXiv:0803.3633].

[122] D. Treleani, *Double parton scattering, diffraction and effective cross section*, *Phys. Rev.* **D76** (2007) 076006, [arXiv:0708.2603].

[123] M. Bähr and M. H. Seymour. in preparation.

[124] P. V. Landshoff and J. C. Polkinghorne, *Calorimeter triggers for hard collisions*, *Phys. Rev.* **D18** (1978) 3344.

[125] C. Goebel, F. Halzen, and D. M. Scott, *Double Drell-Yan annihilations in hadron collisions: Novel tests of the constituent picture*, *Phys. Rev.* **D22** (1980) 2789.

[126] N. Paver and D. Treleani, *Multi - Quark scattering and large P(T) jet production in hadronic collisions*, *Nuovo Cim.* **A70** (1982) 215.

[127] F. Halzen, P. Hoyer, and W. J. Stirling, *Evidence for multiple parton interactions from the observation of multi - muon events in Drell-Yan experiments*, *Phys. Lett.* **B188** (1987) 375–378.

[128] M. L. Mangano, *Four Jet Production at the Tevatron Collider*, *Z. Phys.* **C42** (1989) 331.

[129] R. M. Godbole, S. Gupta, and J. Lindfors, *Double parton scattering contribution to W + jets*, *Z. Phys.* **C47** (1990) 69–74.

[130] M. Drees and T. Han, *Signals for double parton scattering at the Fermilab Tevatron*, *Phys. Rev. Lett.* **77** (1996) 4142–4145, [hep-ph/9605430].

[131] **CMS** Collaboration, G. L. Bayatian *et. al.*, *CMS technical design report, volume II: Physics performance*, *J. Phys.* **G34** (2007) 995–1579.

[132] T. Stelzer and W. F. Long, *Automatic generation of tree level helicity amplitudes*, *Comput. Phys. Commun.* **81** (1994) 357–371, [hep-ph/9401258].

[133] F. Maltoni and T. Stelzer, *MadEvent: Automatic event generation with MadGraph*, *JHEP* **02** (2003) 027, [hep-ph/0208156].

[134] A. Belyaev *et. al.*, *Dictionary of LHC Signatures*, arXiv:0806.2838.

[135] M. L. Mangano, M. Moretti, F. Piccinini, and M. Treccani, *Matching matrix elements and shower evolution for top- quark production in hadronic collisions*, *JHEP* **01** (2007) 013, [hep-ph/0611129].

[136] **ZEUS** Collaboration, S. Chekanov *et. al.*, *Measurement of the neutral current cross section and F2 structure function for deep inelastic e+ p scattering at HERA*, *Eur. Phys. J.* **C21** (2001) 443–471, [hep-ex/0105090].

[137] **H1** Collaboration, C. Adloff *et. al.*, *Deep-inelastic inclusive e p scattering at low x and a determination of alpha(s)*, *Eur. Phys. J.* **C21** (2001) 33–61, [hep-ex/0012053].

[138] **ZEUS** Collaboration, S. Chekanov *et. al.*, *Three- and four-jet final states in photoproduction at HERA*, *Nucl. Phys.* **B792** (2008) 1–47, [arXiv:0707.3749].

[139] **CDF** Collaboration, F. Abe *et. al.*, *Measurement of the $\bar{p}p$ total cross-section at $\sqrt{s} = 546$ GeV and 1800 GeV*, *Phys. Rev.* **D50** (1994) 5550–5561.

[140] V. A. Khoze, A. D. Martin, and M. G. Ryskin, *Soft diffraction and the elastic slope at Tevatron and LHC energies: A multi-Pomeron approach*, *Eur. Phys. J.* **C18** (2000) 167–179, [hep-ph/0007359].

[141] E. Gotsman, E. Levin, and U. Maor, *A Soft Interaction Model at Ultra High Energies: Amplitudes, Cross Sections and Survival Probabilities*, arXiv:0708.1506.

[142] M. G. Ryskin, A. D. Martin, and V. A. Khoze, *Soft diffraction at the LHC: a partonic interpretation*, *Eur. Phys. J.* **C54** (2008) 199–217, [arXiv:0710.2494].

[143] E. Gotsman, E. Levin, U. Maor, and J. S. Miller, *A QCD motivated model for soft interactions at high energies*, arXiv:0805.2799.

[144] **TOTEM** Collaboration, M. Deile *et. al.*, *Diffraction and total cross-section at the Tevatron and the LHC*, hep-ex/0602021.

[145] **CDF** Collaboration, F. Abe *et. al.*, *Measurement of small angle $\bar{p}p$ elastic scattering at $\sqrt{s} = 546$ GeV and 1800 GeV*, *Phys. Rev.* **D50** (1994) 5518–5534.

[146] L. Durand and H. Pi, *Semihard QCD and High-Energy pp and $\bar{p}p$ Scattering*, *Phys. Rev.* **D40** (1989) 1436.

[147] L. Durand and H. Pi, *High-energy nucleon nucleus scattering and cosmic ray cross-sections*, *Phys. Rev.* **D38** (1988) 78–84.

[148] T. T. Chou and C.-N. Yang, *Model of Elastic High-Energy Scattering*, *Phys. Rev.* **170** (1968) 1591–1596.

[149] A. Sherstnev and R. S. Thorne, *Parton Distributions for LO Generators*, arXiv:0711.2473.

[150] J. Dischler and T. Sjöstrand, *A toy model of colour screening in the proton*, *Eur. Phys. J. direct* **C3** (2001) 2, [hep-ph/0011282].

[151] R. M. Godbole, A. Grau, G. Pancheri, and Y. N. Srivastava, *Soft gluon radiation and energy dependence of total hadronic cross-sections*, *Phys. Rev.* **D72** (2005) 076001, [hep-ph/0408355].

[152] A. Achilli *et. al.*, *Total cross-section and rapidity gap survival probability at the LHC through an eikonal with soft gluon resummation*, *Phys. Lett.* **B659** (2008) 137–143, [arXiv:0708.3626].

[153] **CDF** Collaboration, F. Abe *et. al.*, *Measurement of double parton scattering in $\bar{p}p$ collisions at $\sqrt{s} = 1.8$ TeV*, *Phys. Rev. Lett.* **79** (1997) 584–589.

[154] A. Buckley, "The hepthesis LaTeX class."

List of Figures

List of Tables

Acknowledgements

I joined the institute of theoretical physics in Karlsruhe in 2005. First for my diploma thesis and after that starting my PhD there as well. It has been a great pleasure and learning experience. I am particularly grateful to Prof. Dieter Zeppenfeld, who gave me the possibility to perform my PhD studies in his group and the freedom to work abroad for two research stays. Stefan Gieseke deserves special thanks for coping with the tons of questions I had. Furthermore he had the wisdom to give me a research topic that turned out to be perfectly suited and diverse enough to last interesting over the last 3 years. I am grateful for the belief both had in me, to let me work that independently.

I was extremely lucky to raise the interest of two well established scientists to collaborate with me: Prof. Michael Seymour and Prof. Jonathan Butterworth. Without these two, I would not have spent 6 productive and exciting month at CERN and UCL. I really enjoyed working with you and thank you very much for this opportunity. You made the decision to leave physics much harder and I hope we will meet again sometime.

The work described in this thesis has been carried out using the Herwig++ Monte Carlo event generator, and I want to thank my fellow authors and Leif Lönnblad for constant support, comments and answers to my questions.

I want to thank all the students I have met during my time in Karlsruhe for making life at the institute great fun, particularly Gunnar Klämke and Vera Hankele who shared an office with me (although I have been there rather unpredictably).

This work work was partly supported by the *Graduiertenkolleg Hochenergiephysik und Teilchenastrophysik*, *Strukturiertes Promotionskolleg des Landes Baden-Würt-*

temberg: Promotionskolleg am Centrum für Elementarteilchenphysik und Astroteilchenphysik CETA and by the European Union Marie Curie Research Training Network *MCnet* under contract MRTN-CT-2006-035606. It was made in LaTeX 2_ε using the "hepthesis" class [154]. Most of the plots wouldn't have been so nice without Florent Fayette raising my attention to the Python plotting package `Matplotlib`.

Finally, I wish to thank my family and especially Johanna for all their love and support.